Title

Tropical sources and sinks of carbonyl sulfide constrained by atmospheric observations

Author

Stinecipher, James Robert

Publication Date

2020

UNIVERSITY OF CALIFORNIA, MERCED

Tropical sources and sinks of carbonyl sulfide constrained by atmospheric observations

A dissertation submitted in partial satisfaction of the requirements
for the degree of Doctor of Philosophy

in

Environmental Systems

by

James Robert Stinecipher

2020

Committee in Charge:

Professor J. Elliott Campbell, Ph.D., Chair
Professor Roger C. Bales, Ph.D.
Professor Marilyn L. Fogel, Ph.D.
Professor Noemi Petra, Ph.D.
Professor Leroy Westerling, Ph.D.

This work performed in part under the auspices of the U.S. Department of Energy by Lawrence Livermore National Laboratory under Contract DE-AC52-07NA27344.

The Dissertation of James Robert Stinecipher is approved, and it is acceptable
in quality and form for publication on microfilm and electronically:

Professor Roger C. Bales

Professor Marilyn L. Fogel

Professor Noemi Petra

Professor Leroy Westerling

Professor J. Elliott Campbell (Advisor)

University of California, Merced

2020

Table of Contents

List of Tables

List of Figures

Acknowledgements

I am first grateful to my advisor, Dr. Elliott Campbell, for taking a chance and hiring a math student to work in an atmospheric chemistry lab. Your limitless optimism and enthusiasm for science made this degree possible and I am thankful for everything I have learned from you along the way.

Committee members Dr. Roger Bales, Dr. Marilyn Fogel, Dr. Noemi Petra and Dr. Leroy Westerling have all offered countless suggestions and thoughtful questions that have made this work (and my own education) better. I am grateful for the myriad lessons I learned from all of you, both in and out of the classroom.

This work was funded in part thanks to the UC Lab Fees Fellowship Program (Grant LGF-17-476795), in partnership with Lawrence Livermore National Laboratory. My LLNL mentor Dr. Philip Cameron-Smith kept me focused on my goals and my future. Thank you for taking me on at the Lab and for giving me a push whenever I found myself stuck. Angela Jefferson at LLNL was always able to answer my questions, make me smile, and make my years at the Lab a positive experience.

Portions of Chapter 2 are a reprint of “Biomass Burning Unlikely to Account for Missing Source of Carbonyl Sulfide” as it appears in *Geophysical Research Letters*. Permission to use copyrighted material in this dissertation has been granted by John Wiley and Sons.

I have been fortunate to work with a wide group of collaborators who have provided data, advice, ideas and support. I am grateful to Dr. Le Kuai for her help running GEOS-Chem and working with data from TES, and to Dr. Kevin Bowman, Dr. Nicholas Parazoo and Dr. Meemong Lee for their support at the Jet Propulsion Laboratory. Dr. Joseph Berry, Dr. Ian Baker and Dr. Yoichi Shiga provided helpful directions for ongoing and future research. Fellow Campbell lab members Dr. Timothy Hilton, Dr. Mary Whelan, Dr. Andrew Zumkehr, Dr. Brandi McKuin and Dr. Gara Villalba have all, on numerous occasions, kindly lent their support, advice and skills to my work.

Blake McAlister and Garrett Tornello got me through the last three years of this degree. I honestly lack the words to say how much I value your friendship, counsel and encouragement. Thank you both for constantly pushing me forward when life got challenging.

Finally, I am grateful for the love and support of my parents, Eileen Swift and Richard Stinecipher, my sister Hailey Stinecipher, her partner AJ Bassill, and my husband Howard Hua. You have all been tremendous sources of strength through this endeavor and I dedicate this work to you.

Curriculum Vita

James Robert Stinecipher

EDUCATION

Ph.D. – Environmental Systems (2020), University of California, Merced
B.A. – Mathematics (2014), California State University, Fresno

PEER-REVIEWED PUBLICATIONS

J. E. Campbell, M. Laine, **J. Stinecipher**, L. Kuai, C. Wang, K. Zhu, Y. Wang, M. Palm, J. Notholt, J. A. Berry, S. A. Montzka, P. Cameron-Smith (2021). "Increase in atmospheric CO_2 seasonal amplitude controlled by gross primary production." *In prep.*

J. Stinecipher, L. Kuai, N. Glatthor, M. Höpfner, I. Baker, C. Beer, J. A. Berry, K. Bowman, S. Miller, N. Parazoo, P. Cameron-Smith, J. E. Campbell (2020). "Remotely Sensed Carbonyl Sulfide Constrains Model Estimates of Tropical Primary Productivity." *Submitted to Science.*

G. Villalba, M. Whelan, S. Montzka, P. Cameron-Smith, M. Fischer, A. Zumkehr, T. Hilton, **J. Stinecipher**, I. Baker, H. A. Michelsen, B. LaFranchi, R. P. Bambha, C. Estruch, J. E. Campbell (2020). "Using Carbonyl Sulfide to Track the Urban Biosphere Signal." *Submitted to J. Geophys. Res. Atmospheres.*

J. Stinecipher, P. Cameron-Smith, N. Blake, L. Kuai, B. Lejeune, E. Mahieu, I. Simpson, J. E. Campbell (2019). "Biomass Burning Unlikely to Account for Missing Source of Carbonyl Sulfide." *Geophys. Res. Lett.*, 46, 14912-13920. doi:10.1029/2019GL085567

J. E. Campbell, M. E. Whelan, J. A. Berry, T. W. Hilton, A. Zumkehr, **J. Stinecipher**, Y. Lu, A. Kornfeld, U. Seibt, T. E. Dawson, S. A. Montzka, I. T. Baker, S. Kulkarni, Y. Wang, S. C. Herndon, M. S. Zahniser, R. Commane, M. E. Loik (2017). "Coast redwood sink of atmospheric carbonyl sulfide provides a new biogeochemical tracer for coastal fog-mediated processes." *J. Geophys. Res. Biogeosciences*, 112. doi:10.1002/2016JG003703.

J. E. Campbell, J. Kesselmeier, D. Yakir, J. A. Berry, P. Peylin, S. Belviso, T. Vesala, K. Maseyk, U. Seibt, H. Chen, M. E. Whelan, T. W. Hilton, S. A. Montzka, M. B. Berkelhammer, S. T. Lennartz, L. Kuai, G. Wohlfahrt, Y. Wang, N. J. Blake, D. R. Blake, **J. Stinecipher**, I. Baker, S. Sitch (2017). "Assessing a New Clue to How Much Carbon Plants Take Up." *EOS*, 98, 24-29.

N. Glatthor, M. Höpfner, I. T. Baker, J. A. Berry, J. E. Campbell, S. R. Kawa, G. Krysztofiak-Tong, A. Leyser, B.-M. Sinnhuber, G. R. Stiller, **J. Stinecipher**, T. von Clarmann (2015). "Tropical sources and sinks of carbonyl sulfide observed from space." *Geophys. Res. Lett.*, 42, 10082-10090. doi:10.1002/2015GL066293

SKILLS SUMMARY

MATLAB, GrADS, bash, csh, FORTRAN, R, IDL, Python,
Adobe InDesign, Adobe Illustrator, Microsoft Office, VisIt, Slack, LaTeX

PROFESSIONAL EXPERIENCE

Graduate Fellow, Lawrence Livermore National Laboratory (2017 – 2020)
UC Lab Fees In-Residence Graduate Fellowship Program

Participant in the following workshops:
- 2019 NASA Summer School on Satellite Observations and Climate Models
- 2017 Keck Institute for Space Studies Workshop "Next-Generation Approach for Detecting Climate-Carbon Feedbacks: Space-Based Integration of Carbonyl Sulfide (OCS), CO_2, and Solar Induced Fluorescence (SIF)"
- 2017 National Center for Atmospheric Research Community Earth System Model Workshop

Graduate Student Researcher, University of California, Merced (2014 – 2017)
- Helped conduct air sampling campaigns along California coast
- Analyzed data from regional chemical transport models

Teaching Assistant, University of California, Merced (2015 – 2016)
ENVE 160 / ES 260 – Sustainable Energy
- Maintained regular office hours, developed rubrics, graded assignments
- Organized tour of campus energy and recycling facilities

AWARDS AND GRANTS

University of California Laboratory Fees Research Program In-Residence Graduate Fellowship ($200,000)	2017-2020
LLNL Deputy Director's S&T Excellence in Publication Award	2020
LLNL Summer Poster Symposium Winner	2017, 2018
UC Merced Environmental Systems Bobcat Travel Fellowship ($1600)	2017
NSF Graduate Research Fellowship Program – Honorable Mention	2016
University of California Carbon Slam – Finalist	2016
UC Merced Environmental Systems Bobcat Fellowship ($6000)	2016
UC Merced Environmental Systems Bobcat Fellowship ($6000)	2015
UC Merced Chancellor's Graduate Fellowship ($8000)	2014

Abstract

Tropical sources and sinks of carbonyl sulfide constrained by atmospheric observations

by
James Robert Stinecipher
Doctor of Philosophy in Environmental Systems
University of California, Merced, 2020
Professor J. Elliott Campbell, Advisor

Carbonyl sulfide (OCS or COS) is the most common sulfur-containing species in the atmosphere and has the potential to function as a proxy for photosynthetic carbon uptake (gross primary productivity, GPP). In order to expand this technique to regional and global scales, additional questions about poorly constrained aspects of the carbonyl sulfide budget must be resolved.

The first section of this work is devoted to developing a new, spatially resolved and temporally varying inventory of carbonyl sulfide emissions from biomass burning. By leveraging long-term, *in situ* observations of atmospheric carbonyl sulfide, we demonstrate that biomass burning emissions are heavily dependent on biome and are not sufficient to close the overall flux budget.

The second section of this dissertation uses this biomass burning inventory in conjunction with a global chemical transport model in order to constrain plant fluxes in the Amazon basin. Using satellite data from the Michelson Interferometer for Passive Atmospheric Sounding (MIPAS) instrument, I show that downstream observations of carbonyl sulfide in the upper troposphere retain useful information about surface processes and can provide an independent constraint on gross primary production given sufficient convective transport.

Finally, I conduct an observing system simulation experiment (OSSE) to investigate how future remote-sensing campaigns could yield more information and better constrain GPP using carbonyl sulfide. In addition to considering sampling density, sampling height and instrument noise in satellite observations, I address potential challenges in future aircraft sampling campaigns.

Chapter 1: Introduction

Feedbacks between atmospheric carbon dioxide and photosynthesis are one of the largest sources of uncertainty in climate models (Arneth et al., 2010). On one hand, increases in atmospheric carbon dioxide could stimulate photosynthetic uptake, leading to increased uptake of CO_2 and a negative feedback loop. On the other hand, as CO_2 levels lead to warmer climates, plant productivity may decrease and reduce the amount of CO_2 being removed from the atmosphere. Accurately balancing these competing effects remains a major challenge in assessing future climate scenarios.

Constraining these feedbacks is complicated by a further challenge: the tropics, which account for over a third of global photosynthetic carbon uptake, are also the areas where ecosystem models are most likely to diverge (Beer et al., 2010; Malhi, 2012). Better constraints on the amount of carbon taken up by plants – gross primary production, or GPP – are needed.

A variety of techniques exist to measure GPP. At the smallest scale, measurements may be made in leaf chambers, comparing mixing ratios of carbon dioxide over time and varied light conditions (Baldocchi, 2003; Baldocchi & Harley, 1995; Gara et al., 2019; Harley & Baldocchi, 1995; Sprintsin et al., 2012). Extending these observations to regional or global scales, however, requires many assumptions. Natural variability across individual leaves or plants may be difficult to quantify with limited sampling, and the sampling chamber design itself may cause changes in light availability or local meteorology which are inconsistent with natural conditions. Upscaling requires information about the variety of plants and plant functional types in a region, as well as nutrient, water, and light availability. Assumptions about the vertical structure are also necessary to quantify the portion of leaves receiving direct or indirect sunlight.

At a regional level, observations with eddy flux towers are a common approach (Beer et al., 2010; Billesbach et al., 2014; Joiner et al., 2011; Jung et al., 2011). Changes in CO_2 concentrations can be partitioned into photosynthesis and respiration fluxes by using nighttime observations. Two challenges exist in using this technique to constrain global GPP. First, flux tower observations are sensitive to a small footprint and may be heavily influenced by regional meteorology or surface conditions. Second, the sparse network of flux tower sites may lead to under-sampling in key regions, like the Amazon.

Global observations by satellites take many forms. Measurements of global CO_2 concentrations are commonplace, but these represent a *net* flux. Disentangling the collocated respiration source from the photosynthetic sink is challenging; the component fluxes are large and similar in magnitude, but the net flux is small (Steffen et al., 1998). As such, small changes in either component may yield large relative changes in the net flux.

Satellite observations of solar-induced fluorescence (SIF) represent a relatively new approach to quantifying photosynthesis (Frankenberg et al., 2011; Guanter et al., 2014; Joiner et al., 2011; Parazoo et al., 2014). By measuring small emissions of excess light, one can infer the amount of photosynthesis at a given moment. This approach, too, has its challenges. Because the observations are made from the top of the canopy, complexity in the vertical structure may underestimate uptake in the understory. Additionally, contamination by clouds may limit the availability of observations, especially in the tropics.

These limitations suggest the need for an approach that is scalable, able to partition photosynthesis and respiration, and integrative over both space and time. One potential approach is the use of atmospheric carbonyl sulfide (OCS), which has been shown in a variety of contexts to function as a proxy for GPP (Asaf et al., 2013; Berry et al., 2013; Campbell et al., 2008). Particularly in the Amazon basin, where sampling sparsity limits *in situ* studies and frequent cloudiness limits satellite observations, OCS could provide valuable information about surface processes.

Atmospheric carbonyl sulfide concentrations are controlled primarily by a plant uptake sink and an oceanic source. OCS is taken up by plants through the stomata and follows similar metabolic pathways to CO_2 (Protoschill-Krebs et al., 1996; Sandoval-Soto et al., 2005; Seibt et al., 2010). Unlike CO_2, however, OCS is irreversibly hydrolyzed to H_2S. As a result, while CO_2 concentrations are affected by both photosynthesis and respiration, changes in OCS fluxes from plants are one-directional and can therefore be used for estimating stomatal conductance and GPP.

Ocean production of OCS takes the form of both direct OCS emissions and indirect emissions due to oxidation of carbon disulfide (CS_2) and dimethyl sulfide (DMS) (Kettle et al., 2002). On a global scale, ocean activity is a source of OCS; however, at high latitudes in winter, oceans may take up OCS due to undersaturation.

Other processes contribute to the overall OCS budget. Anthropogenic activity, both industrial and residential, is a source of OCS. Recent work by Zumkehr et al. (2017, 2018) shows that a majority of these emissions now come from Asia, with large contributions from rayon production. Biomass burning is a small but variable source in the OCS budget. As demonstrated in this work (reprinting Stinecipher et al., 2019), OCS emissions from biomass burning vary significantly across biomes. Soils are typically OCS sinks, varying in intensity depending on biome, temperature, nutrient availability and soil moisture content. Under certain conditions (e.g., anoxic wetlands and agricultural soils) soils have also been shown to produce OCS (Whelan et al., 2018). Particularly in the stratosphere, OCS is also destroyed by hydroxyl radicals.

While much has been learned about the global OCS budget, our knowledge remains incomplete. Long-term observations of atmospheric OCS show moderate trends consistent with increasing GPP over the past century (Campbell et al., 2017). On the short-term, atmospheric OCS concentrations have been more stable, implying an overall balanced flux budget (Montzka et al., 2007). However, best estimates for each of these budget components still yield a gap of 200 to 600 Gg (S) yr^{-1}. The present work seeks to constrain two specific portions of this budget: global emissions from biomass burning and regional photosynthetic uptake in the Amazon basin.

Chapter 2, “Biomass Burning Unlikely to Account for Missing Source of Carbonyl Sulfide,” investigates the contributions to the overall OCS flux budget from biomass burning. This dataset is an initial attempt at developing a spatially and temporally varying biomass burning inventory that accounts for differences in OCS emission factors across a variety of biomes. These biome-specific emission factors provide an updated understanding of both the spatial distribution and magnitude of OCS emissions from each fuel category. The flux data are validated against long-term atmospheric observations of OCS, constraining both the overall magnitude of fluxes and the contributions of particular emission sources (e.g., tropical peat).

Chapter 3, “Remotely Sensed Carbonyl Sulfide Constrains Model Estimates of Gross Primary Production,” builds on the inventory developed in Chapter 2, implementing the results in a 4-dimensional atmospheric transport and chemistry model. Using upper-troposphere observations of OCS measured by satellite, the modeling work in Chapter 3 seeks to constrain the largest sink in the OCS budget, that of plant uptake. This work shows that ecosystem models which assume lower GPP in the Amazon basin are most consistent with the observed upper-troposphere depletion in OCS. In addition, this work demonstrates the value of OCS as a “downstream” tracer of GPP. Provided sufficient convection exists, models can be used to identify regions in the upper-troposphere which are sensitive to changes at the surface.

Chapter 4 of this work, “Observing System Simulation Experiments Underscore Need for Future Carbonyl Sulfide Sampling Campaigns,” lays the groundwork for future OCS research using an observing system simulation experiment (OSSE). Because of inherent challenges working with the observational data in Chapter 3, this work provides valuable insight on ways data collection can be improved and the extent to which uncertainty in the results from Chapter 3 can be mitigated. In particular, this work shows that increases in tropical sampling density, lower sampling altitudes and reductions in instrument noise all yield improvements to the overall retrieval.

Chapter 2: Biomass Burning Unlikely to Account for Missing Source of Carbonyl Sulfide

2.1 Abstract

Carbonyl sulfide (OCS) provides a proxy for measuring photosynthesis and is the primary background source of stratospheric aerosols. OCS emissions due to biomass burning are a variable and substantial (over 10%) part of the current OCS budget. OCS emission ratios from open burning fires, coupled with 1997-2016 data from the Global Fire Emissions Database (GFED4), yield OCS biomass burning emissions with a global average annual flux of 60 ± 37 Gg (S) yr^{-1}. A global box model suggests these emissions are more consistent with observations from global atmospheric composition monitoring networks than fluxes derived from previous synthesis papers. Even after considering the uncertainty in emission factor observations for each category of emissions and the interannual variation in total burned dry matter, the total OCS emissions from open burning are insufficient to account for the large imbalance between current estimates of global OCS sources and sinks.

2.2 Background

Carbonyl sulfide (abbreviated OCS or COS) is the most abundant sulfur gas in the atmosphere and is important both as a tracer for gross primary production and as a source of stratospheric aerosols. Current estimates of surface fluxes and atmospheric sinks of OCS do not fully account for all processes necessary to balance the OCS budget. For example, Berry et al. (2013) assume a deficit in the OCS source of approximately 600 Gg (S) yr^{-1} (annual mass of sulfur emitted as OCS), compared to a total sink of approximately 1200 Gg (S) yr^{-1}. While ocean chemistry has been hypothesized as a possible way to close this budget gap (Berry et al., 2013; Suntharalingam et al., 2008), other sources including biomass burning, anthropogenic emissions, and anoxic soils may be partially responsible.

Biomass burning has long been recognized as a source of OCS, particularly in smoldering fires (Chin & Davis, 1993; Crutzen et al., 1979, 1985; Crutzen & Andreae, 1990; Kettle et al., 2002; Khalil & Rasmussen, 1984). However, due to differing methodologies and study assumptions, estimates of global total OCS emissions vary widely in the literature (11 Gg (S) yr^{-1} in Kettle et al., 2002, 136 Gg (S) yr^{-1} in Berry et al., 2013 and 68-144 Gg (S) yr^{-1} in Montzka et al., 2007).

Emissions of OCS from biomass burning can be measured and reported in several ways (Akagi et al., 2011). Samples may be burned in a lab setting, allowing for simultaneous measurements of changes in mass and composition of the emitted plume (e.g., Yokelson et al., 1997). When the mass of fuel is known, measurements may be reported as emission factors (EFs), defined as the mass of a species emitted relative to the mass of dry matter (DM) burned (e.g., kg OCS / kg biomass). Samples may also be taken in the field where fires are present, either at ground level (e.g., Meinardi et al., 2003; Nguyen et al., 1995) or by flying through a plume (e.g., Blake et al., 2004; Nguyen et al., 1995). In the field, it can be challenging to accurately measure the total mass burned, and hence, field measurements are frequently reported as emission ratios (ERs), that is, relative enhancements over background values (e.g., [mol OCS_{plume} – mol $OCS_{background}$] / [mol CO_{plume} – mol $CO_{background}$], yielding units of mol OCS / mol CO).

The Global Fire Emissions Database (GFED Version 4, https://www.globalfiredata.org/) provides spatially and temporally resolved maps of fire emissions in a variety of categories based on satellite observations (Giglio et al., 2013; Randerson et al., 2012; van der Werf et al., 2017), as well as a summary table of emission factors for a variety of species (not including OCS), primarily based on Andreae and Merlet (2001) and Akagi et al. (2011). We seek to expand these existing works with updated average emission ratios for OCS, suitable for use with burned totals from GFED.

2.3 Methods

We collected all the published emission factors and emission ratios for carbonyl sulfide, along with corresponding measurements of CO and CO_2 emissions, as available (Table 2-1). Based on fuel type and sample location, we assigned samples to one of the six biomass burning categories used in GFED: savanna and grassland (SAVA), boreal forests (BORF), temperate forests (TEMF), tropical deforestation and degradation (DEFO), peatland fires (PEAT), and agricultural waste burning (AGRI). Categorized samples are shown in Table 2-2 with mean values for each category given in Table 2-3.

Crutzen and Andreae (1990) and Meinardi et al. (2003) show that, while CO_2 emissions peak in the flaming stage, CO and OCS both peak during the later smoldering stage. Hence, in order to combine emission measurements between observational datasets, we compute all possible values as emission ratios relative to CO (mol OCS emitted / mol CO emitted). This has the benefit of including the many studies where the total mass burned was not available but does exclude several studies where CO was not measured. Where emission ratios are not given directly, we calculate them either as the ratio of OCS and CO emission factors or as an enhancement in OCS relative to CO as described above, depending on how data are presented in a given study (see Section 2.7.2).

To test the impact of these emission ratios on global OCS concentrations, we first compute total CO emissions for each category in the GFED4 inventory, using emission factors provided by GFED to convert from total burned dry matter to CO. We then apply the emission ratios described above to these CO totals to obtain global total emissions of OCS in each category.

The OCS emissions are used as an input in a one-box global model, run at monthly timesteps and driven by zero-order sources (biomass burning, biofuels, anthropogenic emissions and oceanic emissions), a zero-order soil sink, and first-order sinks for plant uptake and destruction of OCS by hydroxyl radicals. Zero-order fluxes vary independently of ambient atmospheric OCS concentrations, while first-order fluxes vary proportionally to ambient atmospheric OCS concentrations. A constant, supplemental source is added to maintain a balanced budget. Previous works (Berry et al., 2013; Campbell et al., 2017; Suntharalingam et al., 2008) ascribe this flux to a missing ocean source; however, more recent estimates by Lennartz et al. (2017, 2019) find that ocean emissions are insufficient to close the budget and other fluxes must be involved. The model assumes the atmosphere is well-mixed at every timestep, which is reasonable because the atmospheric lifetime of OCS is approximately 2 years (Campbell et al., 2008; Khalil & Rasmussen, 1984; Montzka et al., 2007). Additional details are given in Section 2.7.3.

We compare the outputs of this box model to NOAA ground-based flask samples taken at a variety of sites since approximately 2000 (Montzka et al., 2007) and annually averaged tropospheric mixing ratios derived from Fourier Transform InfraRed (FTIR) solar spectra recorded at the Jungfraujoch station (Swiss Alps) since 1984 (Lejeune et al., 2017). The NOAA datasets provide a global perspective on OCS trends from 2000 onward, whereas the Jungfraujoch dataset provides one of the only time series of OCS mixing ratios covering the entire GFED4 data period (1997 to 2016). Measurements at Jungfraujoch are specific to that site but are still influenced by changes in global concentrations like those predicted by the global box model because of the long atmospheric lifetime of OCS.

2.4 Results

Figure 2-1 shows the range of observed emission ratios for the six categories used in GFED. Emission ratios from both lab and field studies are shown as black X's. Previous estimates from Andreae and Merlet (2001) and Akagi et al. (2011) use subsets of these data to estimate average emission factors by ecosystem type. As neither inventory covers all of the biome categories, we combine both inventories by using the reported value (if only one study provides a value) or averaging values from both studies, if available.

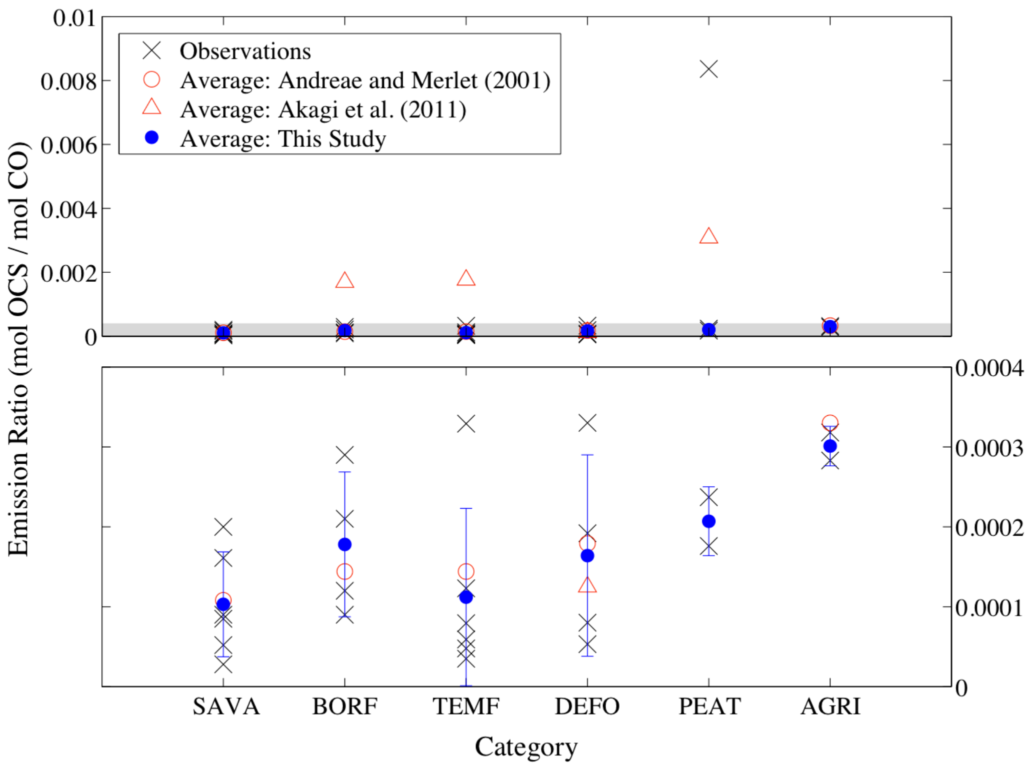

Figure 2-1: Comparison of emission ratio estimates from various literature sources. In order to span the wide range of values, the grey region of the top panel is shown with an expanded scale in the bottom panel. Black x's are individual studies or measurements. Blue dots are the averages used in this paper. Red circles and triangles are average values from Andreae and Merlet (2001) and Akagi et al. (2011), respectively. Error bars represent the standard deviation of emission ratio observations included in the average value for each category. Categories are described in the Methods (Section 2.3). Additional details and numerical data are given in Section 2.7.

Akagi et al. (2011) present OCS and CO emission factors for boreal, temperate (extratropical) and peat ecosystems that are an order of magnitude larger than the other three categories (the three highest red triangles in Figure 2-1). This is due to the inclusion of an anomalously high observation of OCS emitted from a boreal peat sample in a chamber experiment (Yokelson et al., 1997 – Table 1, Minnesota Peat). Compared to another peat sample from the same study (Yokelson et al., 1997 – Table 1, Alaska Peat), this sample yielded over 25 times the OCS per dry matter burned and 35 times the OCS relative to CO. The emission ratio for this sample relative to CO is also more than 40 times larger than the emission ratio computed for a sample of Indonesian peat in Stockwell et al. (2016). Dixon's Q-test (Dean & Dixon, 1951) identifies this largest peat sample as an outlier with 95% confidence and we thus exclude it from our averages.

Our goal is to compare the impact of different possible emission factors against observed OCS concentrations. Specifically, we compare the impact of prior emission estimates to an updated calculation of average emission ratios which includes a wider set of observational data than in previous studies, while excluding the anomalously high peat observation on the basis that it may not be representative of most locations. Our emission ratios for boreal, temperate, and peat ecosystems are an order of magnitude lower than estimates from Akagi et al. (2011), but within 25% of those presented in Andreae and Merlet (2001). Average emission ratios for savanna, tropical deforestation and agricultural waste are within 40% of those presented in Akagi et al. (2011) and Andreae and Merlet (2001). Across categories, our emission ratios range from 1×10^{-4} mol OCS / mol CO (savanna and grassland) to 3×10^{-4} mol OCS / mol CO (agricultural waste burning).

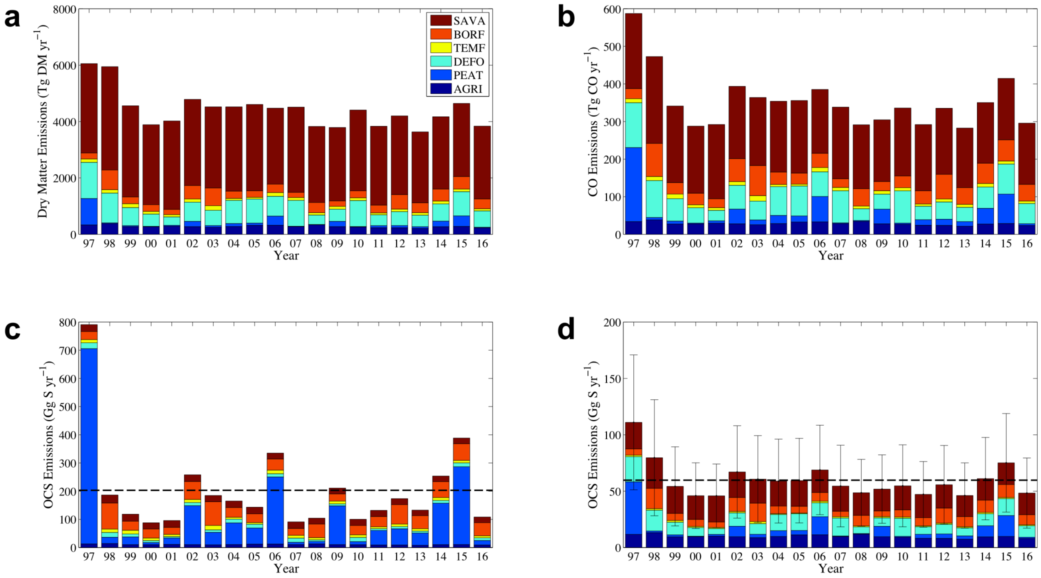

Figure 2-2: Annual total GFED4 estimates of (a) burned dry matter (DM) and (b) associated emissions of CO based on GFED4 emission factors. OCS emissions based on (c) combined emission ratios from Andreae and Merlet (2001) and Akagi et al. (2011) and (d) this study. Dotted lines on panels (c) and (d) represent the average annual total across all years. Error bars in panel (d) are derived from the relative uncertainty in CO emission factors and OCS emission ratios, described in Section 2.7.3. Note the change in y-axis scaling between panels (c) and (d).

We apply these emission ratios to global biomass burning inventories from GFED in order to estimate the corresponding OCS emissions. The GFED estimates of burned dry matter are dominated by savannas, followed by tropical deforestation and boreal forests (Figure 2-2a). The GFED estimates show particularly large interannual variability for peatlands, with nearly 10 times more peat burned in 1997 than the 19982016 average due to massive fires in Indonesia during a large El Niño event (Page et al., 2002). A similar, smaller spike occurs during the 2015 El Niño event.

As mentioned above, we use CO as a reference species to compute OCS emissions. These CO emissions are computed from the emission factors provided by GFED and are shown in Figure 2-2b.

We combine these GFED CO emissions with (i) OCS emission ratio averages from Andreae and Merlet (2001) and Akagi et al. (2011), and (ii) the emission ratio averages we calculated to create a temporally and spatially varying OCS burning inventory (Figures 2-2c and 2-2d, respectively). Note that while savannas and grassland (SAVA) account for 52% to 78% of burned matter depending on the year (Figure 2-2a), they are a small source of OCS (3% to 26% of biomass burning emissions using emission ratios from previous synthesis papers and 21-51% of emissions using the present emission ratios) due to the relatively small emission ratio (Figure 2-2c and 2-2d). Conversely, peatland emissions (PEAT) are a small and variable part of the dry matter total (0.2% to 15%) but a major source of OCS, especially using emission ratios derived from previous synthesis papers (8% to 88% of emissions using previous emission ratios, 1% to 42% using present emission ratios).

Fluxes derived from previous emission ratio inventories are larger in magnitude and in interannual variability (mean 203 Gg (S) yr^{-1}, standard deviation 161 Gg (S) yr^{-1} over all available years) than those derived from our present estimates (mean 60 Gg (S) yr^{-1}, standard deviation 15 Gg (S) yr^{-1} over all available years). Additionally, while 1997 is an exceptional year for both sets of emission factors, the spike in emissions is more pronounced in the previous estimates: total 1997 OCS emissions are 4.6 times larger than the mean from 1998 to 2016 (compared to 1.9 times using our emission ratios). In the years following 1997, the previous emission ratios also yield emissions with coefficients of variation (standard deviation divided by mean) twice as large as those from our present emission ratios.

We examine the validity of these two alternative OCS emission scenarios through two runs of a global atmospheric box model, validated against atmospheric observations (Figure 2-3a). As in previous work, the simulation budget is balanced by adding a supplemental constant source (Berry et al., 2013; Campbell et al., 2017; Suntharalingam et al., 2008) to other sources and sinks described above (Figures 2-3b and 2-3c). Note that the supplemental source for the previous inventories is considerably smaller due to their larger average biomass burning contribution.

Observed atmospheric surface mixing ratios from global and hemispheric averages of NOAA air monitoring sites (Montzka et al., 2007), as well as annually averaged tropospheric mixing ratios from Jungfraujoch (Lejeune et al., 2017), show a moderate decline in the 1990’s followed by similarly moderate growth in the 2000’s (both approximately 1% yr^{-1}), with relatively little interannual variation. These time trends have been attributed to trends in the anthropogenic inventory, driven by a decline in residential coal in the early 1990’s and the decline and growth of the rayon industry from 1990 onward (Campbell et al., 2015; Du et al., 2016; Zumkehr et al., 2017, 2018).

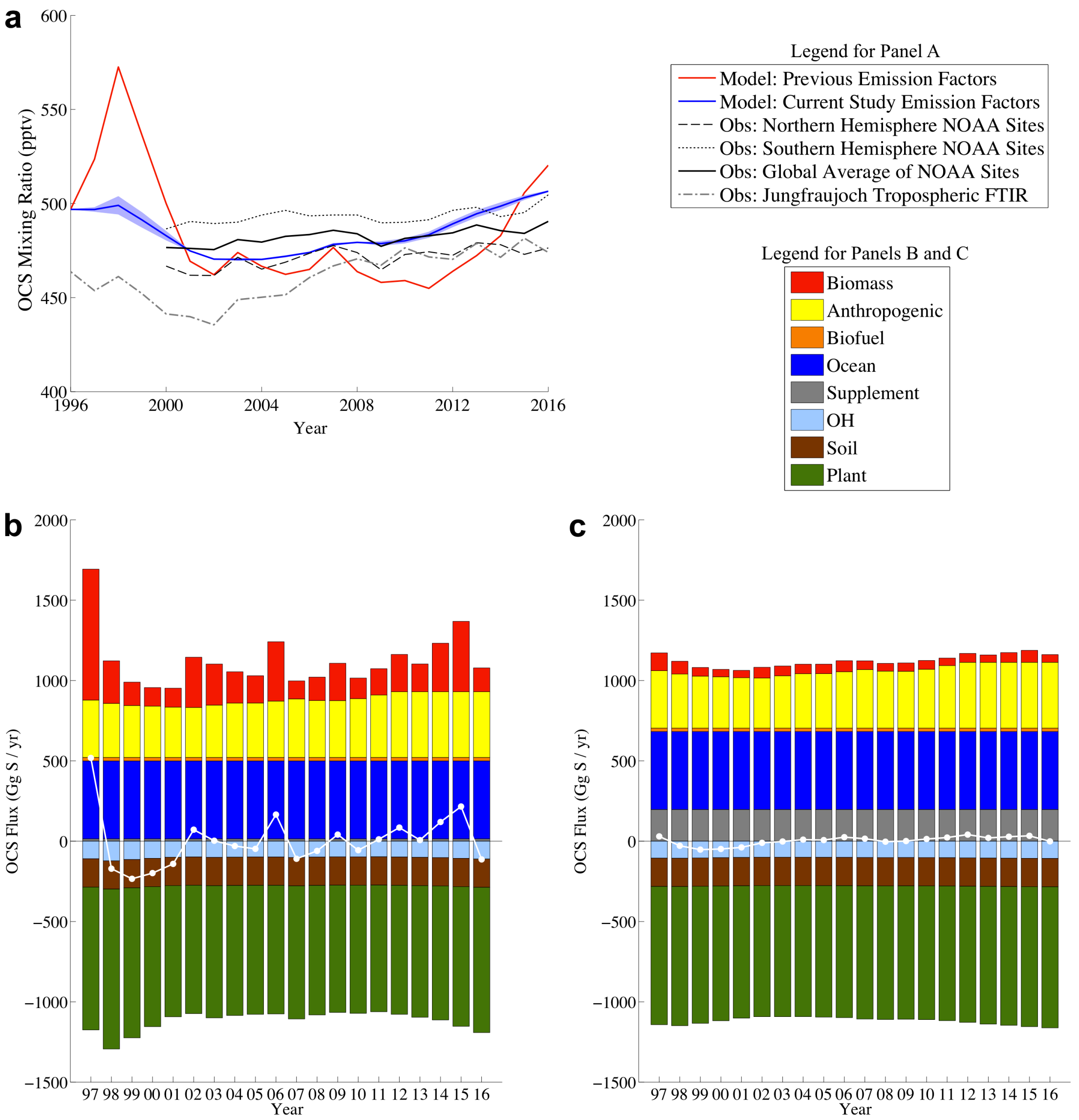

Figure 2-3: Panel (a) shows box model outputs and observations from NOAA air monitoring sites (Montzka et al., 2007) and the tropospheric FTIR data from Jungfraujoch, Switzerland (Lejeune et al., 2017). Previous emission factors are based on Andreae and Merlet (2001), Akagi et al. (2011) or an average of both. The shaded region represents the uncertainty due to the range in emission factors and emission ratios. Panels (b) and (c) show annual fluxes of OCS by category as used in the "previous" and "current" models, with net fluxes indicated by the white dotted line. In both (b) and (c), a supplemental flux is added to close the budget, described in the Methods. Additional details are given in Section 2.7.3.

A simulation using our new emission ratios yields concentrations and interannual variations that are broadly consistent with the observational records. In contrast, a simulation using emission ratios from the previous inventories is unable to capture these trends. In particular, the spike in concentrations following emissions in 1997 and the rapid growth from 2012 onward are accentuated in the model output, but largely absent in the observations.

We quantitatively assess these differences in two ways. We first consider the spike in concentrations following the 1997 peat fires by taking the difference in concentrations between 1998 (the first full year after the event) and an average from 2000 to 2004 (after concentrations had stabilized). The Jungfraujoch dataset shows a decrease of 18 ppt (4%), while the models based on previous studies and our present emission ratios show decreases of 98 ppt (21%) and 25 ppt (5%), respectively. To compare slopes while minimizing bias due to the choice of time period, we perform linear regressions on the annual average concentrations in each model time series for every combination of years starting and ending between 2000 and 2016, inclusive. In each case, we compute root mean square errors against the corresponding slopes of the NOAA global average and the Jungfraujoch data. On average, our model using the present emission ratios yields RMSE values that are half as large as the model based on previous synthesis papers (reducing from 6.29 to 2.69 ppt OCS yr^{-1} compared to NOAA and from 7.10 to 3.66 ppt OCS yr^{-1} compared to Jungfraujoch).

2.5 Discussion

The large discrepancy between the two box model simulations, with our new emission factors giving a much closer match to observations, suggests that the anomalous peat observation is not representative of peat emissions generally and its inclusion could bias global biomass burning inventories. Our estimates show major reductions in OCS emissions from boreal forests (from an average of 45 to 9 Gg (S) yr^{-1}), temperate forests (from 10 to 1 Gg (S) yr^{-1}), and peatlands (from 104 to 7 Gg (S) yr^{-1}) due to the exclusion of the aforementioned sample. The observational constraints on the interannual variability in OCS emissions from biomass burning also constrain the annual average emissions. Unfortunately, even in years with larger-than-average OCS emissions, our estimated biomass burning flux is too small to fully close the existing OCS budget gap, so other fluxes must be involved.

Several sources of uncertainty exist in these estimates. First, although the current work includes more studies than in previous synthesis papers (Akagi et al., 2011; Andreae, 2019; Andreae & Merlet, 2001), observational studies measuring OCS emissions from fires are still few, making it difficult to gauge representativeness of the observations. We quantify the uncertainty using the spread in reported emission factors/ratios for each category, both for OCS (presented here) and for reference species (CO and CO_2) presented in the GFED documentation and Akagi et al. (2011). For each category, we add relative uncertainties (standard deviation divided by mean) for both emission factors/ratios (CO/DM and OCS/CO) in quadrature, then apply the result to the total OCS emissions for that category. Relative uncertainties are largest for temperate forest (105%) and tropical deforestation (82%) categories, followed by savannas (69%). On an absolute basis, savanna uncertainty dominates due to the larger overall contribution. Total uncertainty across all categories is added linearly in order to more conservatively account for correlation in the underlying burned matter dataset.

A second source of uncertainty is the choice of reference species in the emission ratios. OCS emissions derived from CO_2 tend to more closely follow the distribution of burned dry matter, as CO_2 emission factors (ranging from 1489 to 1703 g CO_2 / kg DM in the GFED4 documentation) are less variable than CO (63 to 210 g CO / kg DM) across the six biomass burning categories. Estimates derived from CO_2 yield higher total OCS emissions than those derived from CO (70 ± 37 Gg (S) yr^{-1} versus 60 ± 37 Gg (S) yr^{-1}, respectively), owing primarily to larger emissions from savanna and grasslands. Additional results obtained using CO_2 are presented in Table 2-4.

Other sources of uncertainty are more difficult to quantify. As noted, relatively few studies report OCS emission data, especially for peat and agriculture categories. Further, studies vary in instrumentation, calibration, and approaches to calculating emission factors or ratios. Additionally, emissions vary over the life of the fire and measurements may yield different values based on sampling location (near a fire, downwind, or in a lab). Despite these factors, the difference in the variety of samples used in our averages is significantly smaller than the effect of including or excluding the previously identified peat observation.

Our best estimate of annual-mean global OCS emissions from biomass burning (60 ± 37 Gg (S) yr^{-1}) is broadly consistent with existing estimates, which have typically been computed using global, fixed emission factors. Chin and Davis (1993) estimate the global biomass burning flux as 74.7 (21.3 to 138.7) Gg (S) yr^{-1}, based primarily on tropical fires. Nguyen et al. (1995) report global totals of 70 (30 to 110) Gg (S) yr^{-1}, later cited in Watts (2000) and Kettle et al. (2002). Andreae and Merlet (2001) present a global total of 144 Gg (S) yr^{-1}. This value includes 65 Gg (S) yr^{-1} in emissions from biofuel and charcoal, categories which are not considered in our estimate; subtracting these yields 79 Gg (S) yr^{-1}. Montzka et al. (2007) calculate an estimate of 65 Gg (S) yr^{-1}, based on CO emissions from Andreae and Merlet (2001) and Duncan (2003) and emission ratios from Nguyen et al. (1995). Berry et al. (2013) chose a value from the high end of the published range (136 Gg (S) yr^{-1}) to study the impact of emissions from different sources. Campbell et al. (2015) estimate OCS emissions from open burning (33 to 96 Gg (S) yr^{-1}) and agriculture waste burning (8 to 18 Gg (S) yr^{-1}), totaling 41 to 114 Gg (S) yr^{-1}. Finally, applying the emission factors computed in a similar review by Andreae (2019) to the GFED dataset used here yields an average of 86 Gg (S) yr^{-1}.

A further benefit of this work is the ability to derive spatially and temporally resolved OCS emission distributions using datasets such as GFED that provide biome-specific biomass burning totals. Applying the average emission ratios from this work to existing CO totals from GFED yields global maps of OCS emissions, such as the annually averaged fluxes shown in Figure 2-4a. While the present work has primarily relied on burned area data from GFED, the emission ratios presented are generally applicable to other datasets, which may be higher-resolution or more suitable for regional applications. For example, applying the present emission ratios to average burned matter data from the Fire INventory from NCAR (FINN; see Wiedinmyer et al., 2011) yields global biomass burning emissions of 84 Gg (S) yr^{-1}, primarily due to increased tropical emissions (though FINN does not explicitly account for peat). Future studies comparing emissions derived from these datasets to *in situ* measurements could further constrain emission magnitudes and distributions.

Additionally, variation in emission ratios across biomes yields different spatial patterns and categorical totals than estimates which scale all fuel types evenly. To demonstrate this, we scale the total burned dry matter up to the same global annual OCS totals calculated above, disregarding differences in emission factors between biomes. On average, our biome-specific estimate predicts savanna and grassland emissions which are 17 Gg (S) yr^{-1} less than the upscaled dry matter estimate (21 versus 39 Gg (S) yr^{-1}, respectively) with corresponding increases in emissions in other categories, especially peat (increase of 5 Gg (S) yr^{-1}) and agriculture (increase of 6 Gg (S) yr^{-1}) (Figure 2-4b). The categorical and spatial differences between burned matter and OCS emissions highlight the need for an emissions database that accounts for different sources of biomass burning.

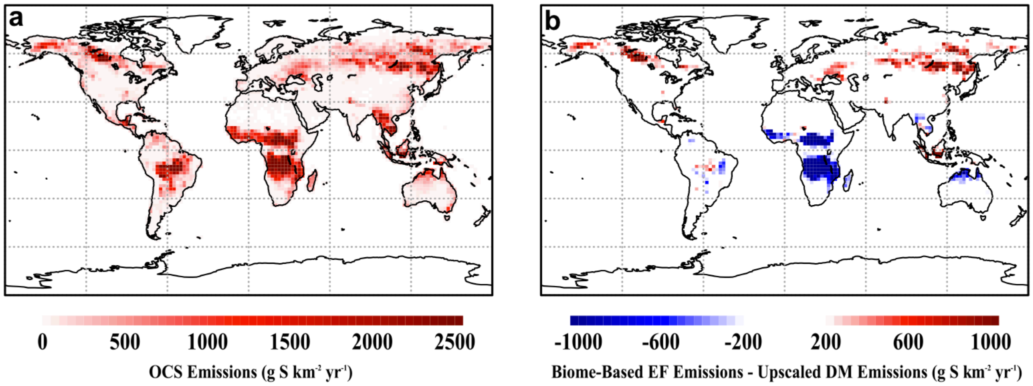

Figure 2-4: Maps showing (a) spatial distribution of average (1997-2016) annual OCS open burning emissions based on biome-specific emission ratios (relative to CO) presented in this work, and (b) difference between the biome-specific OCS estimate and an estimate based on total burned dry matter, scaled up to the same global total (i.e., without specific scaling between biomes).

2.6 Conclusion

Biomass burning represents an important component in global OCS emissions, and estimates can vary significantly in space and magnitude depending on which emission data are used. Our analysis shows that, while biomass burning emissions are highly variable from year to year, the total OCS emitted is, on average, not sufficient to close the existing OCS budget gap (60 ± 37 Gg (S) yr^{-1}, compared to a deficit of approximately 200 to 600 Gg (S) yr^{-1}). Further, previous emission factor averages yield unrealistic OCS concentration trends when implemented in a global box model, whereas inventories derived in this work better match observations.

This work provides a spatially resolved inventory of OCS biomass burning fluxes that can be implemented in atmospheric transport and chemistry modeling studies. While uncertainties remain in our present estimates, new observation campaigns (WE-CAN, FIREX, etc.) are already underway, and it is our hope that this work will spur additional campaigns to measure OCS emissions from biomass burning in the future.

2.7 Supplemental Information for Chapter 2

2.7.1 Introduction

Sections 2.7.2 through 2.7.4 provide additional information into how existing emission data was incorporated into the study's model and how output files may be obtained. Figure 2-5 shows the data from Figure 2-1 of the main text, plotted on a logarithmic scale. Tables 2-1 and 2-2 summarize emission data collected from existing literature. Table 2-3 provides quantitative values for the data displayed in Figure 2-1 of the main text. Table 2-4 provides categorical totals and ranges for the emissions calculated in the main text, as well as comparable estimates using CO_2 as a reference species.

2.7.2 Approach to Standardizing and Combining Existing Emission Data

In order to use the broadest set of OCS emission data, we compute all values as emission ratios of OCS relative to CO (mol/mol). The approaches are identical for computing ratios relative to CO_2. Here, we address three cases for standardizing emission data reported in literature:

Case 1: Study reports OCS emission ratio relative to CO (e.g., Friedli et al., 2001)
In the event a work lists an OCS emission ratio relative to CO, we report the value as-is.

Example: Friedli et al. (2001) present a "Temperate Composite" emission ratio of 1.23×10^{-4} mol OCS / mol CO. This value is used in the Temperate Forest category of Table 2-2.

Case 2: Study reports OCS emission factors (e.g., Liu et al., 2017)
In cases where OCS emissions are reported relative to the amount of mass burned, we divide the reported OCS emission factor with the reported CO emission factor, converting to moles if necessary.

In cases where multiple fires or samples are taken, we compute the emission ratio with the same sample for both OCS and CO. For example, Liu et al. (2017) present emission data for multiple fires, but OCS was only measured in the Rim Fire. Hence, for this case, we compute the OCS emission ratio relative only to CO emissions from the Rim Fire (rather than the study average).

Example: Liu et al. (2017) present emission factors of 5.9×10^{-3} g OCS / kg DM and 78.7 g CO / kg DM measured during the Rim Fire in California.
5.9×10^{-3} g OCS = 9.8×10^{-5} mol OCS
78.7 g CO = 2.8 mol CO
The calculated emission ratio of $[9.8 \times 10^{-5}] / [2.8] = 3.5 \times 10^{-5}$ mol OCS / mol CO is used in the Temperate Forest category.

Case 3: Study reports OCS enhancement in plume (e.g., Bingemer et al., 2001)
In cases where OCS emissions are reported as an enhancement over background values, we divide the enhancement in the volumetric mixing ratio of OCS by the enhancement in CO.

As before, where multiple fires are given, we compute the emission ratio using the same sample for OCS and CO.

Example: Bingemer et al. (1992) compare mixing ratios of OCS and CO_2 in the free troposphere to two boundary layer measurements at different altitudes. The average of the resulting range ($[6.1 \text{ to } 41] \times 10^{-6}$ mol OCS / mol CO_2) is used in the Tropical Forest category.

2.7.3 Box Model Details

We use a one-box model of the global atmosphere to simulate the effect of different biomass burning emissions factors on OCS mixing ratios. The box model includes both concentration-independent (zero-order) and concentration-dependent (first-order) fluxes and was allowed to spin up for 20 years at monthly timesteps from a constant mixing ratio of 500 ppt in until 1980 when annually varying inventories of OCS emissions from anthropogenic activity are first available.

In each version of the model we repeat an average (1997 - 2016) of the estimated biomass burning fluxes until 1997, after which we use the time-varying biomass burning fluxes based on GFED4 burned dry matter. These fluxes are based on emission factors for CO provided in the GFED documentation and emission ratios of OCS relative to CO from either (i) Andreae and Merlet (2001) and Akagi et al. (2011) or (ii) the inventory calculated in the main text. In case (i), the biomass burning source ranges from 112 Gg (S) yr^{-1} to 815 Gg (S) yr^{-1}, with a mean flux of 242 Gg (S) yr^{-1}. In case (ii), the source ranges from 46 Gg (S) yr^{-1} to 111 Gg (S) yr^{-1}, with a mean flux of 60 Gg (S) yr^{-1}.

Biofuel emissions are based on a total of 21 Gg (S) yr^{-1} as calculated from Andreae (2019). This flux is implemented as an aseasonal, zero-order source.

Anthropogenic emissions are based on an inventory from Zumkehr et al. (2017). As these fluxes vary on a yearly (rather than monthly) basis, we distribute the fluxes evenly over the year. Since these data are available from 1980 to 2012, we repeat the estimated fluxes from 1980 for years prior to 1980, and we repeat the estimated anthropogenic fluxes from 2012 for years after 2012. Emissions in this inventory range from 311 Gg (S) yr^{-1} to 409 Gg (S) yr^{-1} with a mean value of 359 Gg (S) yr^{-1}.

We include a concentration-dependent OH sink with a rate constant derived to yield 110 Gg (S) yr^{-1} of uptake given an ambient concentration of 520 ppt (estimated total burden of 2995 Gg S), consistent with modeling conducted by Kuai et al. (2015). Concentrations during the model run yield an OH sink ranging from 100 Gg (S) yr^{-1} to 108 Gg (S) yr^{-1}, with a mean of 103 Gg (S) yr^{-1}.

Soil uptake is based on monthly varying, concentration-independent fluxes from 2006 as computed with the ecosystem model SiB4, repeated each year. Annual uptake from soils is estimated by SiB4 at 176 Gg (S) yr^{-1}. This value is between the estimates of 130 Gg (S) yr^{-1} from Kettle et al. (2002) and 355 Gg (S) yr^{-1} used in Berry et al. (2013). Although the soil flux is parameterized in SiB as a zero-order sink, Conrad (1994) and Whelan et al. (2016) show that the flux is in fact first-order.

Plant uptake fluxes in the model are also based on monthly totals from 2006 from SiB4 but are scaled by the ratio of the current time step's concentration to 450 ppt (the concentration at which SiB was run) to account for linear dependence on atmospheric concentration of OCS. As SiB was run with a fixed concentration, this correction is necessary to account for the concentration dependence. We note that, had plant fluxes been implemented without this correction, the large changes in concentration in the model using previous emission factors would be even more dramatic than reported in the text. The resulting plant uptake in the model varies from 815 Gg (S) yr^{-1} to 878 Gg (S) yr^{-1}, with a mean value of 841 Gg (S) yr^{-1}.

Ocean fluxes are implemented in the model as an aseasonal, zero-order source with total annual emissions (both directly as OCS and indirectly from CS_2 and DMS) of 485 Gg (S) yr^{-1}, as calculated by Lennartz et al. (2017, 2019).

In addition to these fluxes, we include a constant, concentration-independent flux to close the average annual budget, with a magnitude set such that concentrations in 1996 reach 500 ppt before divergent biomass burning emissions scenarios begin in 1997. 500 ppt was chosen for this point and for the initial condition as it is commonly cited as the average atmospheric mixing ratio of OCS (Asaf et al., 2013; Blake et al., 2004; Khalil & Rasmussen, 1984; Kuai et al., 2014).

Previous studies (Berry et al., 2013; Campbell et al., 2008; Suntharalingam et al., 2008) attribute this supplemental source to uncertainty in the ocean source, which typically exhibits low interannual variation. However, Lennartz et al. (2017, 2019) show that, while the ocean source is larger than that presented by Kettle et al. (2002), it is insufficiently large to close the budget gap.

Although the budget in the model using previous emission factors is nearly closed (requiring a supplemental flux of only 14.5 Gg (S) yr^{-1}), the disagreement with observed concentration trends excludes this scenario as a viable solution. In contrast, the model using the emissions computed in this work (which better match the bottom-up and top-down observational constraints) requires a supplemental flux of 197 Gg (S) yr^{-1} to close the budget.

In comparing model output with observational datasets, we focus primarily on relative changes in concentration, as differences in standards and calibration methods between studies could hamper our ability to predict absolute concentrations.

Uncertainties are calculated based on the standard deviations of observed emission factors and emission ratios. For each category of burning, we add the relative uncertainties for the CO emission factors (computed as the mean value reported by GFED divided by the uncertainty reported in Akagi et al. (2011)) and the OCS emission ratios calculated here (computed as the mean value divided by the standard deviation in the observations for that category) in quadrature, then multiply this combined value against each category of OCS emissions.

The corresponding range in estimates is shown in the error bars in Figure 2-2d. Using these high and low biomass burning estimates and compensating with changes in the supplemental flux, we run two additional iterations of the model to yield the shaded region in Figure 2-3a.

2.7.4 Availability of Gridded Data

Files generated for use in this work are available at https://portal.nersc.gov/project/m2319/. We provide NetCDF files for each year of OCS fluxes at monthly timesteps and 2° x 2.5° resolution. These files are based on the GFED datasets scaled by GFED's recommended EFs for CO (all available https://www.globalfiredata.org/), then to OCS using the molar emission ratios presented in this study. Uncertainty totals (based on relative uncertainty of the CO or CO_2 emission factors and OCS emission ratios, as described in the main text) of each category are also included. A corresponding set of files using CO_2 emission ratios is available in the same directory.

All units are g S-OCS km^{-2} month^{-1} and the variables in each file are as follows:

flux_sava – OCS flux from savanna burning
flux_borf – OCS flux from boreal forest burning
flux_temf – OCS flux from temperate forest burning
flux_defo – OCS flux from tropical deforestation and degradation
flux_peat – OCS flux from peatland burning
flux_agri – OCS flux from agriculture burning
flux_total – Sum of OCS fluxes over all six categories

unc_sava – Uncertainty in OCS savanna emissions
unc_borf – Uncertainty in OCS boreal forest emissions
unc_temf – Uncertainty in OCS temperate forest emissions
unc_defo – Uncertainty in OCS tropical emissions
unc_peat – Uncertainty in OCS peat emissions
unc_agri – Uncertainty in OCS agriculture emissions
unc_total – Sum of uncertainty across all six categories

Positive fluxes indicate a flux *into* the atmosphere.

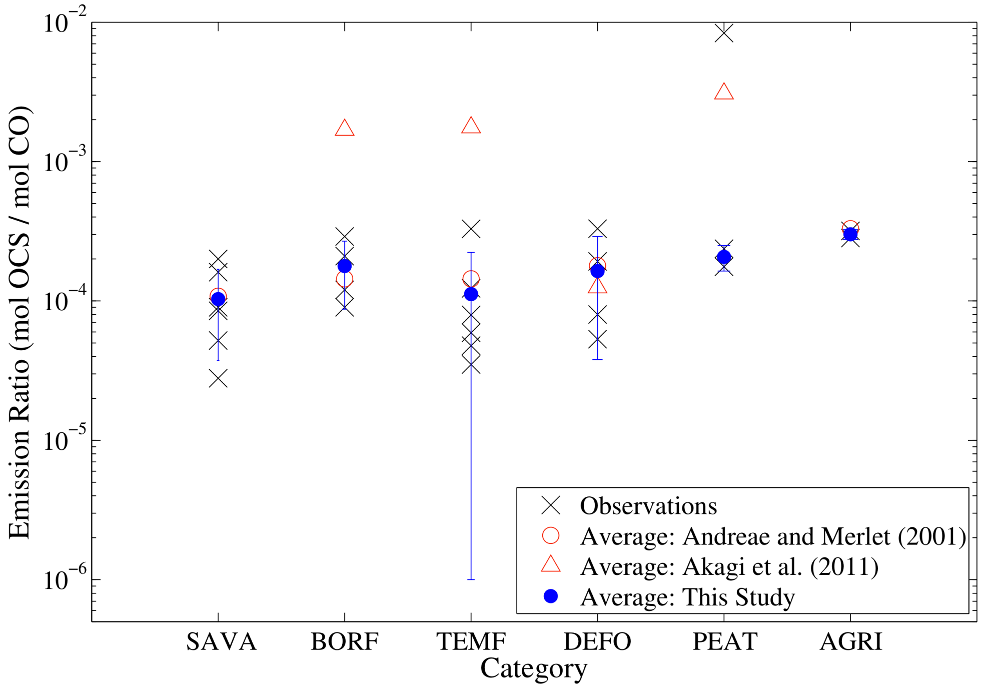

Figure 2-5: Results from Figure 2-1 comparing emission ratios in literature, plotted on a logarithmic scale.

Table 2-1: Emissions factors and ratios as reported in existing literature. DM = dry matter.

Source	Type / Location	Reported values	Computed/Reported ER
Primary data, convertible to OCS / CO and/or OCS / CO_2			
Akagi et al. (2013)	Extratropical Forest Prescribed Fires South Carolina Field Experiment	Ground-based (average values) 0.122 ± 0.187 g OCS / kg DM 1452 ± 130 g CO_2 / kg DM 173 ± 43 g CO / kg DM Airborne (average values) 0.01 ± 0.003 g OCS / kg DM 1675 ± 42 g CO_2 / kg DM 79 ± 19 g CO / kg DM	Ground-based 3.29×10^{-4} mol OCS / mol CO 6.16×10^{-5} mol OCS / mol CO_2 Airborne 5.91×10^{-5} mol OCS / mol CO 4.38×10^{-6} mol OCS / mol CO_2
Andreae 1996* [cited in Delmas 1995 as Andreae 1995b] [Table 27.8 in *Biomass Burning and Global Change* v.1]	Tropical Savanna Ivory Coast Field Experiment (SAFARI 92)	0.01 mol OCS / 1000 mol CO_2 62 ± 10 mol CO / 1000 mol CO_2	1.61×10^{-4} mol OCS / mol CO 1×10^{-5} mol OCS / mol CO_2
Balachandran et al. (2013)	Temperate Forest (US)	Flaming: 0.0061 ± 0.0030 g OCS / kg DM 48.08 ± 35.02 g CO / kg DM 1425.14 ± 63.78 g CO_2 / kg DM Smoldering: 0.0088 ± 0.0003 g OCS / kg DM 133.30 ± 54.16 g CO / kg DM 1324.67 ± 88.28 g CO_2 / kg DM	Flaming: 5.92×10^{-5} mol OCS / mol CO 3.14×10^{-6} mol OCS / mol CO_2 Smoldering: 3.08×10^{-5} mol OCS / mol CO 4.87×10^{-6} mol OCS / mol CO_2 Andreae 2019 uses 60/40 flaming/smoldering average 0.00718 g OCS / kg DM 4.784×10^{-5} mol OCS / mol CO 3.832×10^{-6} mol OCS / mol CO

Table 2-1 (continued)

Source	Type / Location	Reported values	Computed/Reported ER
Primary data, convertible to OCS / CO and/or OCS / CO_2			
Bingemer et al. (1992) (Only using for CO_2)	Tropical Forest Northern Congo Field Experiment (DECAFE 88)	6.1 to 41 × 10^{-6} mol OCS / mol CO_2 6.1 from 150m vs free trop (3660m) 41 from 1370m vs free troposphere (3660m)	6.1 - 41 × 10^{-6} mol OCS / mol CO_2 Avg 2.355 × 10^{-5} mol OCS / mol CO_2
Blake et al. (2008) Page 3 / Paragraph 17	Boreal Forest Flight 9 (Newfoundland) Plume from Alaska (INTEX-NA) Field Experiment	12-20 × 10^{-6} mol OCS / mol CO_2 0.09 × 10^{-3} mol OCS / mol CO (range 0.07 to 0.11) (Correcting exponent in paper per correspondence with authors)	9 × 10^{-5} mol OCS / mol CO (range 7 to 11) 12-20 × 10^{-6} mol OCS / mol CO_2
Crutzen et al. (1979) Table 2 Using Wild Basin Fire data only.	Extratropical Forest Wild Basin, CO Forest Fire Field Experiment	15.8 × 10^{-6} mol OCS / mol CO_2 (range 5.4 to 28.6) 19.9 mol CO / 100 mol CO_2 (range 15.8 to 25.1)	7.94 × 10^{-5} mol OCS / mol CO Based on Wild Basin Fire 1.13 × 10^{-4} mol OCS / mol CO Using average CO value 15.8 × 10^{-6} mol OCS / mol CO_2 (range 5.4 to 28.6)

Table 2-1 (continued)

Source	Type / Location	Reported values	Computed/Reported ER
Primary data, convertible to OCS / CO and/or OCS / CO_2			
Crutzen et al. (1985) Using arithmetic means	Tropical Forest / Grass Amazon / Brazil Field Experiment [Canned samples]	Geometric Mean: 4.7×10^{-6} mol OCS / mol CO_2 Range: 1.5 to 15 × 10^{-6} Arithmetic Mean: 8.2×10^{-6} Arithmetic SD: 7.5×10^{-6} Thornton lists the OCS/CO_2 range as well as the reported arithmetic mean. Geometric Mean: 0.121 mol CO / mol CO_2 Range: 0.06 to 0.24 Arithmetic Mean: 0.154 Arithmetic SD: 0.1 Text later averages arithmetic and geometric means for N_2O	Dividing arithmetic means: 5.32×10^{-5} mol OCS / mol CO 8.2×10^{-6} mol OCS / mol CO_2 (range 1.5 to 15)
Friedli et al. (2001) Using temperate composite for this category	Temperate Forest Temperate Composite 2 CO, 2 MT fires Field Experiment	Table 1: 0.123×10^{-3} mol OCS / mol CO for temperate composite Table 12: Reports 125×10^{-6} mol OCS/mol CO for temperate, as well as global total emission of 36.25×10^{9} g OCS / yr based on CO total in Koppmann 1997 Table 5; (extratropical forest CO emission of 58 Tg C / yr).	1.23×10^{-4} mol OCS / mol CO for “ temperate composite”

Table 2-1 (continued)

Source	**Type / Location**	**Reported values**	**Computed/Reported ER**
Primary data, convertible to OCS / CO and/or OCS / CO_2			
Friedli et al. (2001) Using CA sage scrub for this category	Grassland 1 CA fire Riversidean Sage Scrub Field Experiment	Table 1: 0.090×10^{-3} mol OCS / mol CO for CA fire	9.0×10^{-5} mol OCS / mol CO for CA fire
Lacaux 1993 [in *Fire and the Environment*] Same values in Lacaux 1995 (which was cited in Delmas 1995)	Tropical Savanna Ivory Coast / Africa Field Experiment (FOS-DECAFE 91)	1.7×10^{-6} mol OCS / mol CO_2 0.02-0.04 × 10^6 tons OCS in Africa 0.04-0.06 × 10^6 tons OCS global 61×10^{-3} mol CO / mol CO_2 29-56 × 10^6 tons CO in Africa 56-83 × 10^6 tons CO global	2.79×10^{-5} mol OCS / mol CO 1.7×10^{-6} mol OCS / mol CO_2
Liu et al. (2017) Only using Rim Fire data	Extratropical Forest Rim Fire, CA Field Experiment	$5.9 \pm 0.9 \times 10^{-3}$ g OCS / kg DM 78.7 (4.0) g CO / kg DM [Rim Fire only] 1478 (11) g CO_2 / kg DM [Rim Fire only]	3.50×10^{-5} mol OCS / mol CO 2.93×10^{-6} mol OCS / mol CO_2
Meinardi et al. (2003) Paragraph 10 (Only using for CO)	Australian brush fire Ground samples Field Experiment (BIBLE-B)	5.4×10^{-5} mol OCS / mol CO OCS observed only during smoldering	5.4×10^{-5} mol OCS / mol CO No significant correlation with CO_2

Table 2-1 (continued)

Source	Type / Location	Reported values	Computed/Reported ER
Primary data, convertible to OCS / CO and/or OCS / CO_2			
Nguyen et al. (1994) Table 3 Using average of wet and dry season values	Agriculture / Tropical Forest Vietnam Field Experiment	Dry season rice straw $37.4 \pm 41.1 \times 10^{-6}$ OCS/CO_2 0.13 ± 0.10 CO/CO_2 Wet season rice straw $78.2 \pm 31.4 \times 10^{-6}$ OCS/CO_2 0.28 ± 0.11 CO/CO_2 [Exponents are shifted in the table header. Compare to text.]	Dry season 2.87×10^{-4} mol OCS / mol CO $37.4 \pm 41.1 \times 10^{-6}$ mol OCS / mol CO_2 Wet season 2.79×10^{-4} mol OCS / mol CO $78.2 \pm 31.4 \times 10^{-6}$ mol OCS / mol CO_2
Nguyen et al. (1995)	Savanna Ivory Coast Field Experiment	Table 2: Mean: $11.4 \pm 15.1 \times 10^{-6}$ mol OCS / mol CO_2 Range: 3 to 61×10^{-6} mol OCS / mol CO_2 Also provides estimates for Vietnam rice (mean 3.2, range 1.2 to 4.9) and two lab experiments of savanna plants (14.3 and 2.0)	8.5×10^{-5} mol OCS / mol CO 11.4×10^{-6} mol OCS / mol CO_2
Simpson et al. (2011)	Boreal Forest Canada Field Experiment (ARCTAS 2008)	$(0.12 \pm 0.02) \times 10^{-3}$ mol OCS / mol CO 0.029 ± 0.007 g OCS / kg DM 0.11 ± 0.07 mol CO / mol CO_2 113 ± 72 g CO / kg DM 1616 ± 180 g CO_2 / kg DM Total boreal 41 ± 26 Tg CO / yr Total boreal 10.5 ± 2.5 Gg OCS / yr	$(1.2 \pm 0.2) \times 10^{-4}$ mol OCS / mol CO 1.32×10^{-5} mol OCS / mol CO_2

Table 2-1 (continued)

Source	Type / Location	Reported values	Computed/Reported ER
Primary data, convertible to OCS / CO and/or OCS / CO_2			
Stockwell et al. (2016)	Ag Residue (Table S9) (also includes garbage and cooking) (NAMaSTE)	OCS: 4.93×10^{-2} (3.47×10^{-2}) g OCS / kg DM CO: 72.3 (23.9) g CO / kg DM CO_2: 1401 (68) g CO_2 / kg DM	3.18×10^{-4} mol OCS / mol CO 2.58×10^{-5} mol OCS / mol CO_2
Stockwell et al. (2016)	Tropical Peat Indonesia El Niño year 35 plumes	0.110 (0.036) g OCS / kg DM 291 (49) g CO / kg DM 1564 (77) g CO_2 / kg DM	1.76×10^{-4} mol OCS / mol CO 5.16×10^{-5} mol OCS / mol CO_2
Tereszchuk et al. (2011)	Tropical Forest Amazon Plume - Table 1	3.3×10^{-4} mol OCS / mol CO	3.3×10^{-4} mol OCS / mol CO
Tereszchuk et al. (2011)	Tropical Forest Congo Plume - Table 1	8×10^{-5} mol OCS / mol CO	8×10^{-5} mol OCS / mol CO
Tereszchuk et al. (2011)	Savanna Northern Australia Plume Table 1	2×10^{-4} mol OCS / mol CO	2×10^{-4} mol OCS / mol CO
Tereszchuk et al. (2011)	Boreal Forest Canada Plume - Table 1	2.1×10^{-4} mol OCS / mol CO	2.1×10^{-4} mol OCS / mol CO

Table 2-1 (continued)

Source	Type / Location	Reported values	Computed/Reported ER
Primary data, convertible to OCS / CO and/or OCS / CO_2			
Thornton et al. (1996) Table 3 / Page 1878 Text / Page 1875 (Only used for CO_2)	Tropical Forest 2 plumes sampled over Pacific Field Experiments (PEM West-A)	13×10^{-6} mol OCS / mol CO_2	13×10^{-6} mol OCS / mol CO_2
Yokelson et al. (1997) Table 1 Only using Alaska peat value in average.	Boreal Peat MN and AK Lab Experiments	Minnesota: 493.7 g C / kg dm 0.127 mol OCS / 100 mol C 15.2 mol CO / 100 mol C 78.5 mol CO_2 / 100 mol C Alaska: [no estimate of C/DM] 0.005 mol OCS / 100 mol C 21.1 mol CO / 100 mol C 75.6 mol CO_2 / 100 mol C MN C x MN OCS 3.13 g OCS / kg DM MN C x AK OCS 0.12 g OCS / kg DM Average (1.62) and range (3.01) used in " boreal peat" component of Akagi 2011' s factors.	MN: 8.36×10^{-3} mol OCS / mol CO 1.62×10^{-3} mol OCS / mol CO_2 AK: 2.37×10^{-4} mol OCS / mol CO 6.61×10^{-5} mol OCS / mol CO_2

Table 2-1 (continued)

Source	Type / Location	Reported values	Computed/Reported ER
Primary data, convertible to OCS / CO and/or OCS / CO_2			
Yokelson et al. (2007) [cited in Yokelson 2008] Only using same-flight CO and CO_2 data.	Tropical Forest One planned fire / Brazil Field Experiment (TROFFEE 2004)	0.0247 g OCS / kg DM 59.91 g CO / kg DM (same fire/flight) 101.41 ± 23.78 g CO / kg DM (average) 1679 g CO_2 / kg DM (same fire/flight) 1615 ± 40 g CO_2 / kg DM (average) Yokelson et al. (2008) also scale this up to an Amazon total of 0.0119 Tg (240 Tg DM), global total of 0.0329 Tg (1330 Tg DM)	1.92×10^{-4} mol OCS / mol CO (using same-flight CO) 1.08×10^{-5} mol OCS / mol CO_2 (using same-flight CO_2) 1.14×10^{-4} mol OCS / mol CO (using average CO) 1.12×10^{-5} mol OCS / mol CO_2 (using average CO_2)
Primary data excluded from analysis			
Blake et al. (2004)	Asian Anthropogenic and Biomass burning Field experiment (TRACE-P 2001) Note: these seem to include biofuel and other sources	Table 2 22 (7 - 46) × 10^{-6} mol OCS / CO_2 0.75 (0.35 - 0.96) × 10^{-3} mol OCS / CO Also provides global BMB OCS totals from Watts 2000 (70Gg), Khalil 1984 (200 Gg) and Chin 1993 (140 Gg)	Excluded from analysis because signal includes biofuels.

Table 2-1 (continued)

Source	Type / Location	Reported values	Computed/Reported ER
Primary data excluded from analysis			
Blake / Simpson FLAME4 Data Personal communication with Isobel Simpson	Canadian / Indonesian Peat Flight / field measurement	Canadian Peat OCS / CO = 1.36×10^{-4} OCS / CO_2 = 3.32×10^{-5} CO / CO_2 = 0.245 Indonesian Peat: OCS / CO = 9.68×10^{-6} OCS / CO_2 = 2.79×10^{-6} CO / CO_2 = 0.288	Excluded from analysis because only one or two samples are available.
Nguyen 1990 Cited in Chin 1993 and Akeredolu 1991	Savanna / forest Ivory Coast / Nigeria Field Experiment	3 to 20 × 10^{-6} mol OCS / mol CO_2 Reported in Chin 1993 10.08×10^{-6} mol OCS / mol CO_2 5.4×10^{-4} Tg OCS (savanna) 2.5×10^{-4} Tg OCS (forest) Reported in Akeredolu 1991	Excluded from analysis -- Data included in Nguyen 1995
Yokelson et al. (1997) Table 3 [cited in Yokelson et al. (1999) and Goode et al. (2000)]	Average Lab Experiments	0.04 mol OCS / 100 mol CO	4×10^{-4} mol OCS / mol CO
Zhuang 1996 [T 71.3] [In *Biomass Burning and Global Change* v.2]	Crop Residue China Lab Experiment	Maize: 2.75 ± 0.23 g OCS/ton (n=7) Rice: 1.80 ± 0.12 g OCS / ton (n=9) Wheat: 2.05 ± 0.19 g OCS / ton (n=7)	Excluded from analysis -- no CO or CO_2 relationship available.

Table 2-1 (continued)

Source	Type / Location	Reported values	Computed/Reported ER
Summary papers, some with OCS vs. CO comparison			
Akeredolu 1991 Citing Nguyen 1990 [in *Global Biomass Burning*]	SUMMARY Tropical Savanna / Forest Nigeria	0.1 mol CO / mol CO_2 based on Greenberg et al. (1984) and Crutzen et al. (1979) 2.4 Tg CO (savanna) 1.1 Tg CO (forest)	1.08×10^{-4} mol OCS / mol CO Using OCS value from Nguyen 1990 and CO value from Greenberg et al. (1984) and/or Crutzen et al. (1979)
Andreae 1991 [in *Global Biomass Burning*]	SUMMARY	OCS 0.01 × 10-3 mol OCS / mol CO_2 0.02 g OCS / kg DM 0.04 Tg (Africa savanna) 0.07 Tg (global savanna) 0.21 Tg biomass burning 0.38 Tg all anthropogenic (based on Chin and Davis 1993) CO 62 × 10-3 mol CO / mol CO_2 65 g CO / kg DM 130 Tg African savanna 240 Tg global savanna 680 Tg biomass burning 1600 Tg all anthropogenic based on Houghton 1995 Table 1.4 gives OCS (field) 0.005 to 0.016 × 10-3 mol OCS / mol CO_2 CO (field) 65 to 140 mol CO / 1000 mol CO_2 CO (lab) 59 to 105 mol CO / 1000 mol CO_2	1.6×10^{-4} mol OCS / mol CO

Table 2-1 (continued)

Source	**Type / Location**	**Reported values**	**Computed/Reported ER**
Summary papers, some with OCS vs. CO comparison			
Andreae & Merlet (2001)	SUMMARY	g OCS / kg DM Savanna: 0.015 ± 0.009 Tropical: 0.04 Extratropical: 0.030-0.036 [using 0.033] Biofuel: 0.04 Charcoal Making: 0.04 Charcoal Burning: 0.04 Ag Waste: 0.065 ± 0.077 g CO / kg DM Savanna: 65 ± 20 Tropical: 104 ± 20 Extratropical: 107 ± 37 Biofuel: 78 ± 31 Charcoal Making: 70 Charcoal Burning: 200 ± 38 Ag Waste: 92 ± 84 g CO_2 / kg DM Savanna: 1613 ± 95 Tropical: 1580 ± 90 Extratropical: 1569 ± 131 Biofuel: 1550 ± 95 Charcoal Making: 440 Charcoal Burning: 2611 ± 241 Ag Waste: 1515 ± 177	mol OCS / mol CO Savanna: 1.08 × 10-4 Tropical: 1.79 × 10-4 Extratropical: 1.44 × 10-4 Biofuel: 2.39 × 10-4 Charcoal Making: 2.67 × 10-4 Charcoal Burning: 9.33 × 10-5 Ag Waste: 3.30 × 10-4 mol OCS / mol CO_2 Savanna: 6.82 × 10-6 Tropical: 1.86 × 10-5 Extratropical: 1.54 × 10-5 Biofuel:1.89 × 10-5 Charcoal Making: 6.67 × 10-5 Charcoal Burning: 1.12 × 10-5 Ag Waste: 3.15 × 10-5

Table 2-1 (continued)

Source	Type / Location	Reported values	Computed/Reported ER
Summary papers, some with OCS vs. CO comparison			
Chin & Davis (1993)	SUMMARY	0.14 (0.04-0.26) Tg (OCS) / yr Based on Crutzen 1979, Crutzen 1985, Bingemer 1990, Nguyen 1990 for OCS Based on Andreae 1991, Crutzen 1990 for C emissions.	
Crutzen & Andreae (1990) Cited in Crutzen 1993	SUMMARY Global biomass burning	0.01 ± 0.005 mol OCS / 100 mol CO_2 0.04-0.2 Tg S OCS from BMB 0.6-1.5 Tg S OCS from all sources 10 ± 5 mol CO / 100 mol CO_2 120-510 Tg CO from BMB 600-1300 Tg CO from all sources	1×10^{-5} mol OCS / mol CO
Khalil & Rasmussen (1984)	SUMMARY	200 Gg OCS based on Crutzen 1979 15.8×10^{-6} OCS/CO_2	

Table 2-1 (continued)

Source	Type / Location	Reported values	Computed/Reported ER
Summary papers, some with OCS vs. CO comparison			
Taylor and Zimmerman 1991 [in *Global Biomass Burning*]	SUMMARY	Total Methane 63.4 × 10^{12} g CH_4 Based on Crutzen 1979 and Greenberg 1984 9.88×10^{-4} mol OCS / mol CH_4 Total 0.13 × 10^{12} g S From Crutzen 8.75 mol CO / mol CH_4 => 971 × 10^{12} g CO from Crutzen 12.9 mol CO / mol CH_4 => 1431 × 10^{12} g CO from Greenberg	1.1×10^{-4} mol OCS / mol CO Differs from published estimate because Taylor uses the average CO and CH_4 values, rather than just the Wild Basin Fire ones.
Watts (2000)	SUMMARY	Text page 765 gives 0.11 Tg/yr OCS based on Kelly and Smith 1990 0.14 ± 0.12 Tg/yr OCS based on Chin and Davis 1993 0.07 ± 0.05 Tg/yr OCS based on Nguyen 1995 Table 4 gives 0.07 ± 0.05 Tg/yr OCS based on Nguyen 1995	

Table 2-2: Summary of literature estimates assigned to ecosystem categories for this work.

GFED Category	**Primary Data mol OCS / mol CO**	**Primary Data mol OCS / mol CO_2**	**Estimates from Akagi 2011 and/or Andreae 2001**
Savanna (SAVA)	Andreae 1996: 1.61×10^{-4} Lacaux 1993: 2.79×10^{-5} Meinardi 2003: 5.2×10^{-5} Nguyen 1995: 8.5×10^{-5} Friedli 2001: 9.0×10^{-5} (scrub) Tereszchuk 2011: 2.0×10^{-4} Average: 1.03×10^{-4} SD: 6.56×10^{-5}	Andreae 1996: 1×10^{-5} Lacaux 1993: 1.7×10^{-6} Nguyen 1995: 11.4×10^{-6} Average: 7.70×10^{-6} SD: 5.24×10^{-6}	Andreae: 1.08×10^{-4} mol OCS / mol CO Andreae: 6.82×10^{-6} mol OCS / mol CO_2
Boreal Forest (BORF)	Blake 2008: 9×10^{-5} (7-11) Rinsland 2007: $2.9 \pm 0.8 \times 10^{-4}$ Simpson 2011: $1.2 \pm 0.2 \times 10^{-4}$ Tereszchuk 2011: 2.1×10^{-4} Average: 1.78×10^{-4} SD: 9.07×10^{-5}	Blake 2008: 16 (12-20) $\times 10^{-6}$ Simpson 2011: 1.32×10^{-5} Average: 1.46×10^{-5} SD: 1.98×10^{-6}	Andreae: 1.44×10^{-4} mol OCS / mol CO " Extratropical" Akagi: 1.69×10^{-3} mol OCS / mol CO Average: 9.17×10^{-4} mol OCS / mol CO Andreae: 1.54×10^{-5} mol OCS / mol CO_2 " Extratropical" Akagi: 2.27×10^{-4} mol OCS / mol CO_2 Average: 1.21×10^{-4} mol OCS / mol CO_2
Temperate Forest (TEMF)	Akagi 2013: 3.29×10^{-4} (ground) Akagi 2013: $5.91 \times 10^{-4}5$ (air) Crutzen 1979: 7.94×10^{-5} Liu 2017: 3.50×10^{-5} Friedli 2001: 1.23×10^{-4} (temp) Balachandran 2013: 4.78×10^{-5} (60/40) Average: 1.12×10^{-4} SD: 1.11×10^{-4}	Akagi 2013: 6.16×10^{-5} (ground) Akagi 2013: 4.38×10^{-6} (air) Crutzen 1979: 15.8×10^{-6} Liu 2017: 2.93×10^{-6} Balachandran 2013: 3.83×10^{-6} (60/40) Average: 1.77×10^{-5} SD: 2.51×10^{-5}	Andreae: 1.44×10^{-4} mol OCS / mol CO " Extratropical" Akagi: 1.76×10^{-3} mol OCS / mol CO " Extratropical" Average: 9.52×10^{-4} mol OCS / mol CO Andreae: 1.54×10^{-5} mol OCS / mol CO_2 " Extratropical" Akagi: 2.24×10^{-4} mol OCS / mol CO_2 " Extratropical" Average: 1.20×10^{-4} mol OCS / mol CO_2

Table 2-2 (continued)

GFED Category	**Primary Data mol OCS / mol CO**	**Primary Data mol OCS / mol CO_2**	**Estimates from Akagi 2011 and/or Andreae 2001**
Tropical Forest (DEFO)	Crutzen 1985: 5.32×10^{-5} Yokelson 2007: 1.92×10^{-4} Tereszchuk 2011: 3.3×10^{-4} (Amazon) Tereszchuk 2011: 8.0×10^{-5} (Congo) Average: 1.64×10^{-4} SD: 1.26×10^{-4}	Bingemer 1992: $6.1 - 41 \times 10^{-6}$ (avg 2.355×10^{-5}) Crutzen 1985: 8.2×10^{-6} Thornton 1996: 13×10^{-6} Yokelson 2007: 1.08×10^{-5} Average: 1.39×10^{-5} SD: 6.73×10^{-6}	Andreae: 1.79×10^{-4} mol OCS / mol CO Akagi: 1.25×10^{-4} mol OCS / mol CO Average: 1.52×10^{-4} mol OCS / mol CO Andreae: 1.85×10^{-5} mol OCS / mol CO_2 Akagi: 1.12×10^{-5} mol OCS / mol CO_2 Average: 1.49×10^{-5} mol OCS / mol CO_2
Peatland (PEAT)	Yokelson 1997 AK: 2.37×10^{-4} Stockwell 2016b: 1.76×10^{-4} Avg: 2.07×10^{-4} with Yokelson AK and Stockwell SD: 4.31×10^{-5} Excludes: Yokelson 1997 MN: 8.36×10^{-3} FLAME4 Canada: 1.36×10^{-4} FLAME4 Indonesia: 9.68×10^{-6}	Yokelson 1997 AK: 6.61×10^{-5} Stockwell 2016b: 5.16×10^{-5} Avg: 5.89×10^{-5} with Yokelson AK and Stockwell SD: 1.03×10^{-5} Excludes: Yokelson 1997 MN: 1.62×10^{-3} FLAME4 Canada: 3.32×10^{-5} FLAME4 Indonesia: 2.79×10^{-6}	Akagi: 3.08×10^{-3} mol OCS / mol CO Akagi: 5.6×10^{-4} mol OCS / mol CO_2
Agricultural Waste (AGRI)	Nguyen 1994: 2.83×10^{-4} Stockwell 2016a: 3.18×10^{-4} Average: 3.01×10^{-4} SD: 2.47×10^{-5}	Nguyen 1994: 5.78×10^{-5} Stockwell 2016a: 2.58×10^{-5} Average: 4.18×10^{-5} SD: 2.26×10^{-5}	Andreae: 3.30×10^{-4} mol OCS / mol CO Andreae: 3.15×10^{-5} mol OCS / mol CO_2

Table 2-3: Table of Values for Average ERs in Figure 2-1.

	SAVA	BORF	TEMF	DEFO	PEAT	AGRI
Andreae & Merlet, 2001	1.08×10^{-4}	1.44×10^{-4}		1.79×10^{-4}	NR	3.30×10^{-4}
Akagi et al., 2011	NR	1.69×10^{-3}	1.76×10^{-3}*	1.25×10^{-4}	3.08×10^{-3}	NR
Previous Study Average	1.08×10^{-4}	9.17×10^{-4}	9.52×10^{-4}	1.52×10^{-4}	3.08×10^{-3}	3.30×10^{-4}
This Paper	1.03×10^{-4}	1.78×10^{-4}	1.12×10^{-4}	1.64×10^{-4}	2.07×10^{-4}	3.01×10^{-4}

Emission ratios for 6 categories of burning included in GFED. Units are mol OCS / mol CO. Andreae and Merlet (2001) report a value for “extratropical forest” which we have used for both boreal and temperate forests. Akagi et al. (2011) provide a value for “extratropical forest” which we use for temperate forests. The Previous Study Average is the value used in the box model simulation and is equal to either the emission ratio from Andreae and Merlet (2001) or Akagi et al. (2011) (when only one study provides a value) or an evenly weighted average of emission ratios from both studies (when both studies report a value). NR = not reported.

*[9.28×10^{-5} in an updated version of the data maintained by the original authors and posted at http://bai.acom.ucar.edu/Data/fire/ (accessed 07/30/2019)]

Table 2-4: Summary of average annual OCS emissions (Gg (S) yr^{-1}) based on CO and CO_2 totals from all complete years of GFED data (1997-2016).

Category	**Current Study** **CO-based Estimate**	**Previous Studies** **CO-based Estimate**
SAVA	21.4 (18.7 - 27.2) ± 14.8	22.5 (19.6 - 28.5)
BORF	8.8 (4.7 - 18.0) ± 5.5	45.4 (24.2 - 92.5)
TEMF	1.1 (0.7 - 1.9) ± 1.2	9.6 (5.6 - 15.8)
DEFO	11.5 (5.2 - 22.4) ± 9.5	10.7 (4.8 - 20.7)
PEAT	7.0 (0.5 - 46.6) ± 2.5	104.2 (7.4 - 692.6)
AGRI	9.9 (7.4 - 13.2) ± 3.3	10.8 (8.2 - 14.5)
Total:	**59.8 (45.9 - 111.0) ± 36.7**	**203.1 (88.0 - 790.8)**
Category	**Current Study** **CO_2-based Estimate**	**Previous Studies** **CO_2-based Estimate**
SAVA	27.3 (23.8 - 34.6) ± 18.6	24.2 (21.0 - 30.7)
BORF	5.4 (2.9 - 11.0) ± 0.9	44.7 (23.8 - 91.1)
TEMF	2.1 (1.3 - 3.5) ± 3.0	14.3 (8.5 - 23.7)
DEFO	11.0 (4.9 - 21.3) ± 5.3	11.8 (5.3 - 22.8)
PEAT	10.3 (0.7 - 68.4) ± 1.8	97.8 (6.9 - 649.9)
AGRI	13.5 (10.2 - 18.2) ± 7.4	10.2 (7.7 - 13.7)
Total:	**69.6 (52.5 - 141.6) ± 37.0**	**203.0 (93.3 - 756.7)**

Minimum and maximum annual totals are given in parentheses. For estimates derived in this paper, uncertainty estimates based on the spread of observations are also given. Previous Studies refers to estimates from Andreae and Merlet (2001), Akagi et al. (2011) or an average of both, as described in the main text.

In general, both CO- and CO_2-based approaches show similar total emissions of OCS, but as CO_2 emission factors vary less between categories (standard deviation of CO_2 EFs across categories is 5% of mean, compared to 45% for CO), estimates based on CO_2 more closely follow the distribution of emissions shown in Figure 2-2a (Dry Matter Emissions by Category) in the main text.

Chapter 3: Remotely Sensed Carbonyl Sulfide Constrains Model Estimates of Amazon Primary Productivity

3.1 Abstract

Understanding the magnitude of tropical gross primary production (GPP) is critical for carbon cycle modeling, and hence future climate projections, but this quantity is poorly constrained at regional scales. One promising approach is the use of atmospheric carbonyl sulfide (OCS) uptake as a proxy for regional GPP. Here, we simulate OCS concentrations driven by surface flux scenarios encompassing a wide range of GPP estimates for the Amazon basin. We compare the transport model output to satellite retrievals and find a regional GPP estimate of 1051 ± 581 g C m^{-2} yr^{-1}, which is near the low end of previous estimates, including the TRENDY model range.

3.2 Background

Accurate quantification of photosynthetic carbon uptake (gross primary production, GPP) in the tropics is critical to improving ecosystem models and climate predictions. The net flux between respiration and GPP is relatively small relative to the magnitude of each component (e.g., Steffen et al., 1998), and changes in either component can lead to significant changes in the net carbon balance. As such, feedbacks between climate and GPP represent some of the largest sources of uncertainty in climate projections (Arneth et al., 2010; Wenzel et al., 2016). In order to address these uncertainties, it is arguably first necessary to accurately quantify GPP, estimates of which vary widely between models, particularly in the tropics (Figure 3-1).

Previous work has sought to constrain the magnitude of regional GPP estimates primarily by upscaling of eddy covariance (Beer et al., 2010; Jung et al., 2011) measurements or regression with solar-induced fluorescence (SIF) measurements (Frankenberg et al., 2011, 2012; Guanter et al., 2014; Parazoo et al., 2014; van der Tol et al., 2009). While much has been learned from such approaches, spatiotemporal uncertainties in regional GPP estimates persist; measurements of SIF represent photosynthetic activity only at a given instant, eddy covariance data is limited by the sparse network of sites, and remote sensing approaches in general often face complications from cloud contamination. These challenges suggest the need for a complementary approach that is integrative over space and time.

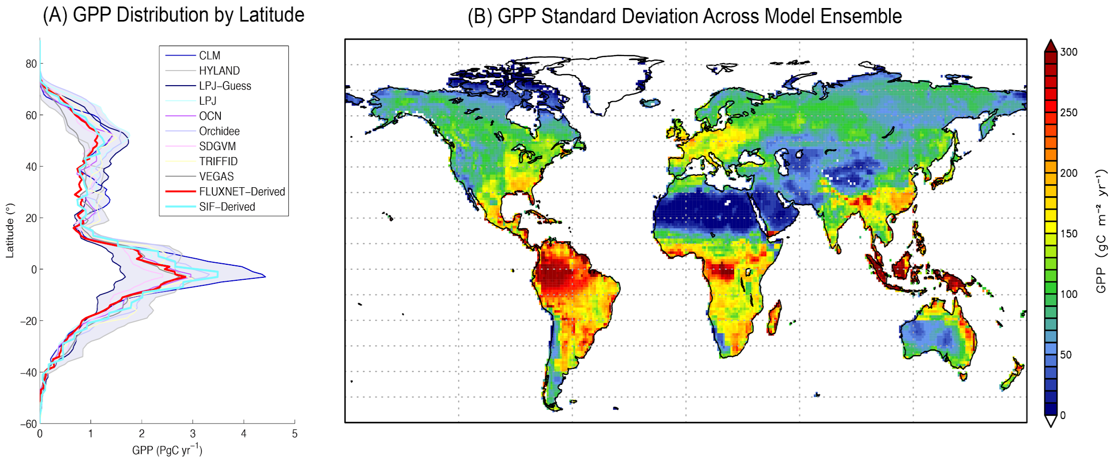

Figure 3-1: Variation of GPP within the TRENDY model ensemble expressed (*A*) by 1° latitudinal averages and (*B*) by standard deviation across models. Data are annual averages from the most recent simulation year in the Trendy data (2010). Also included in Figure 3-1a are observation-based GPP estimates from previously published flux tower (red, Beer et al., 2010) and solar-induced fluorescence (cyan, Parazoo et al., 2014) measurements.

One such approach involves the use of atmospheric carbonyl sulfide (OCS or COS) as a tracer for regional and global GPP (Berry et al., 2013; Campbell et al., 2008, 2017; Montzka et al., 2007). The primary OCS sink is terrestrial plant uptake, which is controlled by stomatal conductance and strongly correlated with GPP at regional scales (Berry et al., 2013; Hilton et al., 2017; Sandoval-Soto et al., 2005; Stimler et al., 2010). The primary sources are ocean chemical cycling and industrial activity (Campbell et al., 2015; Launois, Belviso, et al., 2015; Launois, Peylin, et al., 2015; Zumkehr et al., 2017, 2018). Soil uptake, soil efflux and emissions from biomass burning also contribute to the OCS budget (Kettle et al., 2002; Stinecipher et al., 2019; Whelan et al., 2016).

Although large-scale OCS analyses have thus far focused on global or North American domains (Berry et al., 2013; Campbell et al., 2008, 2017; Hilton et al., 2017; Wang et al., 2016), recently published satellite retrievals of OCS concentrations provide more detailed spatial coverage that may support a broader range of regional applications (Glatthor et al., 2015, 2017; Kuai et al., 2014, 2015; Vincent & Dudhia, 2017). Satellite OCS data over continental regions are currently available for the upper troposphere, which is generally too high of an altitude to be useful for inferring the land surface plant sink, unless there is sufficient convective transport (Figure 3-2).

Such meteorological conditions, however, are fortuitously met in the Amazon region, where satellite retrievals from the Michelson Interferometer for Passive Atmospheric Sounding (MIPAS) yield the lowest global OCS concentrations, consistent with both significant OCS uptake and strong convective transport (Figure 3-2a, see also Glatthor et al., 2015, 2017). The spatial separation of the dominant regional sink (plant uptake) from other regional sources (particularly ocean chemistry and industrial activity) further accentuates this gradient (Campbell et al., 2015; Glatthor et al., 2015).

In contrast, satellite-constrained model estimates of CO_2 concentrations in the upper troposphere do not show a similar drawdown over the Amazon, as the photosynthesis sink and respiration source are co-located (Figure 3-2b). Furthermore, even given sufficiently large changes in CO_2 concentrations (e.g., near the surface), these changes only represent the net carbon flux, without addressing the underlying components.

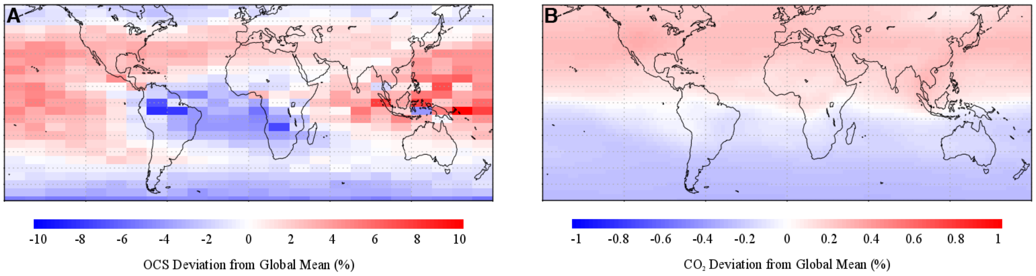

Figure 3-2: Upper troposphere measurements show stronger relative deviations in (***A***) OCS concentration from MIPAS (average binned observations, 2002 - 2012) compared to (***B***) CO_2 concentration from GOSAT's Level 4B product (averaged 2010 - 2013). Both plots express changes in concentration as percent deviation from the global annual mean at 250 hPa.

3.3 Methods

Here we seek to estimate the regional GPP flux that is most consistent with the large depletion of OCS over the Amazon and the tropical Atlantic identified by MIPAS, a limb-sounding instrument operating aboard the Envisat satellite from 2002 to 2012 (Glatthor et al., 2015, 2017). Glatthor et al. (2015) attribute this depletion to Amazonian plant uptake but do not provide an estimate for that uptake. We consider multiple scenarios for plant uptake of OCS in the Amazon basin, corresponding to the high and low extremes of the regional GPP fluxes from the TRENDY ecosystem model intercomparison project (Figure 3-1; see also Sitch et al., 2015).

A baseline set of OCS plant uptake fluxes is estimated from SIF-optimized GPP using the linear relationship between canopy OCS and GPP computed by the Simple Biosphere Model (SiB3). Using the linear relationship between GPP and OCS uptake, we scale these baseline plant fluxes in the Amazon region (defined for this purpose as extending from 7° N to 19° S and from 51.25° W to 76.25° W) to match the lowest and highest GPP estimates from the TRENDY ensemble. Although the relationship between OCS uptake and GPP depends on a variety of factors (including diurnal variation, ambient concentrations, humidity, stomatal conductance, and plant functional type), at aggregate spatial and temporal scales, the linear relationship is both strong and consistent with findings of Hilton et al. (2017) that mechanistically calculated OCS uptake and uptake computed from linearly scaled GPP yield similar results.

We simulate OCS concentrations in the atmosphere by running a modified version of the GEOS-Chem atmospheric transport and chemistry model with 2° latitude by 2.5° longitude resolution, 47 vertical levels and GEOS5 meteorology from 2004 to 2012 (Kuai et al., 2015; Suntharalingam et al., 2008). OCS was implemented with surface fluxes that are independent of the atmospheric OCS concentration and a first-order loss from reaction of OCS with the OH radical in the atmosphere, calculated from a prescribed OH field, following Kuai et al. (2015).

Retrieved MIPAS vertical profiles were quality-filtered based on averaging kernel weights and clear-sky flags and interpolated to 250 hPa as in Glatthor et al. (2015). 250 hPa was selected because it was the lowest altitude with near-complete global coverage when data are binned. Although MIPAS observations are available from 2002-2012, due to limitations in available meteorological data for our modeling, we exclude the first two years from the analysis.

To maintain consistent spatial weighting between the modeled and observed data, we sample the model output at the locations and times of MIPAS observations using a nearest-neighbor scheme. We combine all observations (and their corresponding model points) in a given month across the entire model period (e.g., all January observations, regardless of year). Although this yields estimates on a coarser, climatological timescale, it allows for the inclusion of far more points in each monthly average.

Glatthor et al. (2015) compare observed and modeled values within a fixed region, but preliminary tests found this approach to be too sensitive to the choice of boundaries for the current work. In order to increase the robustness of the estimate, we dynamically define signal and background regions as follows.

At each extracted point, we compute a "sensitivity ratio" R_{sens} by dividing the low-GPP model concentrations by the high-GPP model concentrations, akin to a Jacobian. As the primary difference between runs is the change in Amazon plant uptake fluxes, this ratio represents the change in concentration at a given point due to changes in surface fluxes. By aggregating and averaging points where R_{sens} is relatively large, we can determine the subset of upper-tropospheric observations most sensitive to plant uptake in the Amazon.

The value of this approach is highlighted in Figure 3-3. In months with sufficient convection (i.e., during the wet season), a strong signal region is identifiable downstream of the actual uptake, even though retrievals directly over the Amazon and elsewhere in the tropics are hampered by cloud cover. Conversely, during the dry season (shown here for July), more observations are available directly above the tropics, but are less affected by changes at the surface.

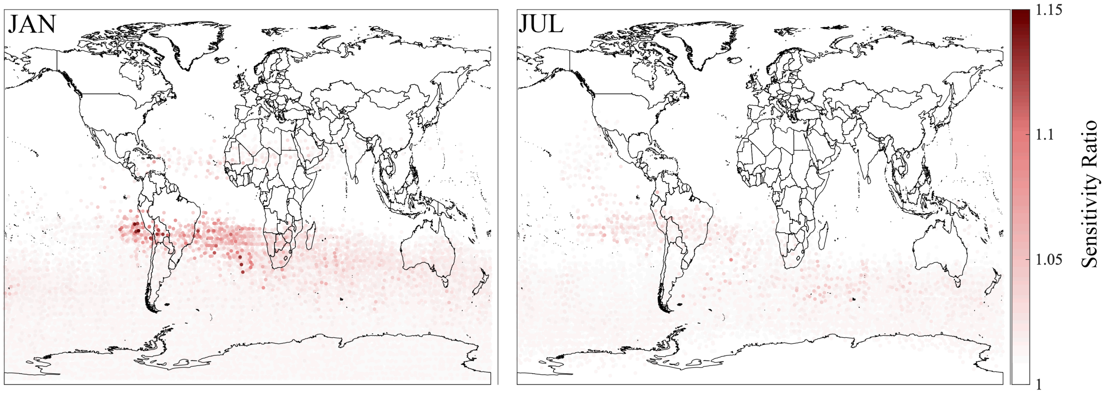

Figure 3-3: Sensitivity ratios indicate strong, decentralized influence of surface fluxes in January (left), but weaker influences in July (right). Values are the ratio of the low-GPP model concentration divided by the high-GPP model concentration at the location of each valid MIPAS OCS observation at 250 hPa. Values are aggregated over all model years (2004-2012).

We extract mean concentrations from two regions: a signal region sensitive to the Amazon (i.e., points with a high R_{sens} value) and a background region against which the former value can be standardized between datasets. We then relate the difference in mixing ratios between the regions to the monthly OCS fluxes in the Amazon by a linear regression. This procedure yields an estimate for the net OCS flux in the region for a given month, from which we subtract non-plant fluxes to obtain an estimate for the amount of OCS plant uptake responsible for the signal in the satellite data. We repeat the analysis across a range of thresholds to reduce bias from any particular choice of threshold values for R_{sens} and estimate the uncertainty in our method (see Section 3.7.2).

3.4 Results

Model results generally follow the observed seasonal pattern, with the low-GPP model yielding the best correspondence in overall magnitude. Figure 3-4 shows the mean difference in concentrations between the signal and background regions described above, and the resulting monthly flux estimates based on the regression. In the dry season (June through October), convection is limited and therefore fewer points during this period meet the sensitivity thresholds, making values highly uncertain.

While additional post-analysis sources of uncertainty are described below, monthly uncertainty shown in Figure 3-4 is computed as the sum of two factors: the standard error of the mean within each signal and background region, as well as the standard deviation of the estimates across all thresholds.

On average, observed concentrations in the signal region have a standard error of the mean (SEM) ranging from 3 to 21 ppt, depending on the month. In contrast, the average SEM for the background region is less than 1 ppt due to the vastly larger number of observations. This range in concentrations propagates to create a corresponding range of flux estimates with a relative error between 19% and 178% of each month's estimate.

The second source of uncertainty is the choice of threshold used to define the two averaging regions. Across the combinations of thresholds described above, we find a standard deviation between 17% and 136% of the estimated flux. The largest uncertainties occur during the dry season months due to limited convective transport, which reduces the number of upper troposphere observations sensitive to surface fluxes.

When added in quadrature, the uncertainties yield overall monthly relative errors between 28% and 188% of the monthly retrieved plant flux. As before, the largest combined uncertainties occur during the dry season.

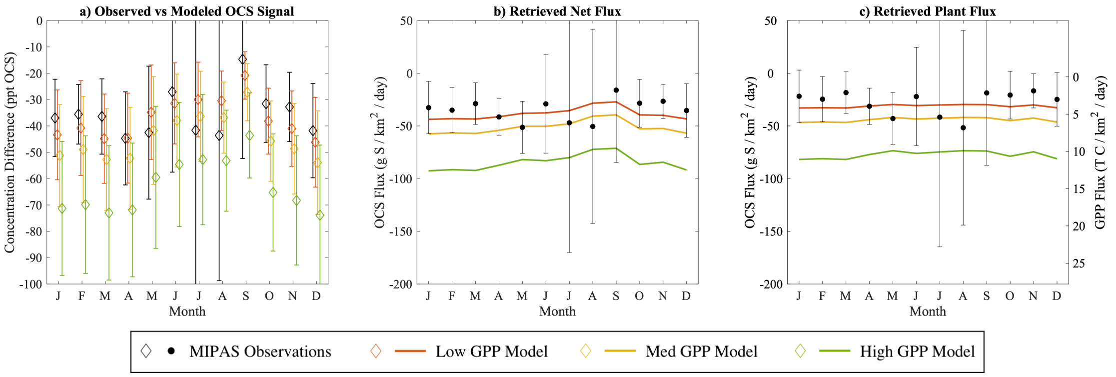

Figure 3-4: During months with sufficient convection, observed OCS concentrations are more consistent with values from lower GPP models. Average OCS concentrations in signal regions relative to background regions are shown in (**A**), with corresponding monthly estimates of net OCS flux (**B**) and plant-only OCS flux (**C**) for perturbed Amazon region. Error bars are 95% confidence intervals.

Given the large uncertainty from May to October, we estimate annual OCS fluxes using a weighted mean of the monthly plant flux with weights based on the squared inverse of the calculated monthly uncertainties. The months with the largest weights (November to April) correspond to the time when convection is strong enough to yield sufficient observations, while months with large uncertainty (July to September) contribute little information. Using this weighting, we obtain average plant fluxes of -70.7 ± 24.3 Gg S yr^{-1} and corresponding GPP fluxes of 8.6 ± 3.4 Pg C yr^{-1} using the OCS-GPP relationship from the flux generation step.

Several factors contribute additional uncertainty and bias to this initial estimate. These include uncertainty in the relationship between GPP and OCS uptake by plants, bias due to weighting and flux seasonality, surface flux uncertainty, and choice of transport model.

Uncertainty in the relationship between OCS uptake and GPP is difficult to quantify, given the lack of observational data in the region. We approach this uncertainty by considering the leaf-scale relative uptake (LRU), which is the ratio of OCS uptake to GPP, normalized by ambient concentrations. Hilton et al. (2017) argue that for seasonal analyses at regional scales, LRU represents a small source of uncertainty relative to other factors, particularly the spatial distribution of fluxes.

Over the region of interest, the baseline (medium) flux is 128 Gg S OCS corresponding to 17 Pg C GPP annually, as estimated using the SiB3 mechanistic model. Assuming an ambient concentration ratio of 1.1 pptv OCS / ppmv CO_2 (Hilton et al., 2017), this calculation yields an LRU of 2.6. This estimate is within the range of 1.7 to 3.6 that has been reported for tropical forests (See Table 3 of Sandoval-Soto et al., 2005). Given this overall range, we estimate a standard deviation of 0.475 and obtain a relative uncertainty of 18.2%, or 1.56 Pg C when applied to the retrieved GPP.

Models in the TRENDY ensemble tend to show a decrease in GPP during the months of low convection (May to October). As such, our weighting scheme favoring high-convection months may in fact be overestimating GPP. To assess this bias, we apply the same weighting to the suite of TRENDY models and compare the GPP calculated using both weighted and unweighted averages. Across all TRENDY models, the weighted average predicts GPP that is 0% to 6% higher than that calculated using all months of data, hence the estimate derived here may overestimate GPP by a similar amount. To account for this, we reduce the final weighted mean value by 3% while including a relative error of ± 3% (0.26 Pg C).

Uncertainties due to non-plant surface fluxes are relatively small. We estimate the standard deviation of the total range in non-plant fluxes as 10 Gg S yr^{-1} which, when compared to the range in regional plant fluxes, yields a corresponding uncertainty in GPP of 1.4 Pg C yr^{-1}.

While non-plant fluxes within the region of interest have a direct effect on the overall retrieval, the effect of these fluxes elsewhere in the globe is more like a representation error; although the overall total remains approximately the same, the spatial distribution is impacted. We compare the present model simulations with another set using larger biomass burning fluxes (based on scaling factors from Campbell et al., 2017) and smaller anthropogenic fluxes from Kettle et al. (2002), with corresponding changes to the supplemental ocean flux to balance the flux budget. Comparing the range in retrieved values to the overall range in plant fluxes, we estimate an uncertainty of 8.9 Gg S yr^{-1}, corresponding to 1.3 Pg C yr^{-1}.

Estimates of uncertainty due to different transport models are likewise small relative to the range of GPP estimates. An additional pair of runs was performed to test the sensitivity to different transport models. We ran the Parameterized Chemical Transport Model (PCTM, see Berry et al., 2013; Kawa, 2004) and a corresponding GEOS-Chem simulation with the same surface fluxes, for two years. The average

RMSE between models was 2.4 pptv. We compare this value to the average difference between the low- and high-GPP model depressions (25.9 pptv), which yields a corresponding uncertainty of approximately 1.8 Pg C yr^{-1} when compared to the underlying GPP values.

When added in quadrature, the overall estimate obtained is 8.3 ± 4.6 Pg C yr^{-1} (mean ± sd), or 1051 ± 581 g C m^{-2} yr^{-1}, which encompasses the lower end of estimates predicted by TRENDY.

3.5 Discussion

Concentrations within the signal region are generally lower than those in the background region because, by definition, the region is strongly influenced by plant uptake of OCS in the Amazon at the surface. In general, the signal region is also more uncertain than the background region, with fewer observations leading to standard errors of the signal mean an order of magnitude larger than that of the background. Additionally, since these signal regions include fewer total retrievals (each of which has associated noise and errors), the averages are more sensitive to changes in the thresholds. This highlights the need for more, higher-resolution satellite measurements of OCS over the tropics.

Net fluxes in the model increase between August and October due to increases in biomass burning. Biomass burning emissions show significant seasonal and interannual variation (Stinecipher et al., 2019); however, two factors mitigate sensitivities of our estimates to uncertainties in the location, timing and magnitude of our fire emissions. First, by attempting to constrain fluxes only on a climatological basis, we avoid the challenge of predicting fluxes in any particular year. Further, since the period when biomass burning spikes (the dry season) is also the same period where deep convection weakens, our model already shows little to no skill at differentiating between GPP scenarios at this time, and therefore these months already receive a low weighting.

Beyond the existing ecosystem model results, two independent approaches provide measurement-based context for this estimate of GPP. We calculate an additional constraint on GPP using estimates derived from the FLUXNET observation network, as described in Beer et al. (2010). Across the six approaches described in that paper, the mean GPP within the Amazon basin was determined to be 2604 g C m^{-2} yr^{-1} with a standard deviation of 253 g C m^{-2} yr^{-1}. We calculate a separate constraint for GPP based on solar-induced fluorescence observations from GOSAT from 2009-2013 (Parazoo et al., 2014), yielding 3060 g C m^{-2} yr^{-1}. These independent estimates, as well as the estimates computed above, are shown in Figure 3-5.

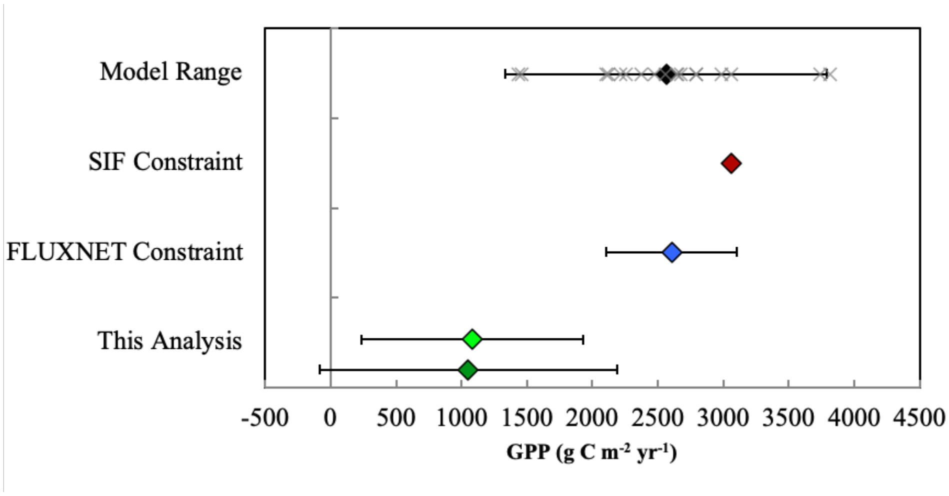

Figure 3-5: Our OCS-based estimates for GPP in the Amazon basin are more consistent with the lower-GPP TRENDY models. Grey crosses are individual TRENDY model averages over the last decade of simulation. Black diamond is the mean across all TRENDY models. Red diamond is GOSAT-observed SIF constraint from Parazoo et al. (2014). Blue diamond is FLUXNET constraint from Beer et al. (2010). MIPAS-based OCS constraint with errors based on those in Figure 3-4 (light green diamond) or with additional sources of error included and with mean shifted to account for seasonal bias (dark green diamond). Error bars represent 95% confidence intervals.

In light of these uncertainties, it remains challenging to use the MIPAS OCS dataset to estimate Amazonian carbon uptake for any given month or year. However, the current work demonstrates that this method can yield valuable information about regional GPP on a climatological timescale. These in turn could be used to calibrate short-term flux variability derived from emerging carbon cycle assimilation systems (e.g., Bowman et al., 2017, Liu et al., 2017), yielding a synthesis between instantaneous approaches like SIF and climatological information from OCS. The encouraging spatial patterns underscore both the importance of OCS as a tracer for primary productivity and stomatal conductance, as well as the need for additional measurements of OCS at higher spatial and temporal resolutions. Measurements at lower altitudes would further constrain estimates, especially during months with reduced convective transport.

3.6 Conclusion

This approach yields information about a region that other satellite products (SIF, NDVI) struggle to capture amid frequent cloud contamination. Even though few OCS observations are available directly above the Amazon, information is still available "downstream" of the region due to the spatially and temporally integrative nature of the tracer approach.

While much of the discussion on the global OCS budget has centered on missing sources (Lennartz et al., 2017; Stinecipher et al., 2019), we note that the smaller plant sink described here would also help to close the budget. This would reduce the need for a large, supplemental ocean source (e.g., Berry et al., 2013), consistent with recent analyses by Lennartz et al. (2017, 2019).

If our lower estimates of GPP are borne out in future, this result will have profound impacts on our understanding of the global carbon cycle, particularly the ability of tropical forests to sequester carbon.

3.7 Supplemental Information for Chapter 3

3.7.1 Details on GEOS-Chem Setup

Process Model Estimates of GPP

Process-based estimates of GPP were taken from the TRENDY Version 1 S1 and S2 datasets (Sitch et al., 2015), including the following models: CLM, HYLAND, LPJ-Guess, LPJ, OCN, ORCHIDEE, SDGVM, TRIFFID and VEGAS. Over the region of interest (76.25°W-51.25°W, 19°S-7°N), model estimates of GPP ranged from 11.3 Pg C yr^{-1} (LPJ-Guess) to 30.2 Pg C yr^{-1} (CLM), averaged over the most recent 10 years of simulation (2001 - 2010). See Figure 3-6, Panel (A).

OCS Transport Model Fluxes

Canopy Uptake: Initial estimates of OCS uptake by plants (totaling 691 Gg S yr^{-1} globally) followed spatial distributions of GPP inferred through solar-induced fluorescence (SIF) as measured by GOME-2 (Parazoo et al., 2014). Flux totals were calculated using the Simple Biosphere Model (SiB3); see Baker et al., 2008), which mechanistically simulates the relationship between regional GPP and OCS flux (Baker et al., 2008; Berry et al., 2013). These fluxes are scaled by atmospheric concentrations predicted from a previous GEOS-Chem simulation and normalized by the constant boundary layer value assumed by SiB (450 ppt). The unscaled (medium) total in the region of interest was 128 Gg S yr^{-1}, corresponding to 16.6 Pg C yr^{-1} in GPP.

Two additional sets of canopy fluxes were generated to conduct high- and low-productivity runs, based on end members in the TRENDY dataset (described above). We scale the canopy uptake in the region of interest based on the total GPP fluxes in this region from the LPJ-Guess and CLM models, yielding scaling factors of 0.7 and 1.8, respectively. This yielded regional plant sinks ranging from 90 to 224 Gg S yr^{-1}, respectively. This linear scaling relationship is consistent with approaches based on leaf-scale relative uptake and process models (Hilton et al., 2017).

Soil uptake: Soil uptake was implemented using zero-order soil fluxes from SiB4, yielding a global total of 177 Gg S yr^{-1}.

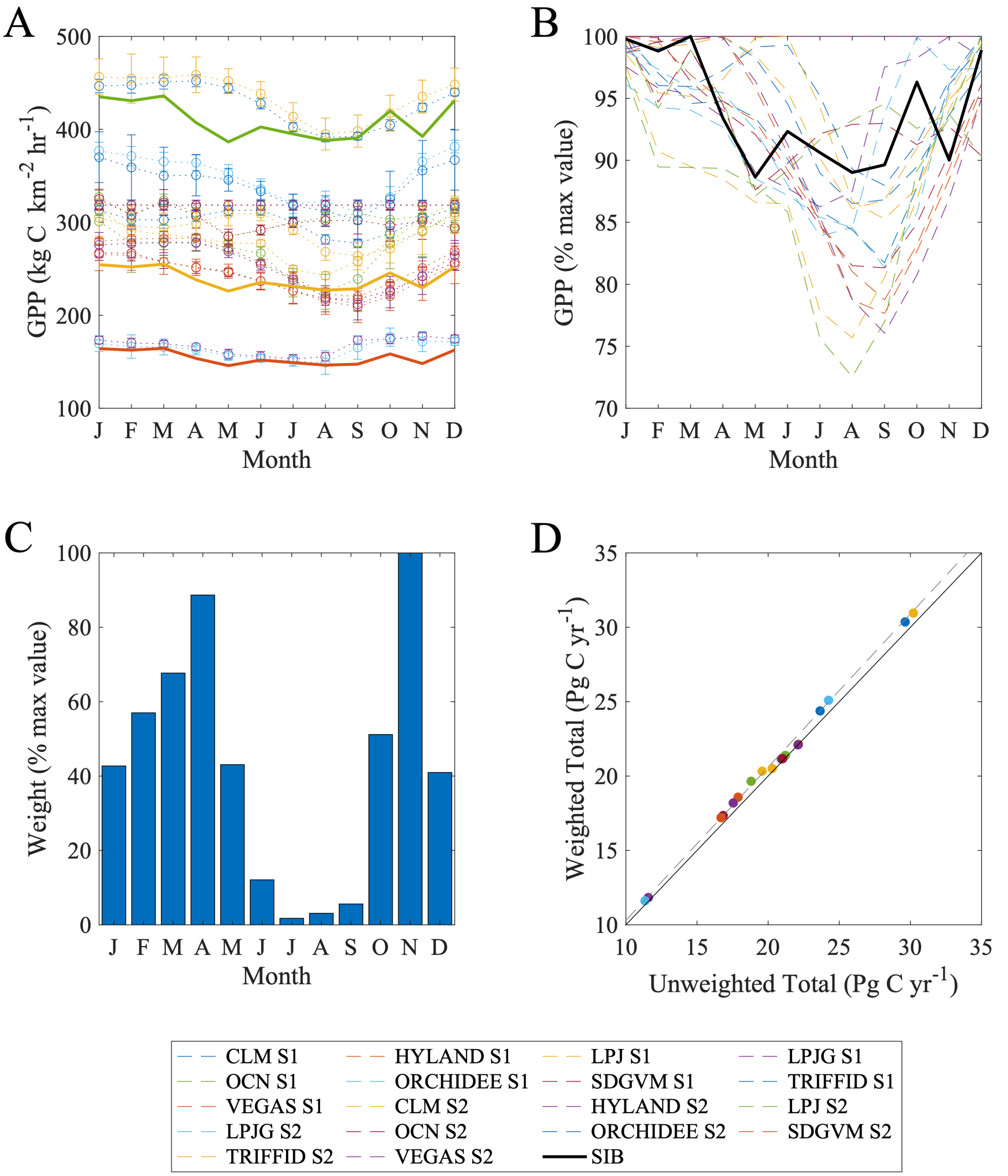

Figure 3-6: Impact of weighting on final estimated totals for the Amazon region. Panel A shows the GPP values from TRENDY (dotted) and the SiB-based values used for the model runs (solid). Error bars are 95% confidence intervals based on mean values for the last decade of simulation. Panel B shows the seasonal variation across these models, normalizing each model against its maximum value. Panel C plots the relative weights for each month as determined from the monthly error estimates (see Figure 3-4). Panel D plots the unweighted and weighted totals of TRENDY models, using the weights in Panel C. The 1-1 line indicates that the weighting typically results in an overestimation of annual GPP of 0-6%. A 3% overestimation is shown with the dotted line for comparison.

Ocean Emissions: We include direct (OCS) and indirect (DMS and CS_2) ocean sources from Kettle et al. (2002), totaling 39, 156 and 81 Gg S yr^{-1}, respectively. A supplemental ocean source optimized using data from TES observations of OCS was added to balance the flux budget (Kuai et al., 2015), following literature (Berry et al., 2013; Launois, Belviso, et al., 2015) suggesting that the ocean source was significantly larger than reported in Kettle et al. (2002). The supplemental source ranges from 239 Gg S yr^{-1} for the low-GPP model to 373 Gg S yr^{-1} for the high-GPP model.

Lennartz et al. (2017, 2019) show that, while oceanic emissions are larger than Kettle et al. (2002), the emissions are not necessarily large enough to fully account for the existing gap in the OCS budget. We note that a smaller OCS plant sink, as found here, further reduces the need for a large ocean source.

Anthropogenic Emissions:
Anthropogenic fluxes were based on a recent inventory by Zumkehr et al. (2017, 2018), averaging 363 Gg S yr^{-1} between 2004 and 2012. Compared to sources in Kettle et al. (2002), which yield 62 Gg S yr^{-1} for direct emissions of OCS and 122 Gg S yr^{-1} for indirect emissions, these fluxes are larger and primarily influenced by industrial sources in Asia. These latest fluxes, however, show little change in the Amazon region. As with changes to the ocean, changes to this flux primarily act as boundary conditions, accounted for in the background region.

Biomass Burning Emissions: OCS emissions due to biomass burning are based on an average of fluxes from Stinecipher et al. (2019) yielding 55 Gg S yr^{-1} between 2004 and 2012. This total is lower than the average of 116 Gg S yr^{-1} given in Campbell et al. (2015), but accounts more specifically for emissions between different biomes.

OH Chemical Sink: A hydroxyl radical sink is implemented in the model as described in Kuai et al. (2015), yielding a sink of approximately 106 Gg S yr^{-1}.

Annual fluxes are shown in Table 3-1 and Figure 3-7.

Atmospheric Transport and Chemistry Modeling

The above fluxes were used to drive multiple GEOS-Chem runs at 2° x 2.5° latitude-longitude resolution at 3-hourly time steps for 2004 to 2012 (the years for which both GEOS5 meteorology and MIPAS observations were available). Each setup was spun up from a constant initial condition file for four years with repeated meteorology and fluxes, prior to running the full simulation period.

Due to differences in sampling years and model data availability, we repeat surface fluxes annually and limit our analysis to a climatological time scale. However, for all TRENDY models, annual estimates of GPP from the last decade of simulations vary by less than 1.1% of the total GPP (standard deviation/mean) in the region of interest, mitigating concerns about interannual variability for the purposes of this study.

Table 3-1: Global flux totals as implemented in the GEOS-Chem simulations.

Flux Category	**Low GPP Model**	**Medium GPP Model**	**High GPP Model**
Ocean (Direct OCS)	40	40	40
Ocean (Indirect from DMS)	155	155	155
Ocean (Indirect from CS_2)	83	83	83
Ocean (Supplemental Flux)	*239*	*277*	*373*
Anthropogenic Source	363	363	363
Biomass Burning Source	56	56	56
OH Chemical Sink	-106	-106	-106
Soil Uptake	-177	-177	-177
Plant Uptake	-691	-691	-691
Amazon Plant Uptake Adjustment	*37*	*0*	*-96*
Net Flux	**0**	**0**	**0**

Italicized rows highlight changes between models. All fluxes are in terms of Gg S yr^{-1}, where positive fluxes signify a source of OCS into the atmosphere. See Figure 3-7 for more information on the spatial distribution of fluxes.

3.7.2 Point Sampling Approach

Observations from MIPAS (Glatthor et al., 2015, 2017) were used as comparison products for the GEOS-Chem simulations. MIPAS data were quality-filtered per data use guidelines and interpolated to 250 hPa as in Glatthor et al. (2015). 250 hPa was selected because it was the lowest altitude with near-complete global coverage when data are binned (e.g., Figure 3-2). We note that additional OCS total column abundance data measured by the nadir-sounding Tropospheric Emission Spectrometer (TES) onboard the Aura satellite is available, but for a smaller period of time and only over oceans (Kuai et al., 2014, 2015).

GEOS-Chem models the atmosphere through an Eulerian (rather than Lagrangian) framework (Henze et al., 2007). In this case, the model solves the continuity equation to determine mixing ratios in each grid cell, as opposed to tracing specific parcels of air. While this allows for efficient computation of global mixing ratios, it complicates the task of identifying a parcel's origin (Henze et al., 2007; Reynolds et al., 1973). However, by perturbing a region in the model (in this case, the Amazon basin) and comparing the concentration fields downwind, we can effectively determine the atmospheric region influenced by certain surface fluxes.

This task is similar to calculating a Jacobian in that we are interested in determining the sensitivity of concentrations in grid cells (the observation vector) to perturbations of surface fluxes (the state vector). Such an approach is often computationally prohibitive when many regions or fluxes are being changed, as many forward model runs are required (Henze et al., 2007; Rigby et al., 2011). However, by limiting the focus of this work to one region, we mitigate these challenges.

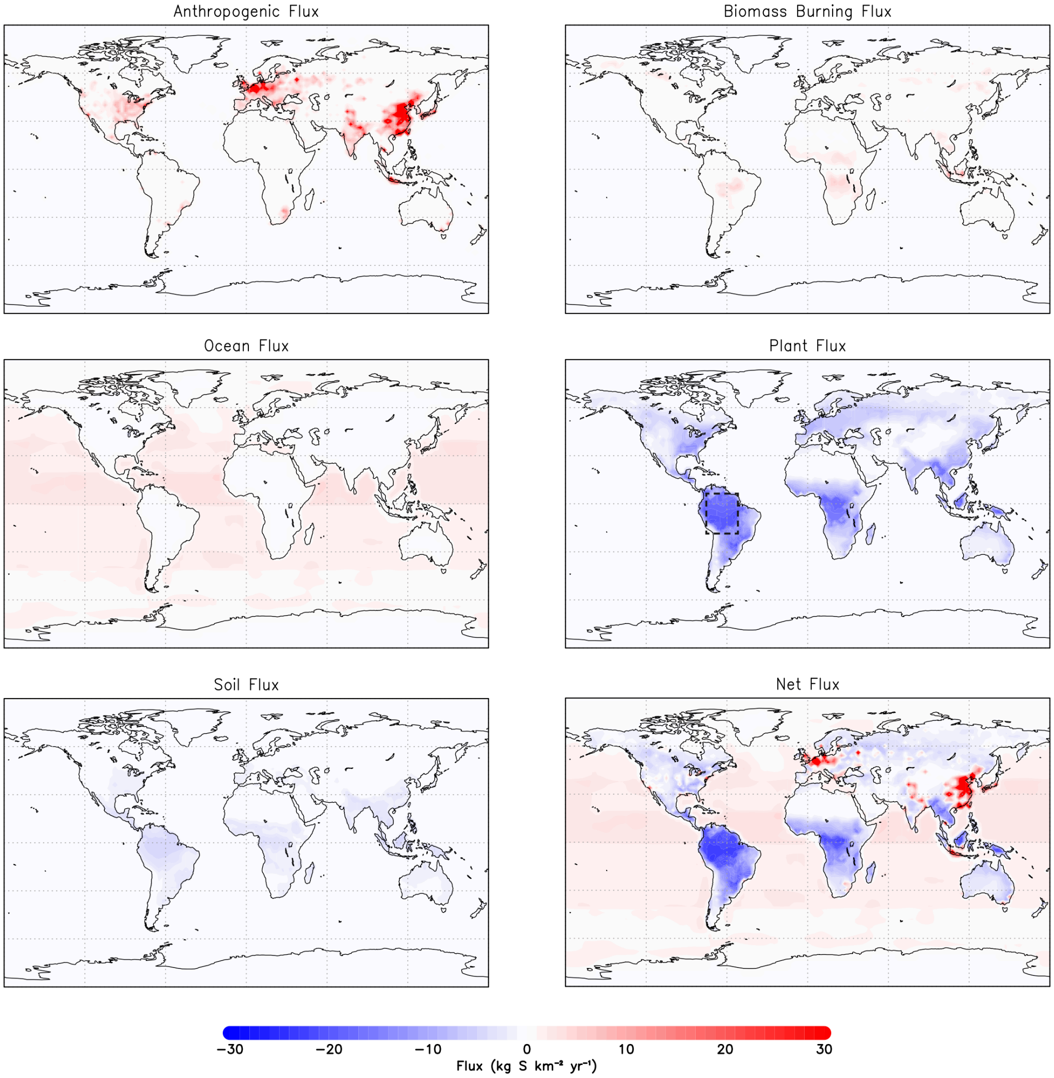

Figure 3-7: Annual OCS fluxes (kg S km^{-2} yr^{-1}) from different components of baseline (medium) budget. The dashed box on the Plant Flux panel denotes the region perturbed between simulations.

For each satellite observation and its associated model estimates, a sensitivity ratio R_{sens} is defined as the low-GPP model concentration divided by the high-GPP model concentration. In regions that are strongly influenced by changes to surface fluxes in the Amazon, the low-GPP model will yield less OCS uptake and higher concentrations, leading to sensitivity ratios greater than 1. Collections of points where R_{sens} is greater than 1 therefore represent upper-troposphere regions sensitive to the region of interest at the surface. Conversely, regions of points where R_{sens} is less than or approximately equal to 1 represent background regions that are relatively unchanged between simulations.

We demonstrate the approach by comparing an inner region with $R_{sens} \geq 1.035$, to an outer region with sensitivity values $1.005 \leq R_{sens} \leq 1.01$, truncated to values between ± 30° latitude. The latter region serves as a background or inflow value against which the former value can be standardized between datasets. Figure 3-8 shows the point clouds for January observations. This spatial pattern is consistent with westerly winds of the Atlantic Walker cell in the upper troposphere.

To reduce bias from an arbitrary choice of thresholds, we test an ensemble of 576 combinations (12 inner thresholds x 12 outer thresholds x 4 outer latitude bounds in order to focus only on the tropics). The list of thresholds is given in Table 3-2.

For illustrative purposes, we plot histograms of concentrations for these regions in Figure 3-9 for both January and July. Note that in January, the histogram for the observations shows far less variance and tends to yield values consistent with the low-GPP model, while in July, the histogram spans the entire range of model scenarios.

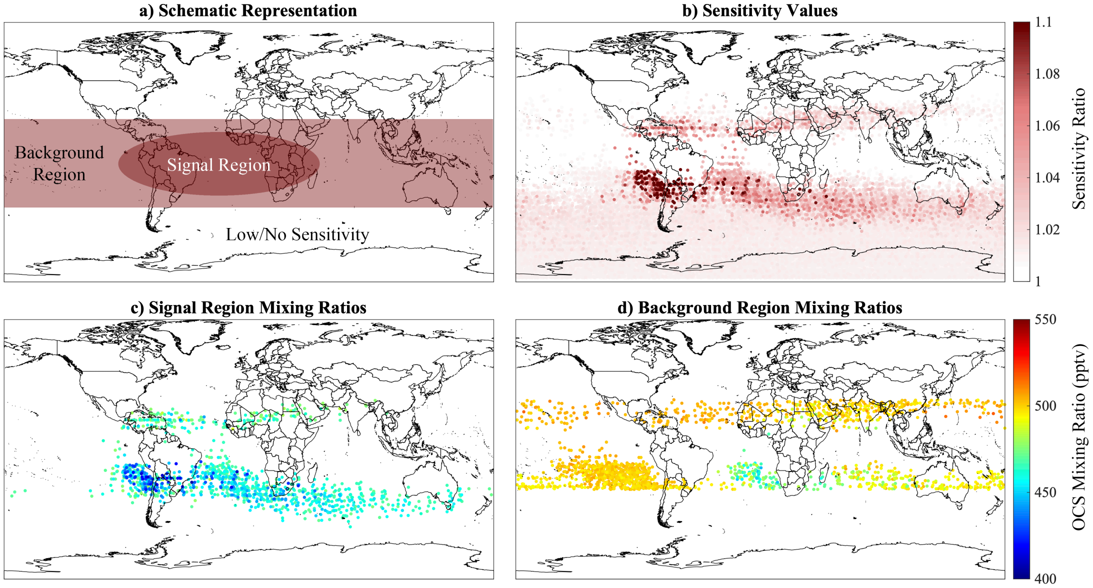

Figure 3-8: (A) Schematic of signal / background regions. (B) All measurement locations, with colors corresponding to sensitivity ratio calculated by model output. (C-D) Demonstration point distribution for one pair of signal (C) and background (D) regions for all January observations, with colors corresponding to medium-GPP model concentrations at 250 hPa.

Table 3-2: Thresholds for sensitivity levels, as well as constraints on latitudinal variation.

Inner/Signal Region Sensitivity Thresholds	Outer/Background Region Sensitivity Thresholds	Outer/Background Region Latitude Bounds
$R_{sens} \geq 1.03$	$0 \leq R_{sens} \leq 1$	30°N to 30°S
$R_{sens} \geq 1.0325$	$0 \leq R_{sens} \leq 1.0025$	35°N to 35°S
$R_{sens} \geq 1.035$	$0 \leq R_{sens} \leq 1.005$	40°N to 40°S
$R_{sens} \geq 1.0375$	$0 \leq R_{sens} \leq 1.0075$	45°N to 45°S
$R_{sens} \geq 1.04$	$0 \leq R_{sens} \leq 1.01$	
$R_{sens} \geq 1.0425$	$0 \leq R_{sens} \leq 1.0125$	
$R_{sens} \geq 1.045$	$0 \leq R_{sens} \leq 1.015$	
$R_{sens} \geq 1.0475$	$1 \leq R_{sens} \leq 1.005$	
$R_{sens} \geq 1.05$	$1.0025 \leq R_{sens} \leq 1.0075$	
$R_{sens} \geq 1.0525$	$1.005 \leq R_{sens} \leq 1.01$	
$R_{sens} \geq 1.055$	$1.0075 \leq R_{sens} \leq 1.0125$	
$R_{sens} \geq 1.0575$	$1.01 \leq R_{sens} \leq 1.015$	

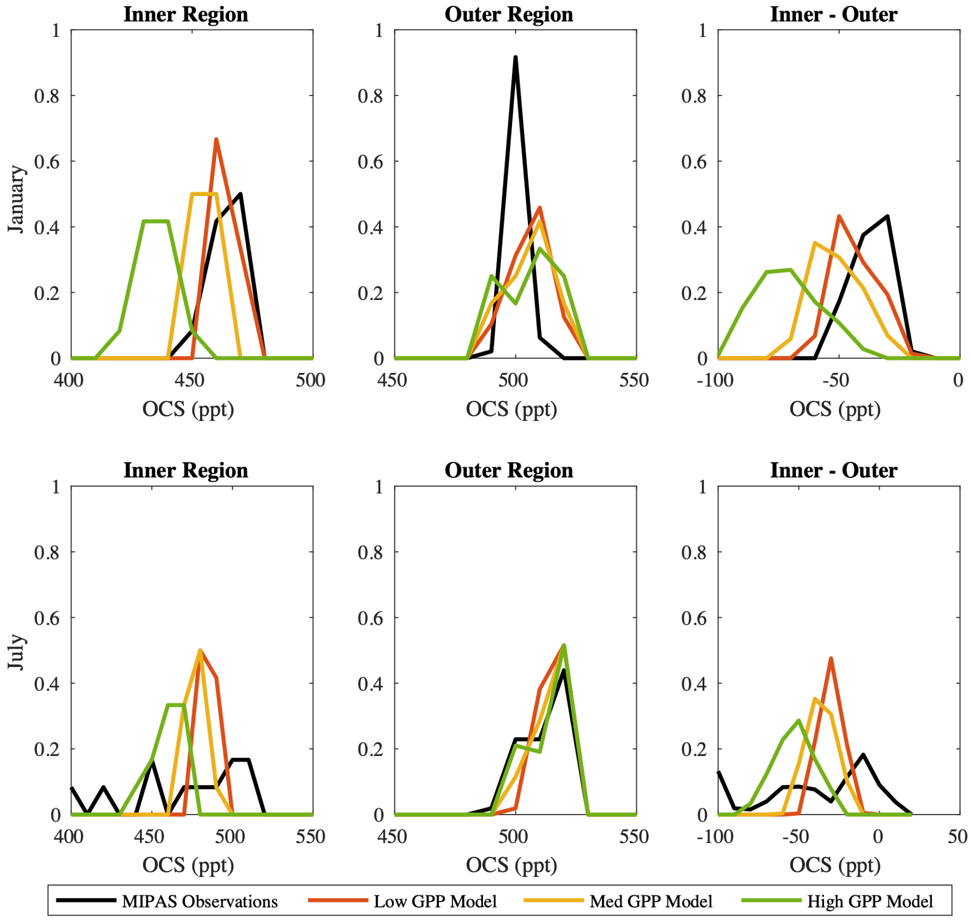

Figure 3-9: Histograms for average inner (signal), outer (background), and difference (inner-outer) concentrations across all threshold combinations. In January (top row), MIPAS values are most similar to the low model. In July (bottom row), observations span all three models and cannot be constrained.

3.7.3 Error Analysis

We divide the error analysis into two components: those sources of uncertainty due to the point-sampling method itself and post-analysis sources of uncertainty which are more systemic in nature.

Analysis Sources of Error

Measurement variation within each choice of threshold
For every month, we extract and aggregate observations as described in Section 3.7.2. Each choice of threshold yields an associated standard error of the mean, which depends both on the number of observations which meet the threshold and the variation in those observations.

Each month, we calculate the standard error of the mean (SEM) for the signal and background regions for each threshold combination and add the components in quadrature. We then average the combined SEM values across all threshold combinations.

The SEM for the signal region dominates relative to the background due to the much smaller number of observations. We note that more extensive sampling would drive this error term lower (optimally to zero), as more samples would better approach the true mean concentration for a given region.

Variation in estimated fluxes across threshold combinations
Since each choice of threshold yields a different estimate for GPP, we repeat the analysis with a range of threshold values to minimize selection bias (see Section 3.7.2). To account for the variation in the resulting estimated fluxes, we compute the standard deviation of surface flux estimates across all threshold setups.

Total sources of error due to point-sampling method
We add the above terms in quadrature for each month (see Figure 3-4 in the main text). In computing the annual total, we compute a weighted average based on the square inverse of this combined uncertainty.

The resulting uncertainty for the weighted average is computed by an unbiased weighted sample variance

$$s^2 = \frac{\sum_{t=1}^{12} w_t (x_t - \mu^*)^2}{\sum_{t=1}^{12} w_t - \left(\frac{\sum_{t=1}^{12} {w_t}^2}{\sum_{t=1}^{12} w_t}\right)}$$

where t is the month, w_t and x_t are the corresponding weights and monthly flux estimates respectively, and μ^* is the overall weighted average.

Using these sources of error, we obtain an initial estimate of 8.6 ± 3.4 Pg C yr^{-1} for the region of interest.

Systemic / Post-Analysis Sources of Error

Relationship between OCS uptake and GPP

A variety of factors influence the amount of OCS taken up by plants relative to GPP. A useful parameter for assessing the relationship between OCS uptake and GPP is the leaf-scale relative uptake (LRU), which relates the efficiencies with which plants take up OCS and CO_2. These parameters are related through the following expression:

$$F_{OCS} = GPP \times LRU \times [OCS]/[CO_2]$$

where F_{OCS} and GPP are the fluxes of OCS and CO_2 into the plant, respectively, LRU is the leaf-scale relative uptake, and the final term is the ratio of ambient concentrations of OCS and CO_2 (Hilton et al., 2017).

Over the region of interest, the medium flux is 127.52 Gg S OCS vs. 16.63 Pg C GPP annually, computed directly from flux files or, in different units, 18.6 pmol OCS m^{-2} s^{-1} vs. 5.54 μmol CO_2 m^{-2} s^{-1}. Given these values and assuming an ambient ratio of 1.1 ppt OCS / ppm CO_2 as in Hilton et al. (2017), we obtain an LRU of 2.6.

Sandoval-Soto et al. (2005) report tropical forest LRU values ranging from 1.7 to 3.6. Given this range, we estimate a standard deviation of 0.475 and thus a relative uncertainty of 18% compared to the computed LRU. Applying this error to the retrieved GPP yields an uncertainty of 1.56 Pg C yr^{-1}.

Choice of Transport Model

In order to determine the effect of transport model choice on the analysis, we ran GEOS-Chem and PCTM with identical surface fluxes. Due to model limitations, the atmospheric OH sink was excluded from the PCTM model run. For both runs, we extract and aggregate model concentrations as described above. We compare the root mean square error (RMSE) from estimated depressions over all regions in the ensemble for two years of model output. The average RMSE was 2.4 pptv OCS between models across all threshold setups.

For comparison, the average difference between the GEOS-Chem model depressions is 25.9 pptv OCS (ranging from 22.7 in August to 29.1 in February). When compared to the overall range between the low and high model GPP (18.9 Pg C / yr), we obtain an uncertainty of 1.8 Pg C yr^{-1} (approximately 9.3%).

Bias due to seasonality and weighting

The weighted average computed in the text results in undersampling the period of time when TRENDY models predict a decrease in GPP (see Figure 3-6, panels B and C). To account for this, we apply the same weights to the TRENDY values, then compare the uncertainty-weighted and unweighted (evenly weighted) annual totals.

The weighted GPP values are 0% to 6% higher than the unweighted totals, suggesting a possible overestimation of GPP in our result by a similar magnitude. We reduce the initial estimate of the mean by 3% and add 3% to the overall error.

Uncertainty in Non-Plant Fluxes

Although we have sought to use the best available estimates for each type of surface flux, uncertainties remain in each category. To assess this variation, we extract the following ranges in flux estimates from literature, summed over the Amazon region.

Estimates of soil fluxes in the region of interest range from -5 to -28 Gg S yr^{-1} (Kettle et al., 2002 versus mechanistic estimates from SiB), estimates of anthropogenic emissions range from 0.2 to 1.3 Gg S yr^{-1} (Zumkehr et al., 2017 versus Kettle et al., 2002), and estimates of biomass burning range from 6 to 22 Gg S yr^{-1} (Stinecipher et al., 2019 versus the upper end of scaling factors from Campbell et al., 2017). In comparison, regional plant fluxes between the low- and high-GPP scenarios range from -90 to -224 Gg S yr^{-1}. We estimate the standard deviation of the total range in non-plant fluxes as 10 Gg S yr^{-1} which, when compared to the range in plant fluxes, yields a corresponding GPP uncertainty of 1.4 Pg C yr^{-1} (approximately 7%).

Representation Error in Flux Distribution

We conducted an additional set of runs using lower anthropogenic fluxes from Kettle et al. (2002) and larger biomass burning fluxes based on scaling factors from Campbell et al. (2017). Supplemental ocean fluxes were increased by 118 Gg S yr^{-1} to account for the resulting deficit in emissions. Results from this experiment are shown in Figure 3-10 (compare with the results in Figure 3-4).

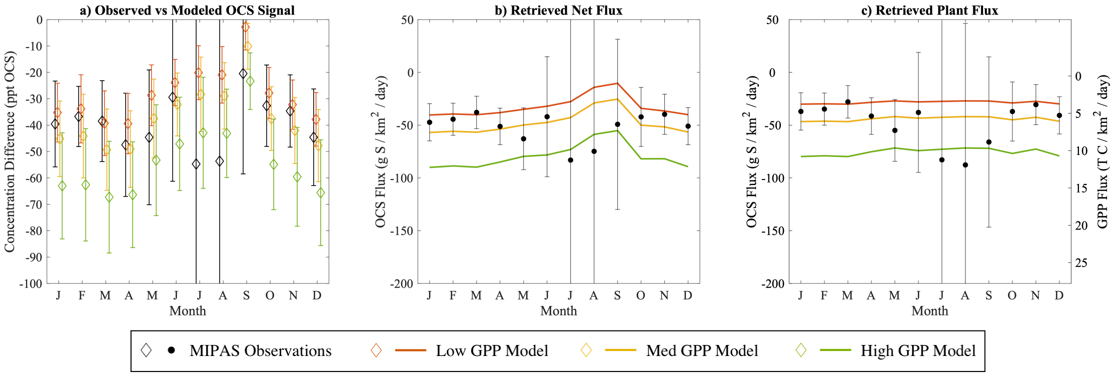

Figure 3-10: Results from an additional set of model runs using different fluxes also suggest lower-GPP models are most consistent with observed OCS concentrations. See Figure 3-4 for additional details.

As before, retrievals are highly uncertain between June and September, while months with less uncertainty tend to correspond best with the low-GPP model. In this case, the total retrieved plant flux in the region was -106.3 Gg S yr^{-1}, in contrast to the -70.7 Gg S yr^{-1} calculated above. Comparing this range against the range in plant fluxes, we estimate an uncertainty of 8.9 Gg S yr^{-1}, corresponding to 1.3 Pg C yr^{-1}.

Total Uncertainty

The final estimate combines all categories of errors in quadrature, yielding an overall estimate of 8.3 ± 4.6 Pg C yr^{-1} (mean ± sd), or 1051 ± 581 g C m^{-2} yr^{-1}.

3.7.4 Vertical Profile Estimates

While the primary focus of the present work is the use of upper-troposphere MIPAS observations, additional trends are evident in the vertical structure of model results. Figure 3-11 shows the modeled vertical profile over the perturbed Amazon region.

Near the surface, the effect of modifying plant fluxes is highly visible; in both the wet and dry season, concentrations are nearly 100 ppt lower in the high-GPP model. In the upper troposphere, however, results are more seasonal. While the high-GPP model continues to yield lower OCS concentrations at 250 hPa, during the period of low convection (June to August), the high-GPP model shows only a slight depletion in OCS. Future studies collecting observations closer to the surface could better differentiate between models during this period.

While MIPAS observations at 250 hPa over this region were still most similar to the low-GPP model, the use of fixed averaging regions proved to be overly sensitive to the manner in which regions were defined. Leveraging sensitivity ratios as described in the main text allows for the capture of additional, informative parcels which may have been transported outside the column. Similarly, the approach places less weight on background parcels which may have been transported *into* the column.

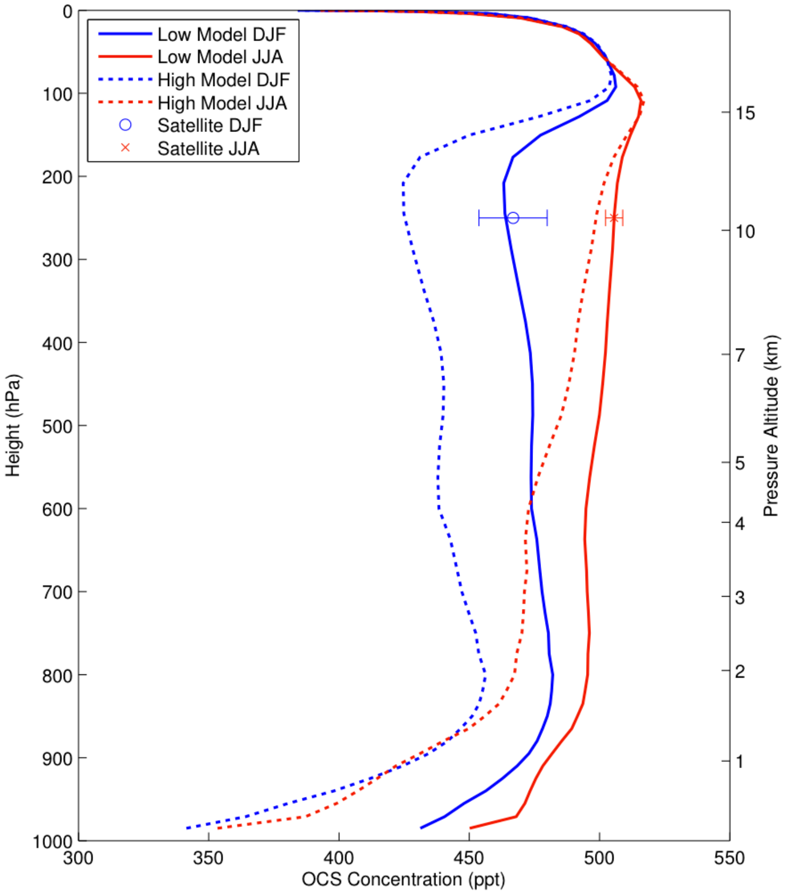

Figure 3-11: Modeled vertical profiles of OCS for simulations with low- and high-uptake plant fluxes. Changes in model surface fluxes propagate to the tropopause (~ 250 hPa), with the largest differences visible during wet season months. Modeled data from GEOS-Chem are evenly weighted across the region at each vertical level. MIPAS observations are the mean of all samples within the region interpolated to 250 hPa, with 95% confidence intervals on the mean (μ ± 1.96 * s.e.). Pressure altitudes are calculated by interpolating values from the US Standard Atmosphere, 1976. (Table 1 - https://ntrs.nasa.gov/archive/nasa/casi.ntrs.nasa.gov/19770009539.pdf).

Chapter 4: Observing System Simulation Experiments Underscore Need for Additional OCS Sampling

4.1 Abstract

Observing system simulation experiments (OSSEs) are a common approach to analyzing design aspects of future experiments. Particularly in remote-sensing contexts where cost constraints leave little room for error, OSSEs provide information about the feasibility of an experiment or instrument, while also assessing the relative benefits that changes to the design could have on the overall retrieval. Here, we consider a number of modifications which could be made to the MIPAS approach from the previous chapter. Increased sample density (especially in the tropics), lower sample altitudes and reductions in instrument noise all yield improvements to the retrieval, though often only to a point. In addition to considering satellite observations, we briefly assess some considerations for future studies with aircraft in the Amazon basin.

4.2 Introduction

Chapter 3 shows the value and limitations in using remotely sensed carbonyl sulfide to constrain gross primary production. While the data are sufficient to make broad estimates of photosynthetic uptake, changes to future sampling campaigns could lead to improved estimates. Among other aspects, changes to spatial and temporal resolution, sampling altitude, and instrument accuracy could each provide unique value in reducing the overall retrieval uncertainty (see e.g., Aghedo et al., 2011).

Upper-troposphere retrievals contain limited information during the dry season, due primarily to a lack of deep convection. In the absence of this vertical transport, only a few parcels with sufficient information content from the surface reach the upper troposphere.

More broadly, sampling the tropics (and the Amazon specifically) remains a challenge and leads to uncertainties year-round. Cloud contamination is a major issue, resulting in far fewer observations in the tropics than in temperate regions. Although Chapter 3 mitigates this issue through “downstream” sampling, additional observations closer to the area of interest could lead to improved estimates.

Beyond the lack of sampling, instrument noise remains a source of error. The minute concentrations of ambient carbonyl sulfide make it challenging to sample *in situ*, let alone by remote sensing. As such, there is room for improvements to the instrument or the overall retrieval algorithm. A reduction in instrument noise could effectively reduce the need for more sampling.

To this end, we incorporate these challenges into an observing system simulation experiment (OSSE), in order to assess the relative impact of various changes that could be made in future studies. OSSE studies have been used extensively (particularly in the remote sensing community) to address the merits and feasibility of future missions with minimal cost (Chen et al., 2011; Errico et al., 2013; Masutani et al., 2010; Privé et al., 2013; Timmermans et al., 2015).

In general, an OSSE is conducted by sampling known data (the “nature run”), adding appropriate instrument noise, and then using the retrieval approach in question to attempt to reconstruct the underlying variables of interest (Timmermans et al., 2015). In this case, we use the existing low-GPP model run from the previous chapter as truth, and, after sampling the model output and adding noise, we attempt to retrieve the low model fluxes.

Finally, although satellite data provide broad, long-term coverage, future campaigns leveraging aircraft data could provide additional value at smaller spatial and temporal scales. While an in-depth study of the value of aircraft measurements is beyond the scope of the present paper, initial results highlight the value and some necessary considerations of future airborne sampling campaigns. For this work, we limit our analysis to patterns of surface sensitivity at different altitudes over the course of the year.

4.3 Methods

Nature Run and Synthetic Observations

As mentioned, we use the low-GPP model as truth. Because the underlying fluxes of this model are known exactly, we can assess how differences in sampling and noise propagate to the retrieved signal. Ideally, the model used to create the nature run should be distinct from the model used for the inversion, but this is beyond the scope of the current study. We run the model from 2004 to 2012, the time period overlapping both the available MIPAS observations and the available model meteorology.

Sampling Locations

In order to capture the wide variety of possible improvements described above, we employ a number of different sampling scenarios.

To investigate the effect of sampling density in general, without considering the role of cloud contamination, we conduct a set of three tests with fully random sampling locations. We denote these scenarios as A-15, A-30, and A-45, where the number corresponds to the number of observations in a given 3-hour model timestep. A-45 is most similar to the number of observations taken by MIPAS, though in practice these are not evenly distributed.

The MIPAS sampling pattern forms the basis for the next set of experiments. We denote these sampling locations as scenario B. Note that, in general, very few observations are available in the tropics, although samples outside of this region are still sensitive to the Amazon surface fluxes.

Using a region defined by Glatthor et al. (2015), we consider the effect of additional sampling in the tropical Atlantic. We denote two scenarios as C-1 and C-5, where the value corresponds to the number of additional random samples per 3-hour model timestep in a box extending from 20°S to 10°N and from 75°W to 25°E. This box was selected to capture the large depletion of OCS observed by MIPAS in the upper troposphere resulting from the convective outflow of parcels sensitive to photosynthetic uptake in the tropics. Although Glatthor et al. (2015) do not attribute this depletion solely to uptake in the Amazon, results from the previous chapter show that the region contains significant information content about surface fluxes in the Amazon basin.

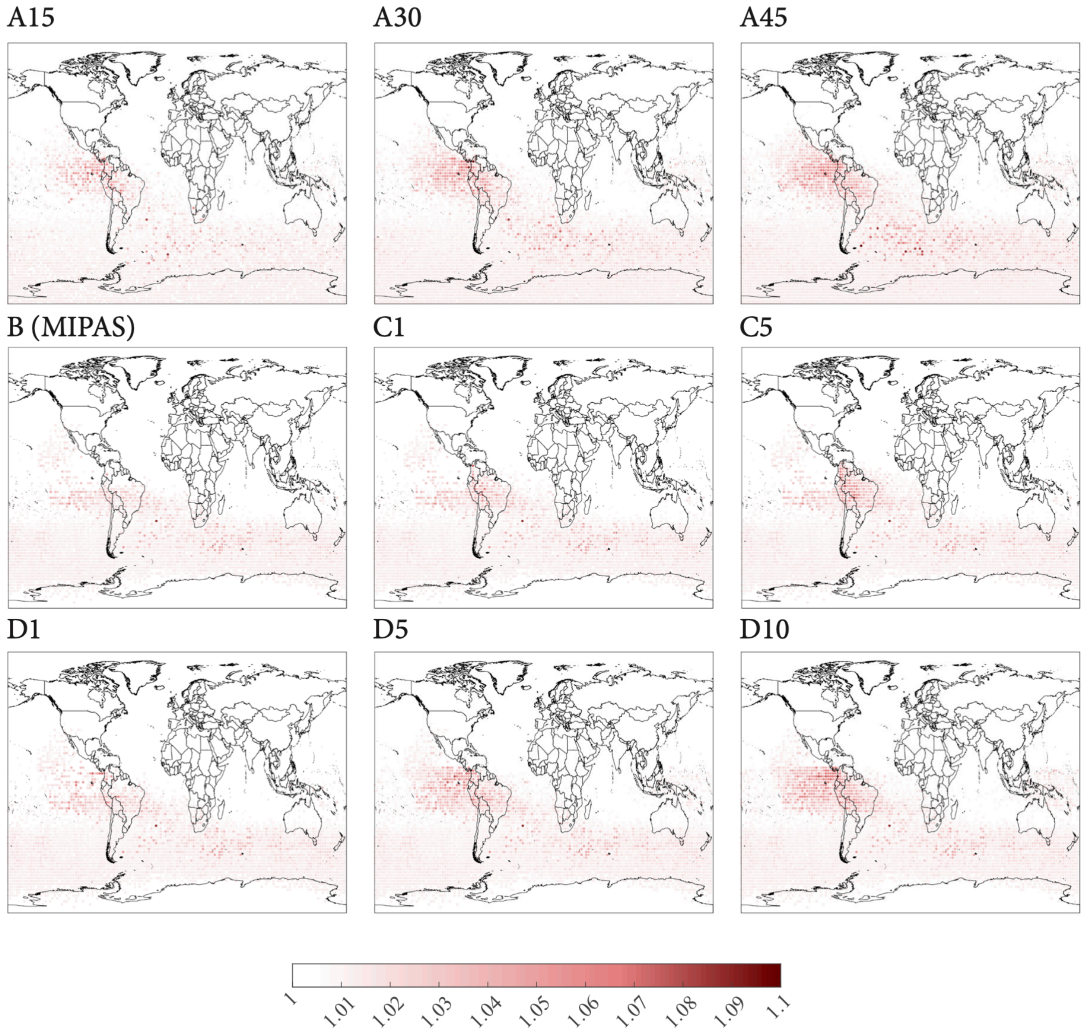

Figure 4-1: Comparison of different sampling scenarios in July. Colors represent the sensitivity of the model concentrations at 250 hPa to changes in surface fluxes in the Amazon, defined as the low-GPP model concentration divided by the high-GPP model concentration.

In contrast to the Atlantic-based C scenarios, we also consider the effect of randomly sampling the entire tropical band defined in Glatthor et al. (2015). We conduct three scenarios, D-1, D-5 and D-10, with additional observations randomly sampled between 20°S and 10°N. As before, these scenarios include 1, 5, or 10 additional observations per 3-hour model timestep, respectively.

Instrument Error Estimation

To obtain a realistic estimate of the measurement noise in the MIPAS observations, it is necessary to account for differences in spatial and temporal distribution, as well as any bias in the global mean.

An initial estimate for instrument is derived by first gridding points into boxes 5° by 15° in size, following Glatthor et al. (2015). In this case, we compute the standard deviation of points in each grid cell, then average these across the entire globe for each month. The standard deviation obtained using this approach is 63.5 ppt.

To reduce the impact of gridding on the overall estimate, a more precise approach is to consider each observation separately, while still accounting for spatial and temporal differences. We compute the following standard deviation for each month:

$$\sigma_{ins} = \sigma\big((\mathrm{OCS_{obs}} - \overline{\mathrm{OCS_{obs}}}) - (\mathrm{OCS_{low}} - \overline{\mathrm{OCS_{low}}})\big)$$

where $\overline{\mathrm{OCS_{obs}}}$ and $\overline{\mathrm{OCS_{low}}}$ are the global mean mixing ratios for the MIPAS observations and low-GPP model values, respectively.

By comparing to the low model (shown in Chapter 3 to more closely approximate the correct fluxes than other model runs), we reduce the effect that the spatial distribution has on the error. Removing the respective mean values mitigates any bias between the modeled and observed concentrations. The computed standard deviations for each month vary from 58 to 64 ppt OCS, with a mean value of 60.8. We use a normally distributed random variable with mean 0 and the mean standard deviation in place of measurement noise.

In addition to the noise level calculated for the MIPAS observations (60.8), we conduct an additional series of tests using noise at various thresholds (0, 15, 30, 45, 75 and 90 ppt).

Flux Retrieval from Pseudodata

For each set of sampling scenarios and noise levels, we sample the model output over the entire simulation period as in the previous chapter. We add noise to the sampled values and use these as inputs in the retrieval. A sample retrieval is shown in Figure 4-2; in this case, we are attempting to retrieve the low-GPP model values when sampled at the same locations as MIPAS (Scenario B) with added noise.

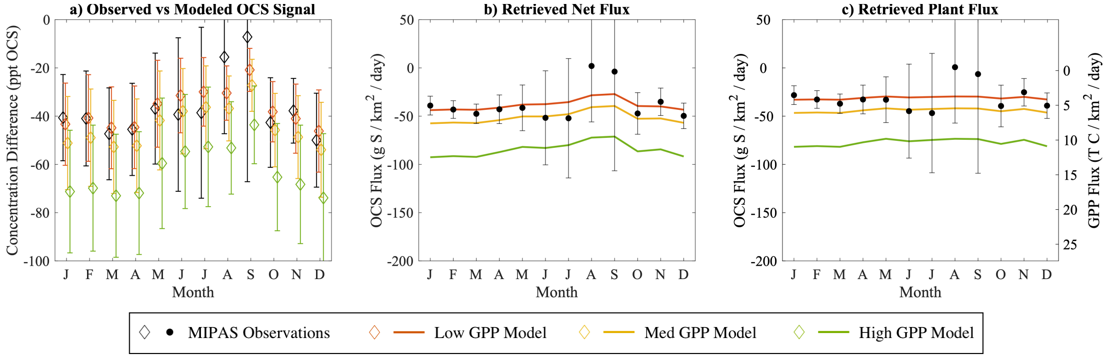

Figure 4-2: One iteration of retrieval using pseudodata from MIPAS sampling locations. The retrieved values (black) are prescribed to most closely approximate the low-GPP model (red). Error bars are 95% confidence intervals as described in Chapter 3.

Particularly in months with low convection, few observations at altitude are sensitive to changes at the surface. As a result, a few observations with significant amounts of noise can unduly influence the overall average value. Although this is difficult to account for in a field setting, we run 10 replications for each scenario, then take the mean and standard deviation in order to determine the effect of different random number seeds on our experiments.

After each retrieval is completed, we analyze the performance through several root mean square error calculations. We compute the RMSE for the concentration and for the plant flux, comparing the values between the known model and the pseudodata retrieval over the full year. Because uncertainties can vary throughout the year, we compute both an unweighted RMSE and a weighted value using the inverse of the uncertainty. Differences between these two values show the impact that poorly computed months have on the overall value.

We compute these errors for each simulation, then average the values over all replications. These average errors are used as the comparison metric between scenarios (Figure 4-3).

Aircraft/Profile Analysis

Gatti et al. (2014) used aircraft profiles in order to compare changes in CO and CO_2 across the Amazon basin. Following this work, we sample the model outputs from the previous chapter at six sites used for *in situ* measurement campaigns. Four sites (RBA, TAB, SAN, and ALF) are within the Amazon basin, while two others (RPB and ASC) serve as background sites for air parcels entering from the Atlantic. At the nearest grid cell for each site, we extract vertical profiles from one year of model results to determine spatial and temporal changes in sensitivity values.

Table 4-1: Site locations of aircraft profiles in Gatti et al. (2014)

Code	Name	Lat	Lon
RBA	Rio Branco	-9.97	-67.81
TAB	Tabatinga	-4.25	-69.94
SAN	Santarém	-2.43	-54.72
ALF	Alta Floresta	-9.89	-56.09
RPB	Royal Point Barbados	13.16	-59.43
ASC	Ascension Island	-7.93	-14.37

4.4 Results

In comparing the different scenarios, we compute the root mean square error across the retrieved concentration and fluxes, both as an unweighted mean over the course of the year and weighted by the inverse of the retrieval error (Table 4-2 and Figure 4-3). For samples at 250 hPa, the error-weighted values are lower than the unweighted values, as these reduce the impact of the most uncertain (and typically least accurate) retrieval months on the overall RMSE. Samples at 500 hPa show little difference between the two averaging approaches.

Table 4-2: Root mean square errors in retrieved values vary due to changes in sampling scenario, synthetic instrument noise σ_{ins}, and sampling height (250 hPa and 500 hPa). The starred row (Scenario B with 60.8 ppt of added noise, sampled at 250 hPa) most closely matches the actual data observed by MIPAS and is therefore used as truth. Values are reported as mean ± sd, where the standard deviation is computed over 10 replications of each analysis.

Scenario	σ_{ins}	**250 hPa Unweighted**	**250 hPa Weighted**	**500 hPa Unweighted**	**500 hPa Weighted**
** B (MIPAS)*	*60.8*	*7.2 ± 12.9*	*5.5 ± 7.4*	*3.8 ± 6*	*3.9 ± 5.8*
A15	60.8	3.9 ± 6.7	3.8 ± 5.1	2.8 ± 4.1	2.8 ± 4
A30	60.8	3 ± 5.2	2.9 ± 3.6	2 ± 3	2.1 ± 2.8
A45	60.8	3 ± 5.1	3 ± 3.3	1.8 ± 2.6	1.8 ± 2.5
B (MIPAS)	15	1.9 ± 0.7	1.9 ± 0.6	0.9 ± 0.2	1 ± 0.4
B (MIPAS)	30	3.6 ± 0.7	3.2 ± 0.7	1.8 ± 0.2	1.9 ± 0.3
B (MIPAS)	45	4.5 ± 0.9	3.7 ± 0.5	2.6 ± 0.3	2.8 ± 0.4
B (MIPAS)	75	8.5 ± 1.9	6.9 ± 1.2	4.9 ± 0.7	5 ± 0.8
B (MIPAS)	90	10.6 ± 3.4	7.6 ± 1.9	6.1 ± 1.6	5.9 ± 1.5
C1	60.8	4.7 ± 8.3	4 ± 5	2.8 ± 4.2	2.9 ± 3.9
C5	60.8	3.3 ± 5.9	3.2 ± 3.6	1.8 ± 2.7	2 ± 2.4
D1	60.8	5.4 ± 9.6	4.5 ± 5.9	3 ± 4.6	3.1 ± 4.4
D5	60.8	3.2 ± 5.6	3 ± 3.7	2.2 ± 3.3	2.3 ± 3.1
D10	60.8	2.5 ± 4.4	2.4 ± 2.9	1.7 ± 2.6	1.9 ± 2.5

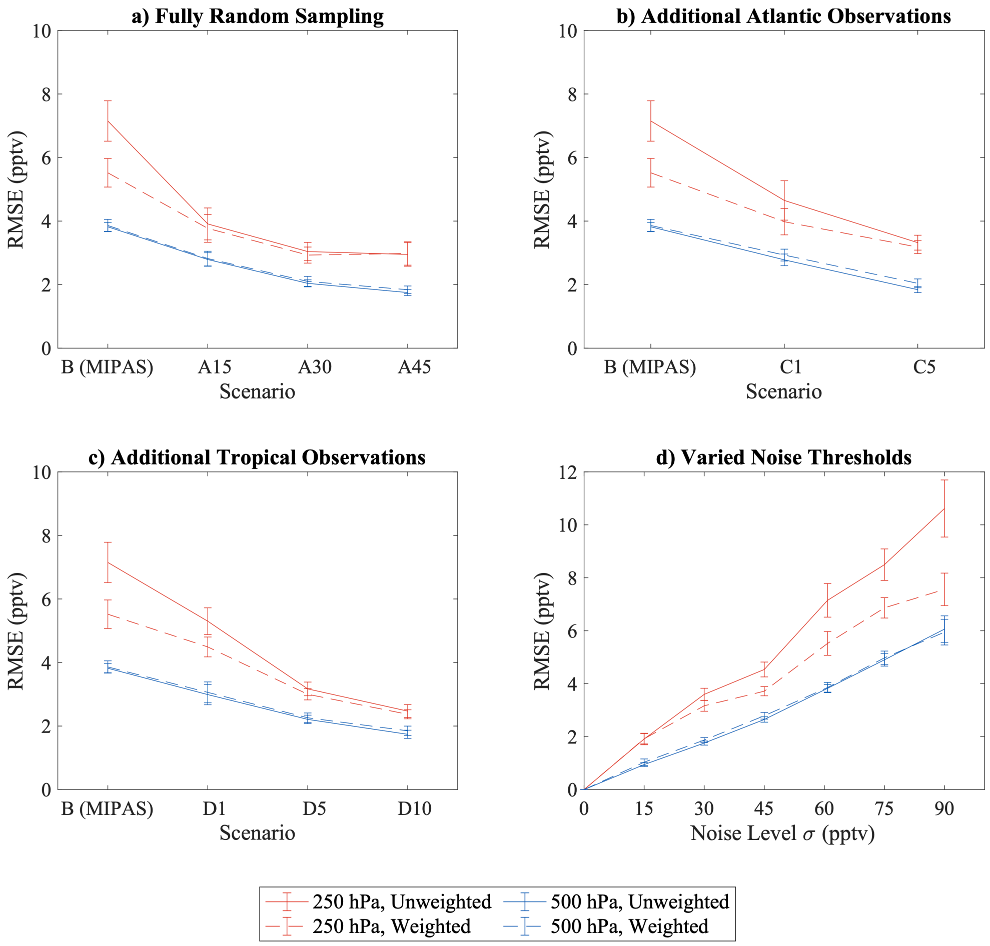

Figure 4-3: Increasing sample density (Panels A-C) and decreasing instrument noise (Panel D) yield improvements to overall retrieval errors. Samples at 500 hPa yield further improvements over samples at 250 hPa. Error bars are standard deviations across 10 replications of each analysis.

In all cases, retrievals using values extracted at 500 hPa (mid-troposphere) are more accurate than those at 250 hPa (upper troposphere). As the upper-troposphere measurements require significant convective transport, fewer sensitive parcels reach the necessary sampling altitude. As these parcels are subject to atmospheric mixing and instrument noise, the average within the signal region may be unduly influenced by a few noisy observations. In contrast, although the observations at 500 hPa are subjected to the same level of noise, more parcels sensitive to the Amazon region are elevated to the sampling height (Figure 4-4). As such, the averages for the same signal regions contain far more observations and provide a better estimate of the mean values. In July, for example, the signal regions at 250 hPa contain an average of only 27 observations, whereas more than 142 samples at 500 hPa meet the thresholds for inclusion.

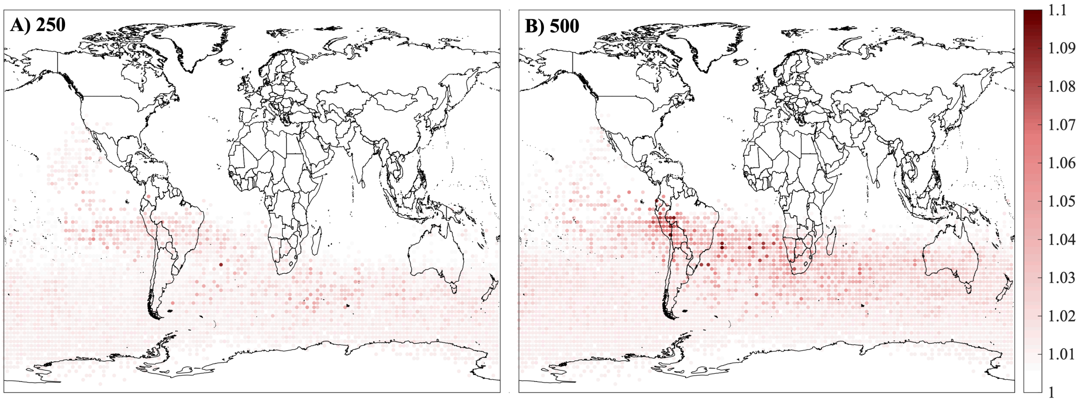

Figure 4-4: Sampling at MIPAS observation locations at both (A) 250 hPa and (B) 500 hPa during July, aggregated over all model years. Colors are the computed sensitivity ratios for each observation location.

In a similar manner, increases in sampling density yield lower errors (Figure 4-3, Panels A-C). In these cases, while the number of sensitive grid cells at a given level remains the same, the ability to sample them improves; greater sampling density increases the odds that a parcel of interest will be measured.

Compared to the cloud-limited observations in the MIPAS data, the randomly sampled data all show improvement, even with fewer total samples (Figure 4-3). The A-15 scenario, which contains roughly one-third as many observations as MIPAS yields errors 45% (unweighted) to 48% (weighted) smaller than the MIPAS sampling scheme at 250 hPa. Such improvements, however, are not inexhaustible: while the error continues to decrease as the number of observations doubles between scenario A-15 and A-30, the improvement from scenario A-15 to A-30 is negligible.

Although the randomly sampled data yield significant improvements over the actual satellite observation locations, such sampling belies current limitations due to cloud contamination. With the addition of only a few more samples within the Atlantic outflow box (Figure 4-3, Panel B) or the tropical band (Figure 4-3, Panel C), however, similar improvements in the overall retrieval are possible.

To the extent observations can be increased close to the outflow of OCS-depleted air from the Amazon, improvements are immediately visible. In Figure 4-3, Panel B, scenario C-1 shows a decrease in the error of 35% compared to the MIPAS observations at 250 hPa. C-5 shows continued reduction in error, though at a slower pace for the upper-troposphere.

Improvements that facilitate additional tropical sampling will yield more data across the globe (Figure 4-3, Panel D). Similar to the C-series, then, we find moderate improvement from B to D-1 (26%) and a substantial decrease from D-1 to D-5 (41%).

As before, the rate begins to decrease after a certain threshold; from D-5 to D-10, the error decreases by only 21%.

The calculated error decreases roughly linearly as the applied noise decreases. Decreasing the error by 15 ppt (approximately 25% of the variation in the MIPAS measurements) yields a decrease in the RMSE of 37%. Given the linearity in the retrieval approach, this result is largely expected, but highlights the value in making even slight improvements to future measurement technology.

Aircraft Results

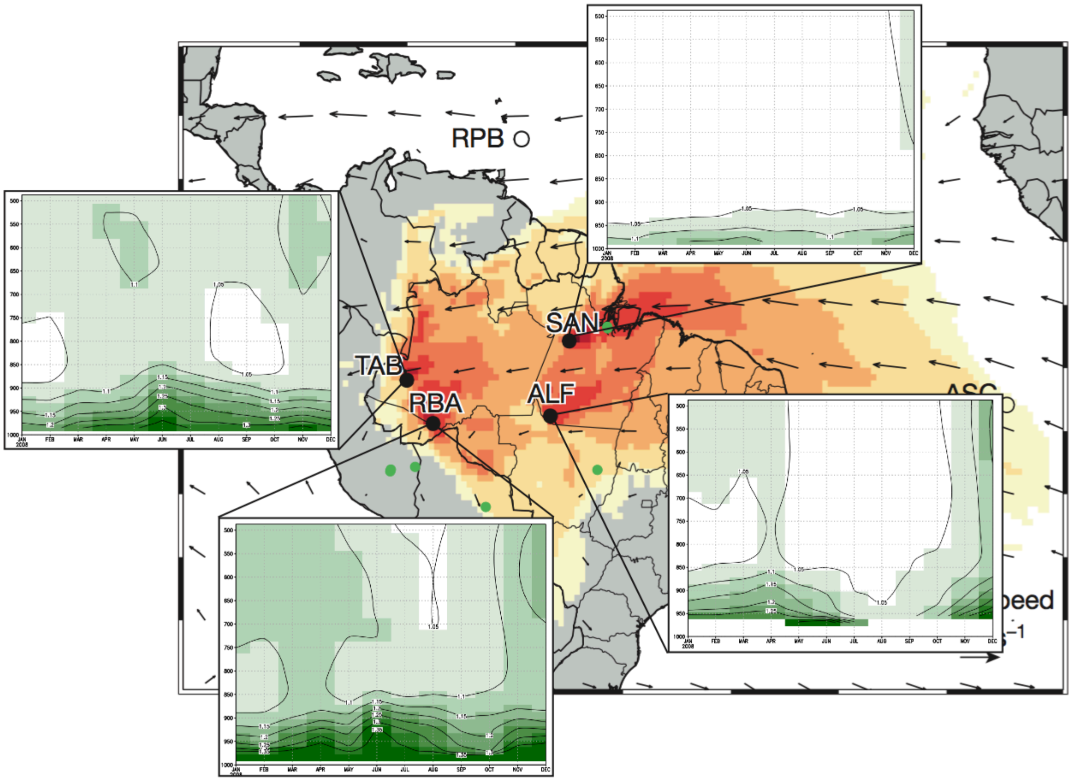

Figure 4-5: Sensitivity ratios for four sites over one year of simulation show differing patterns of surface sensitivity varying by altitude, season and location. Darker colors correspond to larger sensitivity ratios, that is, regions which are strongly influenced to changes in surface fluxes across the Amazon basin. The background map is from Gatti et al. (2014), with colors representing regions of influence computed by Lagrangian modeling of back trajectories.

Future studies relying on aircraft profiles have the potential to yield far more accurate results on a regional scale, though at the cost of a variety of other confounding factors discussed below. Figure 4-5 shows the variation in sensitivity ratios at the sites sampled in Gatti et al. (2014). All four sites within the Amazon show strongest sensitivity in the boundary layer, but mid-tropospheric measurements vary with altitude, season and location. Two western sites, TAB and RBA, show sensitivity to the surface throughout the entire column for nearly all months. In contrast, ALF only shows sensitivity during the wet season, similar to patterns seen in the upper-troposphere satellite data. SAN shows little sensitivity above the boundary layer at any point in the year. These results are consistent with findings by Cassol et al. (2020) that the eastern sites (ALF and SAN) are significantly less sensitive to the interior of the Amazon basin.

Gatti et al. (2014) leverage observations of SF_6 and CO_2 at RPB and ASC to determine the proportion of background CO_2 coming from each of these sites and, by extension, each hemisphere. Although flask samples of OCS and CO_2 are available at a variety of NOAA observation sites, these two specific sites do not currently provide OCS observations. In the absence of this data, two options for future modeling studies exist. Model outputs could average values from both sites to yield an approximate background signal, either weighting sites evenly or with existing SF_6 observations. Alternatively, as these ocean sites are more remote and potentially costly or challenging to sample, the low sensitivity at the coastal Santarém location could also be used for background values.

4.5 Discussion

The above results show that even small improvements in sampling density or instrument noise can yield benefits in the overall retrieval. For comparison, in Chapter 3, the average difference between the high-GPP model and low-GPP model was 25.9 ppt, corresponding to a GPP difference of 18.9 Pg C yr^{-1}. As such, an error reduction of 3.6 ppt (the improvement from reducing the applied instrument noise by 50%) could correspond to a reduction in the flux error by 2.6 Pg C yr^{-1}. Although other sources of error remain, this represents a significant portion of the previous chapter's overall estimate of 8.3 ± 4.6 Pg C yr^{-1}.

The primary issue affecting retrievals in the tropics is cloud contamination and finding ways to diagnose cloudiness and better quantify cloud contamination in the satellite retrieval algorithm remains critical. In the absence of these broader improvements, one approach could be to decrease the observation footprint. The large footprint of limb-sounding instruments in general strongly increases the likelihood that samples will contain clouds. Conversely, smaller footprints increase the odds that a given observation will be cloud-free.

Additional development of nadir-sounding OCS instruments could yield reduced measurement footprints while potentially providing greater sampling density in the tropics. TES has been shown by Kuai et al. (2015) to provide benefits in constraining OCS ocean fluxes. That instrument, however, is unable to measure over land, due to challenges in the retrieval algorithm from reflectance. In general, nadir-sounding instruments would further reduce the lateral sample footprint, but at the expense of vertical resolution. TES, for example, resolves 15 vertical levels, whereas MIPAS resolves 60.

Representation error is a major challenge inherent in the aircraft sampling (Hodyss & Nichols, 2015; Janjić et al., 2018). While the satellite observations represent an aggregate, integrative signal for the Amazon basin, samples close to the surface have a smaller footprint. As such, while measurements at a given site may be generally sensitive to changes in surface fluxes, there is insufficient evidence to show that they are sensitive to changes across the basin. To test this, future modeling studies could perturb smaller regions of the overall Amazon basin and determine regions of influence for given air profiles throughout the year. Lagrangian models like STILT and HYSPLIT have also been employed for this purpose.

While the scope of this study was constrained to changes in the observation system, a more formal inversion approach coupled with more observations in the region of interest could also improve estimates. Recent work by Ma et al. (2020) combines flask, airborne, and satellite data in a global 4-dimensional variational inverse model in order to determine the spatial distribution of the missing flux necessary to close the OCS budget. Given sufficient data in the Amazon, this approach could be applied on a regional basis to address both the overall magnitude of basin productivity as well as spatial and seasonal nuances which are less readily apparent in the integrative satellite measurements.

4.6 Conclusion

The approach shown in the previous chapter is sufficient to yield broad results on a climatological time scale, however a variety of improvements could increase the feasibility of applying this method to questions at finer spatial and temporal scales. Because sampling density, particularly in the often-cloudy tropics, remains a large source of uncertainty, reductions in instrument noise and sampling height also show beneficial reductions in the overall retrieval error.

While satellite observations of OCS provide significant value in constraining GPP over aggregated regions, finer-scale measurements by aircraft can better capture the nuances in surface fluxes. However, just as satellite measurements in the upper troposphere show relatively low sensitivity during the dry season, aircraft measurements must be selected in a way that maximizes the information content in the samples. Convection varies widely between sites, and, as such, additional care must be taken to determine the origin of sampled column parcels.

Along with changes to the inversion approach itself, these improvements to the observing system have the potential to yield better estimates of atmospheric carbonyl sulfide. As these estimates improve, so too will vital constraints on GPP, carbon-climate feedbacks, and the predictive capability of climate models at large.

Chapter 5: Conclusions and Future Work

The value of this work is twofold. On one level, this research further addresses the as-yet unresolved questions about the unbalanced carbonyl sulfide budget. On another level, these improvements are critical for using OCS as a tracer in answering wider questions about the carbon cycle.

Chapter 2 yielded updated global estimates of open biomass burning, constrained by long-term atmospheric records from surface sites. While the present results use GFED as a burned matter database, applying this work to future fire databases could yield suitable flux maps at higher spatial and temporal resolution. Further, by coupling these results to ecosystem models, future studies could investigate the impact of changing land use, fire regimes, and fuel availability on OCS emissions.

Chapter 3 demonstrated that, not only do upper-troposphere measurements of atmospheric carbonyl sulfide yield informative regional constraints, these constraints suggest an overestimation of the plant uptake sink in the Amazon. We note that this overestimation, coupled with increased anthropogenic emissions in Asia, moves the overall OCS budget towards closure. Additionally, these changes further reduce the need for a large missing ocean source, consistent with Lennartz et al. (2017).

Chapter 4 presented a variety of ways to maximize the information content in such satellite observations. The OSSE study presented considered the impacts of sampling height, sampling density and instrument noise as applied to satellite observations. Although the work seeks to mimic samples from the MIPAS instrument, a similar approach could be applied to other, more recent satellite instruments. Further investigations into optimizing samples from aircraft are certainly warranted. These samples could provide high quality, localized data; however, questions about representation error and the origins of sampled parcels remain critically important.

Ongoing work in the carbonyl sulfide community takes many forms. Improved estimates of ocean fluxes have leveraged data from both ship-borne (Lennartz et al., 2017) and satellite (Kuai et al., 2015; Ma et al., 2020) campaigns to constrain both the magnitude and distribution of fluxes. Bottom-up estimates of anthropogenic emissions have shown changes in spatial distribution that must be accounted for in future studies, particularly in Asia (Zumkehr et al., 2018). Recent studies using stable sulfur isotopes have sought to further constrain the role of different fluxes in balancing the global OCS budget (Angert et al., 2019; Hattori et al., 2020).

On a broader level, one of the primary goals in better constraining the sources and sinks of carbonyl sulfide is its use as a tracer or proxy for photosynthesis; better estimates of each of the various OCS budget components ultimately provide better constraints on GPP. Since parameterizations of carbon-climate feedbacks remain a large source of uncertainty across models, such constraints are vital for improving model estimates and, ultimately, our understanding of the linkages between photosynthesis and climate change.

References

Aghedo, A. M., Bowman, K. W., Shindell, D. T., & Faluvegi, G. (2011). The impact of orbital sampling, monthly averaging and vertical resolution on climate chemistry model evaluation with satellite observations. *Atmospheric Chemistry and Physics*, *11*(13), 6493–6514. https://doi.org/10.5194/acp-11-6493-2011

Akagi, S. K., Yokelson, R. J., Wiedinmyer, C., Alvarado, M. J., Reid, J. S., Karl, T., et al. (2011). Emission factors for open and domestic biomass burning for use in atmospheric models. *Atmos. Chem. Phys.*, *11*(9), 4039–4072. https://doi.org/10.5194/acp-11-4039-2011

Akagi, S. K., Yokelson, R. J., Burling, I. R., Meinardi, S., Simpson, I., Blake, D. R., et al. (2013). Measurements of reactive trace gases and variable O3 formation rates in some South Carolina biomass burning plumes. *Atmospheric Chemistry and Physics*, *13*(3), 1141–1165. https://doi.org/10.5194/acp-13-1141-2013

Andreae, M. O. (2019). Emission of trace gases and aerosols from biomass burning – an updated assessment. *Atmospheric Chemistry and Physics*, *19*(13), 8523–8546. https://doi.org/10.5194/acp-19-8523-2019

Andreae, M. O., & Merlet, P. (2001). Emission of trace gases and aerosols from biomass burning. *Global Biogeochemical Cycles*, *15*(4), 955–966. https://doi.org/10.1029/2000GB001382

Angert, A., Said-Ahmad, W., Davidson, C., & Amrani, A. (2019). Sulfur isotopes ratio of atmospheric carbonyl sulfide constrains its sources. *Scientific Reports*, *9*(1), 741. https://doi.org/10.1038/s41598-018-37131-3

Arneth, A., Harrison, S. P., Zaehle, S., Tsigaridis, K., Menon, S., Bartlein, P. J., et al. (2010). Terrestrial biogeochemical feedbacks in the climate system. *Nature Geoscience*, *3*(8), 525–532. https://doi.org/10.1038/ngeo905

Asaf, D., Rotenberg, E., Tatarinov, F., Dicken, U., Montzka, S. A., & Yakir, D. (2013). Ecosystem photosynthesis inferred from measurements of carbonyl sulphide flux. *Nature Geoscience*, *6*(3), 186–190. https://doi.org/10.1038/ngeo1730

Baker, I. T., Prihodko, L., Denning, A. S., Goulden, M., Miller, S., & da Rocha, H. R. (2008). Seasonal drought stress in the Amazon: Reconciling models and observations. *Journal of Geophysical Research: Biogeosciences*, *113*(G1), n/a-n/a. https://doi.org/10.1029/2007JG000644

Balachandran, S., Pachon, J. E., Lee, S., Oakes, M. M., Rastogi, N., Shi, W., et al. (2013). Particulate and gas sampling of prescribed fires in South Georgia, USA. *Atmospheric Environment*, *81*, 125–135. https://doi.org/10.1016/j.atmosenv.2013.08.014

Baldocchi, D. D. (2003). Assessing the eddy covariance technique for evaluating carbon dioxide exchange rates of ecosystems: past, present and future. *Global Change Biology*, *9*(4), 479–492. https://doi.org/10.1046/j.1365-2486.2003.00629.x

Baldocchi, D. D., & Harley, P. C. (1995). Scaling carbon dioxide and water vapour exchange from leaf to canopy in a deciduous forest. II. Model testing and application. *Plant, Cell and Environment*, *18*(10), 1157–1173. https://doi.org/10.1111/j.1365-3040.1995.tb00626.x

Beer, C., Reichstein, M., Tomelleri, E., Ciais, P., Jung, M., Carvalhais, N., et al. (2010). Terrestrial Gross Carbon Dioxide Uptake: Global Distribution and Covariation with Climate. *Science*, *329*(5993), 834–838. https://doi.org/10.1126/science.1184984

Berry, J., Wolf, A., Campbell, J. E., Baker, I., Blake, N., Blake, D., et al. (2013). A coupled model of the global cycles of carbonyl sulfide and CO2: A possible new window on the carbon cycle. *Journal of Geophysical Research: Biogeosciences*, *118*(2), 842–852. https://doi.org/10.1002/jgrg.20068

Billesbach, D. P., Berry, J. A., Seibt, U., Maseyk, K., Torn, M. S., Fischer, M. L., et al. (2014). Growing season eddy covariance measurements of carbonyl sulfide and CO2 fluxes: COS and CO2 relationships in Southern Great Plains winter wheat. *Agricultural and Forest Meteorology*, *184*, 48–55. https://doi.org/10.1016/j.agrformet.2013.06.007

Bingemer, H. G., Andreae, M. O., Andreae, T. W., Artaxo, P., Helas, G., Jacob, D. J., et al. (1992). Sulfur gases and aerosols in and above the equatorial African rain forest. *Journal of Geophysical Research*, *97*(D6), 6207. https://doi.org/10.1029/91JD01112

Blake, N. J., Streets, D. G., Woo, J.-H., Simpson, I. J., Green, J., Meinardi, S., et al. (2004). Carbonyl sulfide and carbon disulfide: Large-scale distributions over the western Pacific and emissions from Asia during TRACE-P. *Journal of Geophysical Research: Atmospheres*, *109*(D15). https://doi.org/10.1029/2003JD004259

Blake, N. J., Campbell, J. E., Vay, S. A., Fuelberg, H. E., Huey, L. G., Sachse, G., et al. (2008). Carbonyl sulfide (OCS): Large-scale distributions over North America during INTEX-NA and relationship to CO2. *Journal of Geophysical Research*, *113*(D9). https://doi.org/10.1029/2007JD009163

Bowman, K. W., Liu, J., Bloom, A. A., Parazoo, N. C., Lee, M., Jiang, Z., et al. (2017). Global and Brazilian Carbon Response to El Niño Modoki 2011-2010.

Earth and Space Science, *4*(10), 637–660. https://doi.org/10.1002/2016EA000204

Campbell, J. E., Carmichael, G. R., Chai, T., Mena-Carrasco, M., Tang, Y., Blake, D. R., et al. (2008). Photosynthetic Control of Atmospheric Carbonyl Sulfide During the Growing Season. *Science*, *322*(5904), 1085–1088. https://doi.org/10.1126/science.1164015

Campbell, J. E., Whelan, M. E., Seibt, U., Smith, S. J., Berry, J. A., & Hilton, T. W. (2015). Atmospheric carbonyl sulfide sources from anthropogenic activity: Implications for carbon cycle constraints. *Geophysical Research Letters*, *42*(8), 3004–3010. https://doi.org/10.1002/2015GL063445

Campbell, J. E., Berry, J. A., Seibt, U., Smith, S. J., Montzka, S. A., Launois, T., et al. (2017). Large historical growth in global terrestrial gross primary production. *Nature*, *544*(7648), 84–87. https://doi.org/10.1038/nature22030

Cassol, H. L. G., Domingues, L. G., Sanchez, A. H., Basso, L. S., Marani, L., Tejada, G., et al. (2020). Determination of Region of Influence Obtained by Aircraft Vertical Profiles Using the Density of Trajectories from the HYSPLIT Model. *Atmosphere*, *11*(10), 1073. https://doi.org/10.3390/atmos11101073

Chen, S.-H., Chen, J.-Y., Chang, W.-Y., Lin, P.-L., Lin, P.-H., & Sun, W.-Y. (2011). Observing System Simulation Experiment: Development of the system and preliminary results. *Journal of Geophysical Research*, *116*(D13). https://doi.org/10.1029/2010JD015103

Chin, M., & Davis, D. D. (1993). Global sources and sinks of OCS and CS2 and their distributions. *Global Biogeochemical Cycles*, *7*(2), 321–337. https://doi.org/10.1029/93GB00568

Conrad, R. (1994). Compensation concentration as critical variable for regulating the flux of trace gases between soil and atmosphere. *Biogeochemistry*, *27*(3). https://doi.org/10.1007/BF00000582

Crutzen, P. J., & Andreae, M. O. (1990). Biomass Burning in the Tropics: Impact on Atmospheric Chemistry and Biogeochemical Cycles. *Science*, *250*(4988), 1669. https://doi.org/10.1126/science.250.4988.1669

Crutzen, P. J., Heidt, L. E., Krasnec, J. P., Pollock, W. H., & Seiler, W. (1979). Biomass burning as a source of atmospheric gases CO, H2, N2O, NO, CH3Cl and COS. *Nature*, *282*(5736), 253–256. https://doi.org/10.1038/282253a0

Crutzen, P. J., Delany, A. C., Greenberg, J., Haagenson, P., Heidt, L., Lueb, R., et al. (1985). Tropospheric chemical composition measurements in Brazil during the dry season. *Journal of Atmospheric Chemistry*, *2*(3), 233–256. https://doi.org/10.1007/BF00051075

Dean, R. B., & Dixon, W. J. (1951). Simplified Statistics for Small Numbers of Observations. *Analytical Chemistry*, *23*(4), 636–638. https://doi.org/10.1021/ac60052a025

Du, Q., Zhang, C., Mu, Y., Cheng, Y., Zhang, Y., Liu, C., et al. (2016). An important missing source of atmospheric carbonyl sulfide: Domestic coal combustion. *Geophysical Research Letters*, *43*(16), 8720–8727. https://doi.org/10.1002/2016GL070075

Duncan, B. N. (2003). Interannual and seasonal variability of biomass burning emissions constrained by satellite observations. *Journal of Geophysical Research*, *108*(D2). https://doi.org/10.1029/2002JD002378

Errico, R. M., Yang, R., Privé, N. C., Tai, K.-S., Todling, R., Sienkiewicz, M. E., & Guo, J. (2013). Development and validation of observing-system simulation experiments at NASA's Global Modeling and Assimilation Office. *Quarterly Journal of the Royal Meteorological Society*, *139*(674), 1162–1178. https://doi.org/10.1002/qj.2027

Frankenberg, C., Fisher, J. B., Worden, J., Badgley, G., Saatchi, S. S., Lee, J.-E., et al. (2011). New global observations of the terrestrial carbon cycle from GOSAT: Patterns of plant fluorescence with gross primary productivity. *Geophysical Research Letters*, *38*(17), n/a-n/a. https://doi.org/10.1029/2011GL048738

Frankenberg, C., O'Dell, C., Guanter, L., & McDuffie, J. (2012). Remote sensing of near-infrared chlorophyll fluorescence from space in scattering atmospheres: implications for its retrieval and interferences with atmospheric CO2 retrievals. *Atmospheric Measurement Techniques*, *5*(8), 2081–2094. https://doi.org/10.5194/amt-5-2081-2012

Friedli, H. R., Atlas, E., Stroud, V. R., Giovanni, L., Campos, T., & Radke, L. F. (2001). Volatile organic trace gases emitted from North American wildfires. *Global Biogeochemical Cycles*, *15*(2), 435–452. https://doi.org/10.1029/2000GB001328

Gara, T. W., Skidmore, A. K., Darvishzadeh, R., & Wang, T. (2019). Leaf to canopy upscaling approach affects the estimation of canopy traits. *GIScience & Remote Sensing*, *56*(4), 554–575. https://doi.org/10.1080/15481603.2018.1540170

Gatti, L. V., Gloor, M., Miller, J. B., Doughty, C. E., Malhi, Y., Domingues, L. G., et al. (2014). Drought sensitivity of Amazonian carbon balance revealed by atmospheric measurements. *Nature*, *506*(7486), 76–80. https://doi.org/10.1038/nature12957

Giglio, L., Randerson, J. T., & van der Werf, G. R. (2013). Analysis of daily, monthly, and annual burned area using the fourth-generation global fire emissions database (GFED4). *Journal of Geophysical Research: Biogeosciences*, *118*(1), 317–328. https://doi.org/10.1002/jgrg.20042

Glatthor, N., Höpfner, M., Baker, I. T., Berry, J., Campbell, J. E., Kawa, S. R., et al. (2015). Tropical sources and sinks of carbonyl sulfide observed from space. *Geophysical Research Letters*, *42*(22), 10,082-10,090. https://doi.org/10.1002/2015GL066293

Glatthor, N., Höpfner, M., Leyser, A., Stiller, G. P., von Clarmann, T., Grabowski, U., et al. (2017). Global carbonyl sulfide (OCS) measured by MIPAS/Envisat during 2002–2012. *Atmospheric Chemistry and Physics*, *17*(4), 2631–2652. https://doi.org/10.5194/acp-17-2631-2017

Goode, J. G., Yokelson, R. J., Ward, D. E., Susott, R. A., Babbitt, R. E., Davies, M. A., & Hao, W. M. (2000). Measurements of excess O_3, CO_2, CO, CH_4, C_2H_4, C_2H_2, HCN, NO, NH_3, HCOOH, CH_3COOH, HCHO, and CH_3OH in 1997 Alaskan biomass burning plumes by airborne Fourier transform infrared spectroscopy (AFTIR). *Journal of Geophysical Research: Atmospheres*, *105*(D17), 22147–22166. https://doi.org/10.1029/2000JD900287

Greenberg, J. P., Zimmerman, P. R., Heidt, L., & Pollock, W. (1984). Hydrocarbon and carbon monoxide emissions from biomass burning in Brazil. *Journal of Geophysical Research*, *89*(D1), 1350. https://doi.org/10.1029/JD089iD01p01350

Guanter, L., Zhang, Y., Jung, M., Joiner, J., Voigt, M., Berry, J. A., et al. (2014). Global and time-resolved monitoring of crop photosynthesis with chlorophyll fluorescence. *Proceedings of the National Academy of Sciences*, *111*(14), E1327–E1333. https://doi.org/10.1073/pnas.1320008111

Harley, P. C., & Baldocchi, D. D. (1995). Scaling carbon dioxide and water vapour exchange from leaf to canopy in a deciduous forest. I. Leaf model parametrization. *Plant, Cell and Environment*, *18*(10), 1146–1156. https://doi.org/10.1111/j.1365-3040.1995.tb00625.x

Hattori, S., Kamezaki, K., & Yoshida, N. (2020). Constraining the atmospheric OCS budget from sulfur isotopes. *Proceedings of the National Academy of Sciences*, *117*(34), 20447–20452. https://doi.org/10.1073/pnas.2007260117

Henze, D. K., Hakami, A., & Seinfeld, J. H. (2007). Development of the adjoint of GEOS-Chem. *Atmospheric Chemistry and Physics*, *7*(9), 2413–2433. https://doi.org/10.5194/acp-7-2413-2007

Hilton, T. W., Whelan, M. E., Zumkehr, A., Kulkarni, S., Berry, J. A., Baker, I. T., et al. (2017). Peak growing season gross uptake of carbon in North America is largest in the Midwest USA. *Nature Climate Change*, *7*(6), 450–454. https://doi.org/10.1038/nclimate3272

Hodyss, D., & Nichols, N. (2015). The error of representation: basic understanding. *Tellus A: Dynamic Meteorology and Oceanography*, *67*(1), 24822. https://doi.org/10.3402/tellusa.v67.24822

Janjić, T., Bormann, N., Bocquet, M., Carton, J. A., Cohn, S. E., Dance, S. L., et al. (2018). On the representation error in data assimilation. *Quarterly Journal of the Royal Meteorological Society*, *144*(713), 1257–1278. https://doi.org/10.1002/qj.3130

Joiner, J., Yoshida, Y., Vasilkov, A. P., Yoshida, Y., Corp, L. A., & Middleton, E. M. (2011). First observations of global and seasonal terrestrial chlorophyll fluorescence from space. *Biogeosciences*, *8*(3), 637–651. https://doi.org/10.5194/bg-8-637-2011

Jung, M., Reichstein, M., Margolis, H. A., Cescatti, A., Richardson, A. D., Arain, M. A., et al. (2011). Global patterns of land-atmosphere fluxes of carbon dioxide, latent heat, and sensible heat derived from eddy covariance, satellite, and meteorological observations. *Journal of Geophysical Research*, *116*. https://doi.org/10.1029/2010JG001566

Kawa, S. R. (2004). Global CO2 transport simulations using meteorological data from the NASA data assimilation system. *Journal of Geophysical Research*, *109*(D18). https://doi.org/10.1029/2004JD004554

Kettle, A. J., Kuhn, U., von Hobe, M., Kesselmeier, J., & Andreae, M. O. (2002). Global budget of atmospheric carbonyl sulfide: Temporal and spatial variations of the dominant sources and sinks. *Journal of Geophysical Research: Atmospheres*, *107*(D22), ACH 25-1. https://doi.org/10.1029/2002JD002187

Khalil, M. A. K., & Rasmussen, R. A. (1984). Global sources, lifetimes and mass balances of carbonyl sulfide (OCS) and carbon disulfide (CS2) in the earth’s atmosphere. *Atmospheric Environment*, *18*(9), 1805–1813. https://doi.org/10.1016/0004-6981(84)90356-1

Kuai, L., Worden, J., Kulawik, S. S., Montzka, S. A., & Liu, J. (2014). Characterization of Aura TES carbonyl sulfide retrievals over ocean. *Atmospheric Measurement Techniques*, *7*(1), 163–172. https://doi.org/10.5194/amt-7-163-2014

Kuai, L., Worden, J. R., Campbell, J. E., Kulawik, S. S., Li, K.-F., Lee, M., et al. (2015). Estimate of carbonyl sulfide tropical oceanic surface fluxes using Aura Tropospheric Emission Spectrometer observations. *Journal of Geophysical Research: Atmospheres*, *120*(20), 11,012-11,023. https://doi.org/10.1002/2015JD023493

Launois, T., Belviso, S., Bopp, L., Fichot, C. G., & Peylin, P. (2015). A new model for the global biogeochemical cycle of carbonyl sulfide - Part 1: Assessment of direct marine emissions with an oceanic general circulation and biogeochemistry model. *Atmospheric Chemistry and Physics*, *15*(5), 2295–2312. https://doi.org/10.5194/acp-15-2295-2015

Launois, T., Peylin, P., Belviso, S., & Poulter, B. (2015). A new model of the global biogeochemical cycle of carbonyl sulfide – Part 2: Use of carbonyl sulfide to constrain gross primary productivity in current vegetation models. *Atmospheric Chemistry and Physics*, *15*(16), 9285–9312. https://doi.org/10.5194/acp-15-9285-2015

Lejeune, B., Mahieu, E., Vollmer, M. K., Reimann, S., Bernath, P. F., Boone, C. D., et al. (2017). Optimized approach to retrieve information on atmospheric carbonyl sulfide (OCS) above the Jungfraujoch station and change in its abundance since 1995. *Journal of Quantitative Spectroscopy and Radiative Transfer*, *186*, 81–95. https://doi.org/10.1016/j.jqsrt.2016.06.001

Lennartz, S. T., Marandino, C. A., von Hobe, M., Cortes, P., Quack, B., Simo, R., et al. (2017). Direct oceanic emissions unlikely to account for the missing source of atmospheric carbonyl sulfide. *Atmospheric Chemistry and Physics*, *17*(1), 385–402. https://doi.org/10.5194/acp-17-385-2017

Lennartz, S. T., von Hobe, M., Booge, D., Bittig, H. C., Fischer, T., Gonçalves-Araujo, R., et al. (2019). The influence of dissolved organic matter on the marine production of carbonyl sulfide (OCS) and carbon disulfide (CS2) in the Peruvian upwelling. *Ocean Science*, *15*(4), 1071–1090. https://doi.org/10.5194/os-15-1071-2019

Liu, J., Bowman, K. W., Schimel, D. S., Parazoo, N. C., Jiang, Z., Lee, M., et al. (2017). Contrasting carbon cycle responses of the tropical continents to the 2015–2016 El Niño. *Science*, *358*(6360), eaam5690. https://doi.org/10.1126/science.aam5690

Liu, X., Huey, L. G., Yokelson, R. J., Selimovic, V., Simpson, I. J., Müller, M., et al. (2017). Airborne measurements of western U.S. wildfire emissions: Comparison with prescribed burning and air quality implications: Western U.S. Wildfire Emissions. *Journal of Geophysical Research: Atmospheres*, *122*(11), 6108–6129. https://doi.org/10.1002/2016JD026315

Ma, J., Kooijmans, L. M. J., Cho, A., Montzka, S. A., Glatthor, N., Worden, J. R., et al. (2020). Inverse modelling of carbonyl sulfide: implementation, evaluation and implications for the global budget. *Atmos. Chem. Phys. Discuss.*, *2020*, 1–39. https://doi.org/10.5194/acp-2020-603

Malhi, Y. (2012). The productivity, metabolism and carbon cycle of tropical forest vegetation: Carbon cycle of tropical forests. *Journal of Ecology*, *100*(1), 65–75. https://doi.org/10.1111/j.1365-2745.2011.01916.x

Masutani, M., Woollen, J. S., Lord, S. J., Emmitt, G. D., Kleespies, T. J., Wood, S. A., et al. (2010). Observing system simulation experiments at the National Centers for Environmental Prediction. *Journal of Geophysical Research*, *115*(D7). https://doi.org/10.1029/2009JD012528

Meinardi, S., Simpson, I. J., Blake, N. J., Blake, D. R., & Rowland, F. S. (2003). Dimethyl disulfide (DMDS) and dimethyl sulfide (DMS) emissions from biomass burning in Australia. *Geophysical Research Letters*, *30*(9). https://doi.org/10.1029/2003GL016967

Montzka, S. A., Calvert, P., Hall, B. D., Elkins, J. W., Conway, T. J., Tans, P. P., & Sweeney, C. (2007). On the global distribution, seasonality, and budget of atmospheric carbonyl sulfide (COS) and some similarities to CO2. *Journal of Geophysical Research: Atmospheres*, *112*(D9). https://doi.org/10.1029/2006JD007665

Nguyen, B. C., Putaud, J. P., Mihalopoulos, N., Bonsang, B., & Doan, C. (1994). CH4 and CO emissions from rice straw burning in South East Asia. *Environmental Monitoring and Assessment*, *31–31*(1–2), 131–137. https://doi.org/10.1007/BF00547188

Nguyen, B. C., Mihalopoulos, N., Putaud, J. P., & Bonsang, B. (1995). Carbonyl sulfide emissions from biomass burning in the tropics. *Journal of Atmospheric Chemistry*, *22*(1), 55–65. https://doi.org/10.1007/BF00708181

Page, S. E., Siegert, F., Rieley, J. O., Boehm, H.-D. V., Jaya, A., & Limin, S. (2002). The amount of carbon released from peat and forest fires in Indonesia during 1997. *Nature*, *420*(6911), 61–65. https://doi.org/10.1038/nature01131

Parazoo, N. C., Bowman, K., Fisher, J. B., Frankenberg, C., Jones, D. B. A., Cescatti, A., et al. (2014). Terrestrial gross primary production inferred from satellite fluorescence and vegetation models. *Global Change Biology*, *20*(10), 3103–3121. https://doi.org/10.1111/gcb.12652

Privé, N. C., Errico, R. M., & Tai, K.-S. (2013). The influence of observation errors on analysis error and forecast skill investigated with an observing system simulation experiment. *Journal of Geophysical Research: Atmospheres*, *118*(11), 5332–5346. https://doi.org/10.1002/jgrd.50452

Protoschill-Krebs, G., Wilhelm, C., & Kesselmeier, J. (1996). Consumption of carbonyl sulphide (COS) by higher plant carbonic anhydrase (CA). *Atmospheric Environment*, *30*(18), 3151–3156. https://doi.org/10.1016/1352-2310(96)00026-X

Randerson, J. T., Chen, Y., van der Werf, G. R., Rogers, B. M., & Morton, D. C. (2012). Global burned area and biomass burning emissions from small fires. *Journal of Geophysical Research: Biogeosciences*, *117*(G4), n/a-n/a. https://doi.org/10.1029/2012JG002128

Reynolds, S. D., Roth, P. M., & Seinfeld, J. H. (1973). Mathematical modeling of photochemical air pollution—I. *Atmospheric Environment (1967)*, *7*(11), 1033–1061. https://doi.org/10.1016/0004-6981(73)90214-X

Rigby, M., Manning, A. J., & Prinn, R. G. (2011). Inversion of long-lived trace gas emissions using combined Eulerian and Lagrangian chemical transport models. *Atmospheric Chemistry and Physics*, *11*(18), 9887–9898. https://doi.org/10.5194/acp-11-9887-2011

Rinsland, C. P., Dufour, G., Boone, C. D., Bernath, P. F., Chiou, L., Coheur, P.-F., et al. (2007). Satellite boreal measurements over Alaska and Canada during June-July 2004: Simultaneous measurements of upper tropospheric CO, C2H6, HCN, CH3Cl, CH4, C2H2, CH3OH, HCOOH, OCS, and SF6 mixing ratios. *Global Biogeochemical Cycles*, *21*(3), n/a-n/a. https://doi.org/10.1029/2006GB002795

Sandoval-Soto, L., Stanimirov, M., von Hobe, M., Schmitt, V., Valdes, J., Wild, A., & Kesselmeier, J. (2005). Global uptake of carbonyl sulfide (COS) by terrestrial vegetation: Estimates corrected by deposition velocities normalized to the uptake of carbon dioxide (CO2). *Biogeosciences*, *2*(2), 125–132. https://doi.org/10.5194/bg-2-125-2005

Seibt, U., Kesselmeier, J., Sandoval-Soto, L., Kuhn, U., & Berry, J. A. (2010). A kinetic analysis of leaf uptake of COS and its relation to transpiration, photosynthesis and carbon isotope fractionation. *Biogeosciences*, *7*(1), 333–341. https://doi.org/10.5194/bg-7-333-2010

Simpson, I. J., Akagi, S. K., Barletta, B., Blake, N. J., Choi, Y., Diskin, G. S., et al. (2011). Boreal forest fire emissions in fresh Canadian smoke plumes: C1-C10 volatile organic compounds (VOCs), CO2, CO, NO2, NO, HCN and CH3CN. *Atmospheric Chemistry and Physics*, *11*(13), 6445–6463. https://doi.org/10.5194/acp-11-6445-2011

Sitch, S., Friedlingstein, P., Gruber, N., Jones, S. D., Murray-Tortarolo, G., Ahlström, A., et al. (2015). Recent trends and drivers of regional sources and sinks of carbon dioxide. *Biogeosciences*, *12*(3), 653–679. https://doi.org/10.5194/bg-12-653-2015

Sprintsin, M., Chen, J. M., Desai, A., & Gough, C. M. (2012). Evaluation of leaf-to-canopy upscaling methodologies against carbon flux data in North America. *Journal of Geophysical Research: Biogeosciences*, *117*(G1). https://doi.org/10.1029/2010JG001407

Steffen, W., Noble, I., Canadell, J., Apps, M., Schulze, E.-D., Jarvis, P., et al. (1998). The Terrestrial Carbon Cycle: Implications for the Kyoto Protocol. *Science.*, *280*, 1393–1394.

Stimler, K., Montzka, S. A., Berry, J. A., Rudich, Y., & Yakir, D. (2010). Relationships between carbonyl sulfide (COS) and CO2 during leaf gas exchange. *New Phytologist*, *186*(4), 869–878. https://doi.org/10.1111/j.1469-8137.2010.03218.x

Stinecipher, J. R., Cameron-Smith, P. J., Blake, N. J., Kuai, L., Lejeune, B., Mahieu, E., et al. (2019). Biomass Burning Unlikely to Account for Missing Source of Carbonyl Sulfide. *Geophysical Research Letters*, *46*(24), 14912–14920. https://doi.org/10.1029/2019GL085567

Stockwell, C. E., Jayarathne, T., Cochrane, M. A., Ryan, K. C., Putra, E. I., Saharjo, B. H., et al. (2016). Field measurements of trace gases and aerosols emitted by peat fires in Central Kalimantan, Indonesia, during the 2015 El Niño. *Atmospheric Chemistry and Physics*, *16*(18), 11711–11732. https://doi.org/10.5194/acp-16-11711-2016

Stockwell, C. E., Christian, T. J., Goetz, J. D., Jayarathne, T., Bhave, P. V., Praveen, P. S., et al. (2016). Nepal Ambient Monitoring and Source Testing Experiment (NAMaSTE): emissions of trace gases and light-absorbing carbon from wood and dung cooking fires, garbage and crop residue burning, brick kilns, and other sources. *Atmospheric Chemistry and Physics*, *16*(17), 11043–11081. https://doi.org/10.5194/acp-16-11043-2016

Suntharalingam, P., Kettle, A. J., Montzka, S. M., & Jacob, D. J. (2008). Global 3-D model analysis of the seasonal cycle of atmospheric carbonyl sulfide: Implications for terrestrial vegetation uptake. *Geophysical Research Letters*, *35*(19). https://doi.org/10.1029/2008GL034332

Tereszchuk, K. A., González Abad, G., Clerbaux, C., Hurtmans, D., Coheur, P.-F., & Bernath, P. F. (2011). ACE-FTS measurements of trace species in the characterization of biomass burning plumes. *Atmospheric Chemistry and Physics*, *11*(23), 12169–12179. https://doi.org/10.5194/acp-11-12169-2011

Thornton, D. C., Bandy, A. R., Blomquist, B. W., & Anderson, B. E. (1996). Impact of anthropogenic and biogenic sources and sinks on carbonyl sulfide in the North Pacific troposphere. *Journal of Geophysical Research: Atmospheres*, *101*(D1), 1873–1881. https://doi.org/10.1029/95JD00617

Timmermans, R. M. A., Lahoz, W. A., Attié, J.-L., Peuch, V.-H., Curier, R. L., Edwards, D. P., et al. (2015). Observing System Simulation Experiments for air quality. *Atmospheric Environment*, *115*, 199–213. https://doi.org/10.1016/j.atmosenv.2015.05.032

van der Tol, C., Verhoef, W., Timmermans, J., Verhoef, A., & Su, Z. (2009). An integrated model of soil-canopy spectral radiances, photosynthesis, fluorescence, temperature and energy balance. *Biogeosciences*, *6*(12), 3109–3129. https://doi.org/10.5194/bg-6-3109-2009

Vincent, R. A., & Dudhia, A. (2017). Fast retrievals of tropospheric carbonyl sulfide with IASI. *Atmospheric Chemistry and Physics*, *17*(4), 2981–3000. https://doi.org/10.5194/acp-17-2981-2017

Wang, Y., Deutscher, N. M., Palm, M., Warneke, T., Notholt, J., Baker, I., et al. (2016). Towards understanding the variability in biospheric CO2 fluxes: using FTIR spectrometry and a chemical transport model to investigate the sources and sinks of carbonyl sulfide and its link to CO2. *Atmospheric Chemistry and Physics*, *16*(4), 2123–2138. https://doi.org/10.5194/acp-16-2123-2016

Watts, S. F. (2000). The mass budgets of carbonyl sulfide, dimethyl sulfide, carbon disulfide and hydrogen sulfide. *Atmospheric Environment*, *34*(5), 761–779. https://doi.org/10.1016/S1352-2310(99)00342-8

Wenzel, S., Cox, P. M., Eyring, V., & Friedlingstein, P. (2016). Projected land photosynthesis constrained by changes in the seasonal cycle of atmospheric CO2. *Nature*, *538*(7626), 499–501. https://doi.org/10.1038/nature19772

van der Werf, G. R., Randerson, J. T., Giglio, L., van Leeuwen, T. T., Chen, Y., Rogers, B. M., et al. (2017). Global fire emissions estimates during 1997–2016. *Earth Syst. Sci. Data*, *9*(2), 697–720. https://doi.org/10.5194/essd-9-697-2017

Whelan, M. E., Hilton, T. W., Berry, J. A., Berkelhammer, M., Desai, A. R., & Campbell, J. E. (2016). Carbonyl sulfide exchange in soils for better estimates of ecosystem carbon uptake. *Atmospheric Chemistry and Physics*, *16*(6), 3711–3726. https://doi.org/10.5194/acp-16-3711-2016

Whelan, M. E., Lennartz, S. T., Gimeno, T. E., Wehr, R., Wohlfahrt, G., Wang, Y., et al. (2018). Reviews and syntheses: Carbonyl sulfide as a multi-scale tracer for carbon and water cycles. *Biogeosciences*, *15*(12), 3625–3657. https://doi.org/10.5194/bg-15-3625-2018

Wiedinmyer, C., Akagi, S. K., Yokelson, R. J., Emmons, L. K., Al-Saadi, J. A., Orlando, J. J., & Soja, A. J. (2011). The Fire INventory from NCAR (FINN): a high resolution global model to estimate the emissions from open burning. *Geoscientific Model Development*, *4*(3), 625–641. https://doi.org/10.5194/gmd-4-625-2011

Yokelson, R. J., Goode, J. G., Ward, D. E., Susott, R. A., Babbitt, R. E., Wade, D. D., et al. (1999). Emissions of formaldehyde, acetic acid, methanol, and other trace gases from biomass fires in North Carolina measured by airborne Fourier transform infrared spectroscopy. *Journal of Geophysical Research: Atmospheres*, *104*(D23), 30109–30125. https://doi.org/10.1029/1999JD900817

Yokelson, R. J., Karl, T., Artaxo, P., Blake, D. R., Christian, T. J., Griffith, D. W. T., et al. (2007). The Tropical Forest and Fire Emissions Experiment: overview and airborne fire emission factor measurements. *Atmospheric Chemistry and Physics*, *7*(19), 5175–5196. https://doi.org/10.5194/acp-7-5175-2007

Yokelson, R. J., Christian, T. J., Karl, T. G., & Guenther, A. (2008). The tropical forest and fire emissions experiment: laboratory fire measurements and synthesis of campaign data. *Atmospheric Chemistry and Physics*, *8*(13), 3509–3527. https://doi.org/10.5194/acp-8-3509-2008

Yokelson, Robert J., Susott, R., Ward, D. E., Reardon, J., & Griffith, D. W. T. (1997). Emissions from smoldering combustion of biomass measured by open-path Fourier transform infrared spectroscopy. *Journal of Geophysical Research: Atmospheres*, *102*(D15), 18865–18877. https://doi.org/10.1029/97JD00852

Zumkehr, A., Hilton, T. W., Whelan, M., Smith, S., & Campbell, J. E. (2017). Gridded anthropogenic emissions inventory and atmospheric transport of carbonyl sulfide in the U.S. *Journal of Geophysical Research: Atmospheres*, *122*(4), 2169–2178. https://doi.org/10.1002/2016JD025550

Zumkehr, A., Hilton, T. W., Whelan, M., Smith, S., Kuai, L., Worden, J., & Campbell, J. E. (2018). Global gridded anthropogenic emissions inventory of carbonyl sulfide. *Atmospheric Environment*, *183*, 11–19. https://doi.org/10.1016/j.atmosenv.2018.03.063